

Jordan Journal of Mechanical and Industrial Engineering (JJMIE)

JJMIE is a high-quality scientific journal devoted to fields of Mechanical and Industrial Engineering. It is published by Hashemite University in cooperation with the Jordanian Scientific Research and Innovation Support Fund, Ministry of Higher Education and Scientific Research.

EDITORIAL BOARD

Editor-in-Chief

Prof. Moh'd Sami Ashhab

Assistant Editors

Dr. Ahmad AlMigdady

Dr. Mohammad Jreissat

Editorial Board

Prof. Tariq A. ALAzab

Al Balqa Applied University

Prof. Jamal Jaber

Al- Balqa Applied University

Prof. Mohamad Al-Widyan

Jordan University of Science and Technology

Prof. Mohammed Taiseer Hayajneh

Jordan University of Science and Technology

Prof. Mohammad Al-Tahat

The University of Jordan

Prof. Ali M. Jawarneh

The Hashemite University

THE INTERNATIONAL ADVISORY BOARD

Abu-Qudais, Mohammad

Jordan University of Science & Technology, Jordan

Tzou, Gow-Yi

Yung-Ta Institute of Technology and Commerce, Taiwan

Abu-Mulaweh, Hosni

Purdue University at Fort Wayne, USA

Jubran, Bassam

Ryerson University, Canada

Afaneh Abdul-Hafiz

Robert Bosch Corporation, USA

Kakac, Sadik

University of Miami, USA

Afonso, Maria Dina

Institute Superior Tecnico, Portugal

Khalil, Essam-Eddin

Cairo University, Egypt

Badiru, Adedji B.

The University of Tennessee, USA

Mutoh, Yoshiharu

Nagaoka University of Technology, Japan

Bejan, Adrian

Duke University, USA

Pant, Durbin

Iowa State University, USA

Chalhoub, Nabil G.

Wayne State University, USA

Riffat, Saffa

The University of Nottingham, U. K

Cho, Kyu-Kab

Pusan National University, South Korea

Saghir, Ziad

Ryerson University, Canada

Dincer, Ibrahim

University of Ontario Institute of Technology,
Canada

Sarkar, MD. Abdur Rashid

Bangladesh University of Engineering &
Technology, Bangladesh

Douglas, Roy

Queen's University, U. K

Siginer, Dennis

Wichita State University, USA

El Bassam, Nasir

International Research Center for Renewable
Energy, Germany

Sopian, Kamaruzzaman

University Kebangsaan Malaysia, Malaysia

Haik, Yousef

United Arab Emirates University, UAE

EDITORIAL BOARD SUPPORT TEAM

Language Editor

Dr. Baker M. Bani-khair

Publishing Layout

Eng. Ali Abu Salimeh

SUBMISSION ADDRESS:

Prof. Moh'd Sami Ashhab, Editor-in-Chief
Jordan Journal of Mechanical & Industrial Engineering,
Hashemite University,
PO Box 330127, Zarqa, 13133, Jordan
E-mail: jjmie@hu.edu.jo



Hashemite Kingdom of Jordan



Hashemite University

Jordan Journal of
Mechanical and Industrial Engineering

JJMIE

An International Peer-Reviewed Scientific Journal

Financed by Scientific Research Support Fund

Volume 15, Number 3, August 2021

<http://jjmie.hu.edu.jo/>

ISSN 1995-6665

Jordan Journal of Mechanical and Industrial Engineering (JJMIE)

JJMIE is a high-quality scientific journal devoted to fields of Mechanical and Industrial Engineering. It is published by Hashemite University in cooperation with the Jordanian Scientific Research and Innovation Support Fund, Ministry of Higher Education and Scientific Research.

Introduction: The Editorial Board is very committed to build the Journal as one of the leading international journals in mechanical and industrial engineering sciences in the next few years. With the support of the Ministry of Higher Education and Scientific Research and Jordanian Universities, it is expected that a heavy resource to be channeled into the Journal to establish its international reputation. The Journal's reputation will be enhanced from arrangements with several organizers of international conferences in publishing selected best papers of the conference proceedings.

Aims and Scope: *Jordan Journal of Mechanical and Industrial Engineering* (JJMIE) is a refereed international journal to be of interest and use to all those concerned with research in various fields of, or closely related to, mechanical and industrial engineering disciplines. *Jordan Journal of Mechanical and Industrial Engineering* aims to provide a highly readable and valuable addition to the literature which will serve as an indispensable reference tool for years to come. The coverage of the journal includes all new theoretical and experimental findings in the fields of mechanical and industrial engineering or any closely related fields (Materials, Manufacturing, Management, Design, Thermal, Fluid, Energy, Control, Mechatronics, and Biomedical). The journal also encourages the submission of critical review articles covering advances in recent research of such fields as well as technical notes.

Guide for Authors

Manuscript Submission:

High-quality submissions to this new journal are welcome now and manuscripts may be either submitted online or email.

Online: For online and email submission upload one copy of the full paper including graphics and all figures at the online, submission site, accessed via <http://jjmie.hu.edu.jo>. The manuscript must be written in MS Word Format. All correspondence including notification of the Editor's decision and requests for revision, takes place by e-mail and via the Author's homepage, removing the need for a hard-copy paper trail

Submission address and contact :

Prof. Moh'd Sami Ashhab

Editor-in-Chief

Jordan Journal of Mechanical & Industrial

Engineering, Hashemite University

PO Box 330127, Zarqa, 13115, Jordan

E-mail: jjmie@hu.edu.jo

Types of contributions: Original research papers and Technical reports

Corresponding author: Clearly indicate who is responsible for correspondence at all stages of refereeing and publication, including post-publication. Ensure that telephone and fax numbers (with country and area code) are provided in addition to the e-mail address and the complete postal address. Full postal addresses must be given for all co-authors.

Original material: Submission of an article implies that the work described has not been published previously (except in the form of itstan abstract or as part of a published lecture or academic thesis), that it is not under consideration for publication elsewhere, the publication is approved by all authors and that, if accepted, it will not be published elsewhere in the same form, in English or in any other language, without the written consent of the Publisher. Authors found to be deliberately contravening the submission guidelines on originality and exclusivity shall not be considered for future publication in this journal.

Withdrawing: If the author chooses to withdraw his article after it has been assessed, he shall reimburse JJMIE with the cost of reviewing the paper.

Manuscript Preparation:

General: Editors reserve the right to adjust style to certain standards of uniformity. Original manuscripts are discarded after publication unless the Publisher is asked to return original material after use. Please use MS Word for the text of your manuscript

Structure: Follow this order when typing manuscripts: Title, Authors, Authors title, Affiliations, Abstract, Keywords, Introduction, Main text, Conclusions, Acknowledgements, Appendix, References, Figure Captions, Figures and then Tables. Please supply figures imported into the text AND also separately as original graphics files. Collate acknowledgements in a separate section at the end of the article and do not include them on the title page, as a footnote to the title or otherwise.

Text Layout: Use 1.5 line spacing and wide (3 cm) margins. Ensure that each new paragraph is clearly indicated. Present tables and figure legends on separate pages at the end of the manuscript. If possible, consult a recent issue of the journal to become familiar with layout and conventions. All footnotes (except for table and corresponding author footnotes) should be identified with superscript Arabic numbers. To conserve space, authors are requested to mark the less important parts of the paper (such as records of experimental results) for printing in smaller type. For long papers (more than 4000 words) sections which could be deleted without destroying either the sense or the continuity of the paper should be indicated as a guide for the editor. Nomenclature should conform to that most frequently used in the scientific field concerned. Number all pages consecutively; use 12 or 10 pt font size and standard fonts.

Corresponding author: Clearly indicate who is responsible for correspondence at all stages of refereeing and publication, including post-publication. The corresponding author should be identified with an asterisk and footnote. Ensure that telephone and fax numbers (with country and area code) are provided in addition to the e-mail address and the complete postal address. Full postal addresses must be given for all co-authors. Please consult a recent journal paper for style if possible.

Abstract: A self-contained abstract outlining in a single paragraph the aims, scope and conclusions of the paper must be supplied.

Keywords: Immediately after the abstract, provide a maximum of six keywords (avoid, for example, 'and', 'of'). Be sparing with abbreviations: only abbreviations firmly established in the field may be eligible.

Symbols: All Greek letters and unusual symbols should be identified by name in the margin, the first time they are used.

Units: Follow internationally accepted rules and conventions: use the international system of units (SI). If other quantities are mentioned, give their equivalent quantities in SI

Maths: Number consecutively any equations that have to be displayed separately from the text (if referred to explicitly in the text).

References: All publications cited in the text should be presented in a list of references following the text of the manuscript.

Text: Indicate references by number(s) in square brackets in line with the text. The actual authors can be referred to, but the reference number(s) must always be given.

List: Number the references (numbers in square brackets) in the list in the order in which they appear in the text.

Examples:

Reference to a journal publication:

[1] M.S. Mohsen, B.A. Akash, "Evaluation of domestic solar water heating system in Jordan using analytic hierarchy process". Energy Conversion & Management, Vol. 38 (1997) No. 9, 1815-1822.

Reference to a book:

[2] Strunk Jr W, White EB. The elements of style. 3rd ed. New York: Macmillan; 1979.

Reference to a conference proceeding:

[3] B. Akash, S. Odeh, S. Nijmeh, "Modeling of solar-assisted double-tube evaporator heat pump system under local climate conditions". 5th Jordanian International Mechanical Engineering Conference, Amman, Jordan, 2004.

Reference to a chapter in an edited book:

[4] Mettam GR, Adams LB. How to prepare an electronic version of your article. In: Jones BS, Smith RZ, editors. Introduction to the electronic age, New York: E-Publishing Inc; 1999, p. 281-304

Free Online Color : If, together with your accepted article, you submit usable color and black/white figures then the journal will ensure that these figures will appear in color on the journal website electronic version.

Tables: Tables should be numbered consecutively and given suitable captions and each table should begin on a new page. No vertical rules should be used. Tables should not unnecessarily duplicate results presented elsewhere in the manuscript (for example, in graphs). Footnotes to tables should be typed below the table and should be referred to by superscript lowercase letters.

Notification: Authors will be notified of the acceptance of their paper by the editor. The Publisher will also send a notification of receipt of the paper in production.

Copyright: All authors must sign the Transfer of Copyright agreement before the article can be published. This transfer agreement enables Jordan Journal of Mechanical and Industrial Engineering to protect the copyrighted material for the authors, but does not relinquish the authors' proprietary rights. The copyright transfer covers the exclusive rights to reproduce and distribute the article, including reprints, photographic reproductions, microfilm or any other reproductions of similar nature and translations.

Proof Reading: One set of page proofs in MS Word format will be sent by e-mail to the corresponding author, to be checked for typesetting/editing. The corrections should be returned within 48 hours. No changes in, or additions to, the accepted (and subsequently edited) manuscript will be allowed at this stage. Proofreading is solely the author's responsibility. Any queries should be answered in full. Please correct factual errors only, or errors introduced by typesetting. Please note that once your paper has been proofed we publish the identical paper online as in print.

PAGES	PAPERS
243 - 249	Mathematical Modelling and Correlation Between the Primary Waviness and Roughness Profiles During Hard Turning <i>Mite Tomov, Bojan Prangoski, Pawel Karolczak</i>
251 - 263	Data Envelopment Analysis in the Presence of Correlated Evaluation Variables <i>Mohammad Bastani, Saeedeh Ketabi, Reza Maddahi, Roya M.Ahari</i>
265– 272	Study of the Effect of some Deflector's Geometry Factors on the Reduction of the Aerodynamic Drag of the Car Model <i>Mohamed MAINE, Mohamed EL OUMAMI, Otmame BOUKSOUR, Boujemâa NASSIRI</i>
273– 282	Performance and Emission Characteristics of Waste Frying Oil Biodiesel Stored Under Optimized Condition <i>J. Pavalavana Pandian , M. Pugazhivadivu , B. Prabu, K. Velmurugan, V.S.K. Venkatachalapathy</i>
283– 290	Impact of Carbon Nano Tubes on the Performance and Emissions of a Diesel Engine Fuelled with Pongamia Oil Biodiesel <i>N.Kapilan</i>
291– 300	Effect of Gable Roof Angle on Natural Ventilation for an Isolated Building <i>Lip Kean Moey, Man Fai Kong, Vin Cent Tai, Tze Fong Go, Nor Mariah Adam</i>
301– 308	Dynamic Behavior of Thin Graphite/Epoxy FRP Simply Supported Beam Under Thermal Load Using 3-D Finite Element Modeling <i>Fadi Alfaqs</i>
309– 318	Effect of Alkaline Nitrates and Operating Temperature on the Performance of Dye Sensitized Solar Cells <i>Mohamad I. Al-Widyan, Borhan A. Albiss, Mohammad S. Ali</i>

Mathematical Modelling and Correlation Between the Primary Waviness and Roughness Profiles During Hard Turning

Mite Tomov^{a*}, Bojan Prangoski^a, Pawel Karolczak^b

^aFaculty of Mechanical Engineering-Skopje, Ss Cyril and Methodius University in Skopje, Karpos II, 1000 Skopje, North Macedonia.

^bDepartment of Machine Tools and Mechanical Technologies, Wroclaw University of Science and Technology, 50-370 Wroclaw, Poland

Received April 13 2021

Accepted June 23 2021

Abstract

This paper presents a research primarily aimed at determining the correlations between the primary profile, waviness, and roughness profiles during hard turning, using mathematical modeling of the primary profile (Pa), the roughness profile (Ra) and the waviness profile (Wa). For this purpose, we employed the Design of experiments (DOE) principles expressing the roughness parameters models as a nonlinear function shape of the first order of the input variables: cutting speed (v), feed (f), depth of cut (a_p) and tool nose radius (r_e). The models were done based on empirical data obtained by processing special rings made of steel IEN C55 (AISI 1055) with hardness of 53 ± 1 HRC, using a CNC lathe. The obtained results are presented as mathematical models, but also as 3D diagrams which clearly show the change trends and their mutual relationships for the considered parameters.

© 2021 Jordan Journal of Mechanical and Industrial Engineering. All rights reserved

Keywords: hard turning, surface roughness, primary profile, waviness profile, roughness profiles, mathematical modeling;

1. Introduction

C.L. He and all. in the research presented in [1] provide a detailed overview of the State-of-the-art of the influential factors and the applied methods used in surface roughness modeling in turning, regardless of whether the processed materials have normal or enhanced hardness. It is worth noting that when processing materials with enhanced hardness, i.e., hardness greater than 45 HRC, more and more attempts are made to replace grinding with turning [2-4]. Therefore, there is much research referring to hard turning surface roughness modelling and predicting. Agrawal A. and all., in [5] provide a table overview of the literature review of optimization studies on hard turning. Thus, [5-8] provide results of the impact of cutting parameters (cutting speed, feed and depth of cut) when optimizing and predicting the roughness of the surfaces, using the regression analysis technique, while the research [9-10] also analyze the impact of cutting speed, feed and depth of cut, but using the *Taguchi experimental design*. Research referring to, among other things, how tool geometry impacts the predicting of surface roughness during hard turning can also be found in [11,12]. The influence of the cutting tool materials on the roughness optimization is analyzed in [13-15], while the influence of the workpiece hardness on the roughness profile formation during hard turning is analyzed in [4,16-18]. Information on the impact of different cooling mediums is provided in the research in [19, 20].

A detailed analysis of the aforementioned research suggests that, regardless of the input parameters in the research (cutting parameters, tool geometry, cutting tool materials, workpiece hardness etc.), surface roughness optimization and prediction during hard turning is done for very few parameters, typically the Ra and Rz (Rt) parameters. This trend of replacing the term surface roughness with the Ra parameter continues even today when researching the processing of new materials [21,22] or when controlling complex machine parts [23].

Knowing that the roughness profile derives from the primary profile and total profile by applying appropriate filtering techniques [24], it is worth noting that the research [2-20] lacks information on waviness deviation and form deviation of the pieces, crucial values for the proper functioning of the parts.

This research aims at determining whether any correlation exists between the primary profile (P-profile), the waviness profile (W-profile), and the roughness profile (R-profile) during hard turning. This is very important because the primary profile, the waviness profile, and the roughness profile coexist and together they form the surface profile (the total profile) as a 2D representation of the surface topography. The justification of this research arises also from the fact that, according to DIN 4760, from a structural point of view, we can simultaneously define six types of deviations including waviness (2nd order deviation) and roughness (3rd to 5th order deviation). We will analyze the correlation between the primary profile, the waviness profile, and the roughness profile using mathematical models for modelling the Pa, Wa, and Ra parameters.

* Corresponding author e-mail: mite.tomov@mf.edu.mk.

2. Method of mathematical modeling and correlation

We will analyze the correlation between the primary profile, the waviness profile, and the roughness profile using mathematical models for modelling the Pa, Wa, and Ra parameters. The term “correlation” used in this research should not be understood purely from a mathematical point of view (expressed by the correlation coefficient). We have used this term here to describe the relationship between the trends of the change of the considered parameters obtained from the nonlinear models.

Models for the Pa, Wa and Ra parameters, as a nonlinear function shape, equation (1), using a four-factorial plan experiments of the first order where the independent input variables comprise cutting speed (v), feed (f), tool nose radius (r_c) and depth of cut (a_p), with repetition in the middle point of the investigated hyperspace.

$$Pa, Wa, Ra = Constant \cdot v^a \cdot f^b \cdot a^c \cdot r_c^d \quad (1)$$

The number of experiments is $2^4 = 16$, plus 4 experiments as a repetition in the middle points, total of 20 experiments. A detailed plan of the experiments is presented in Table 2.

In the experiments involving a repetition of the middle point (17-20) we intentionally deviated from the value of tool nose radius (r_c). The calculation suggests that the geometric mean of the radius is approximately 0.7mm, while the research uses the value of 0.8mm. The reason is that there are no inserts with a radius of 0.7mm and the closest standard value available is 0.8mm.

The verification of the adequacy of the obtained mathematical models employs the Fisher test with a significance level of $\alpha = 0.05$. The accuracy of the mathematical models is defined at 95% confidence interval.

This research also includes the SE parameter in order to obtain information about the stability of the turning process. The SE parameter was calculated for the primary profile and modelled using mathematical models, similarly to the other considered parameters.

3. Experimental verification

3.1. Work piece material

This research uses work pieces made of steel EN C55 (AISI 1055). In order to achieve appropriate hardness of 53 ± 1 HRC the work pieces were thermally enhanced. The pieces are made into rings in order to achieve uniform hardness throughout the entire cross-section. The size of the rings is $\phi 100 \times \phi 82 \times 20$ mm and they are clamped on a special device using a flat key, Figure 1.

3.2. Machine and cutting tool

The work rings are processed using CNC lathe, shown on Figure 2, model OKUMA LB 15-II (C-1S) has variable spindle speed from 38 to 3800 rpm, feed rate from 0.001 to 1000 mm/rev and 15 kW spindle drive motor. From one side the work pieces are clamped in the chuck, while, on the other side, they lean on the tailstock, Figure 2. Before processing starts in accordance with the experimental plan, the rings were processed in order to remove the circular run

out from the clamping of the rings. A coolant (17% concentration of cutting oil in water) was applied during the machining of the rings. The pieces were processed using a holder designated ADPNN2525M15-A (Tungaloy), with $\kappa_r = 62.5^\circ$, $\gamma_o = 0^\circ$, $\lambda_s = -10^\circ$ and cutting T-CBN negative inserts designated 2QP-DNGA 150404-BXM20, 2QP-DNGA 150408-BXM20 and 2QP-DNGA 150412-BXM20 from the Tungaloy. Every working rings is processed using a new cutting edge of the insert, in order to eliminate the effect from the wear of the inserts.

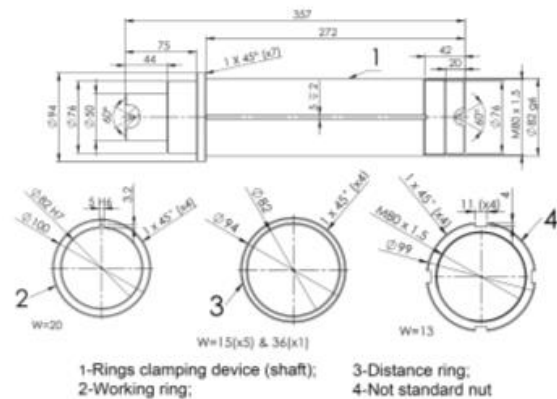


Figure 1. 2D drawing and realistic view of rings clamping device

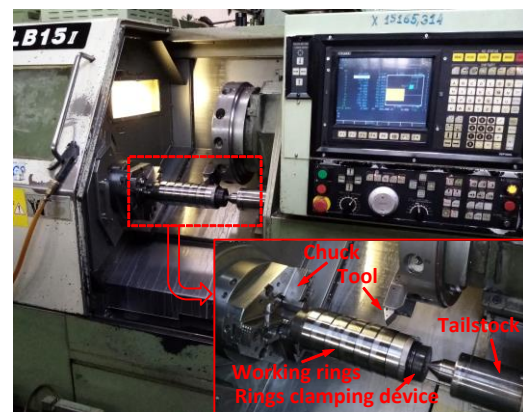


Figure 2. Ring clamping device setting of CNC lathe

3.3. Measurement equipment and conditions

The primary, roughness and waviness profiles of the processed rings were obtained using the procedure presented in Figure 3. The total profile measurements were done using the Surf test model No. SJ-410 (Mitutoyo make), Figure 4, in accordance with the measuring conditions presented in Table 1. The total profiles were measured at five equally spaced locations around the circumference of

the work rings to obtain the statistically significant data for the test. A pick-up stylus used had a top angle of 60° and a top radius of $2 \mu\text{m}$. A skidless pick-up was used. During the measurements, the instrument was mechanically leveled

with respect to the measured surface. The measuring system was calibrated using a type C etalon with $Ra=2.97 \mu\text{m}$, and was verified using a type C etalon with $Ra=6 \mu\text{m}$. The used calibration etalons have a measuring uncertainty of 5%.

Table 1: Measurement conditions of primary, waviness and roughness profiles.

Profile/Parameters	Primary profile / Pa / SE	
Experiment No.	All	
Filter	Gaussian	
$r_{up} (\mu\text{m})$	2	
λ_s profile filter (μm)	2.5	
L evaluation length $L = 1 \times N$ (mm)	8	
Profile/Parameters	Waviness profile / Wa	
Experiment No.	1,2,5,6,9,10,13,14	3,4,7,8,11,12,15,16, 17,18,19,20
Filter	Gaussian	
$r_{up} (\mu\text{m})$	2	
λ_c profile filter (mm)	0.25	0.8
λ_f profile filter (mm)	2.5	
L evaluation length (mm)	$5 \times 2.5 = 12.5$	
Profile/Parameters	Roughness profile / Ra	
Experiment No.	1,2,5,6,9,10,13,14	3,4,7,8,11,12,15,16, 17,18,19,20
Filter	Gaussian	
$r_{up} (\mu\text{m})$	2	
λ_s profile filter (μm)	2.5	
λ_c profile filter (mm)	0.25	0.8
lr sampling length		
ln evaluation length $ln = N \times lr$ (mm)	$5 \times 0.25 = 1.25$	$5 \times 0.8 = 4$

Table 2. Experimental plan and results.

No.	V (m/min)	f (mm/rev)	a_p (mm)	r_e (mm)	Pa (μm)	Wa (μm)	Ra (μm)	SE P -profile
1	100	0.09	0.2	0.4	0.726	0.055	0.695	0.036
2	200	0.09	0.2	0.4	0.772	0.049	0.735	0.047
3	100	0.2	0.2	0.4	3.447	0.078	3.398	0.033
4	200	0.2	0.2	0.4	3.407	0.094	3.362	0.044
5	100	0.09	0.4	0.4	0.749	0.076	0.720	0.033
6	200	0.09	0.4	0.4	0.821	0.055	0.782	0.041
7	100	0.2	0.4	0.4	3.347	0.080	3.309	0.038
8	200	0.2	0.4	0.4	3.501	0.101	3.442	0.051
9	100	0.09	0.2	1.2	0.258	0.045	0.249	0.147
10	200	0.09	0.2	1.2	0.317	0.054	0.287	0.078
11	100	0.2	0.2	1.2	0.944	0.036	0.938	0.047
12	200	0.2	0.2	1.2	0.949	0.040	0.934	0.047
13	100	0.09	0.4	1.2	0.284	0.042	0.254	0.115
14	200	0.09	0.4	1.2	0.236	0.041	0.218	0.141
15	100	0.2	0.4	1.2	0.958	0.035	0.938	0.039
16	200	0.2	0.4	1.2	0.956	0.036	0.940	0.054
17	141.4	0.134	0.283	0.8	0.700	0.026	0.699	0.039
18	141.4	0.134	0.283	0.8	0.732	0.027	0.726	0.043
19	141.4	0.134	0.283	0.8	0.726	0.028	0.713	0.032
20	141.4	0.134	0.283	0.8	0.788	0.036	0.781	0.042

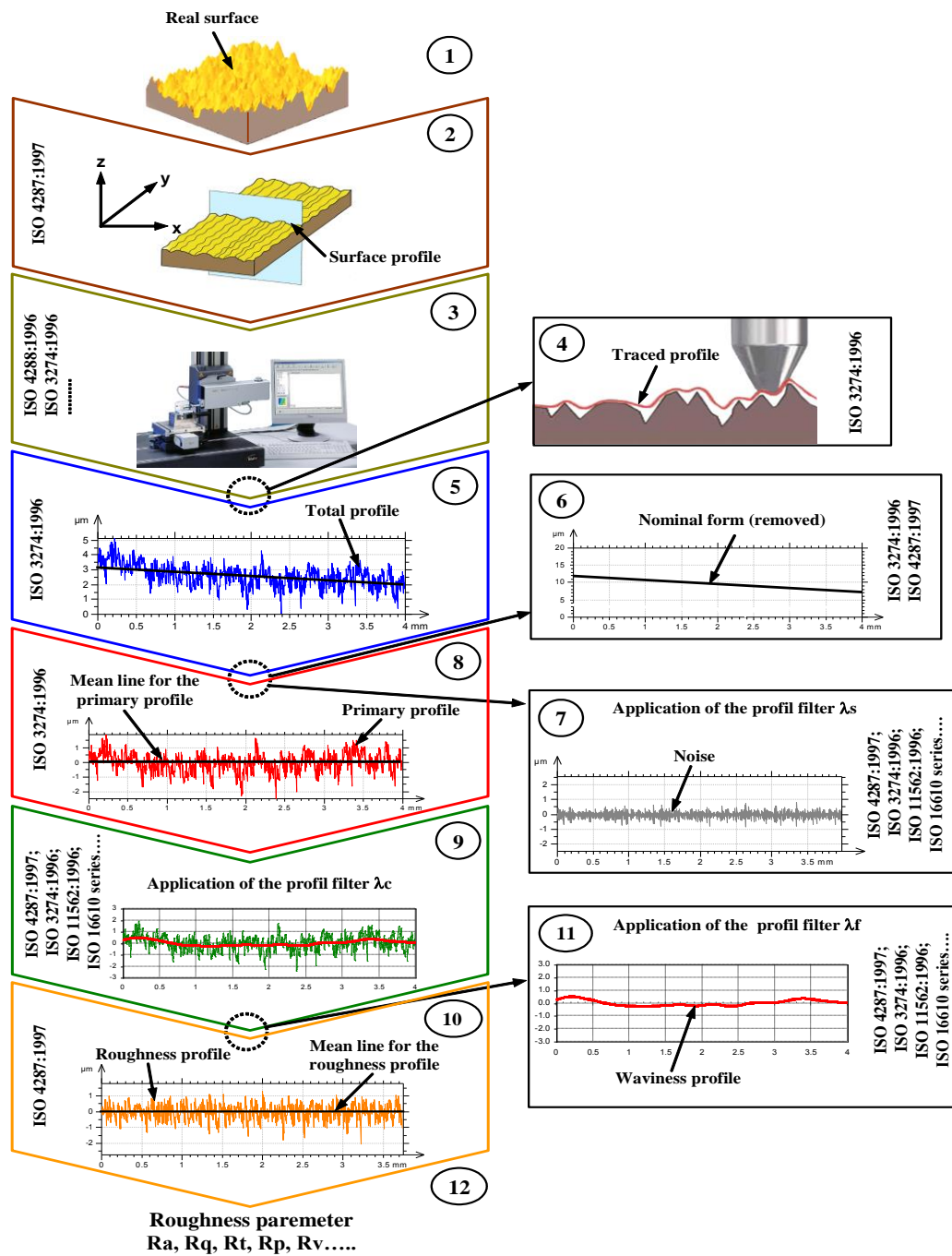


Figure 3. Procedure for obtaining the primary profile, the roughness profile, and the waviness profile [24]

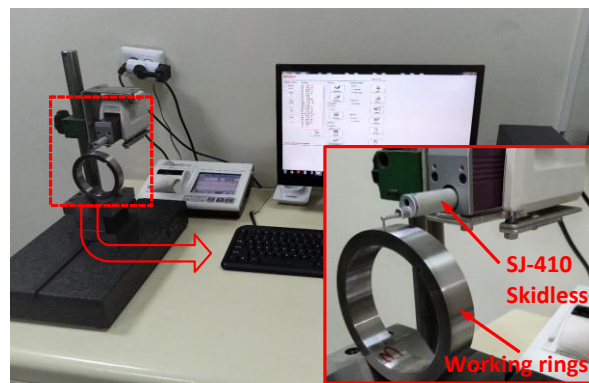


Figure 4. Surf test model No. SJ-410 (Mitutoyo make).

4. Results and discussion

The entire plan for the realization of the experiments, as well as the measured values for the parameters Pa, Wa, Ra and SE is presented in Table 2. The value of all parameters provided in Table 2 are mean values of five measurements.

The following mathematical models for the considered parameters were obtained based on the value from Table 2 and applying the methodology stipulated in point 2:

$$P_a = 15.259 \cdot v^{0.0379652} \cdot f^{1.722} \cdot a^{-0.0155956} \cdot r_\epsilon^{-1.054} \quad (2)$$

$$W_a = 0.0406614 \cdot v^{0.0491459} \cdot f^{0.1290388} \cdot a^{0.0104809} \cdot r_\epsilon^{-0.5093038} \quad (3)$$

$$R_a = 17.175 \cdot v^{0.0278376} \cdot f^{1.783} \cdot a^{-0.0278446} \cdot r_\epsilon^{-1.071} \quad (4)$$

$$SE = 0.0095850 \cdot v^{0.1733292} \cdot f^{-0.5450216} \cdot a^{0.0656300} \cdot r_\epsilon^{0.5575011} \quad (5)$$

The mathematical models expressed by the equations (2-5) represent first order models without mutual interaction

and without factor significance evaluation. Their dispersion analysis together with an adequacy evaluation is provided in Table 3.

For the Wa parameter, the data in Table 3 suggest that the coefficient of determination is 0.64 which justifies its use in the first order model with mutual interaction. We decided to use a model without mutual interaction in order to enable the comparability with the models of the other considered parameters and because of the affirmative assessment of the adequacy.

The minus sign in the exponent in the term of the model indicates an inverse relationship between that term of the model and the modeled parameter.

In order to provide a graphic overview of the obtained mathematical models of the modeled parameters of the investigated hyperspace, the paper presents 3D graphs, Figures 5-8.

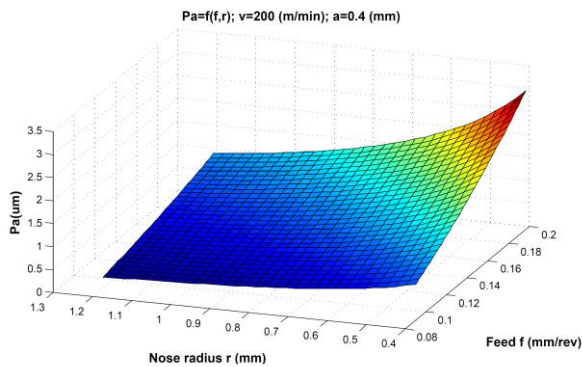


Figure 5. 3D graph for Pa, according to equation (2)

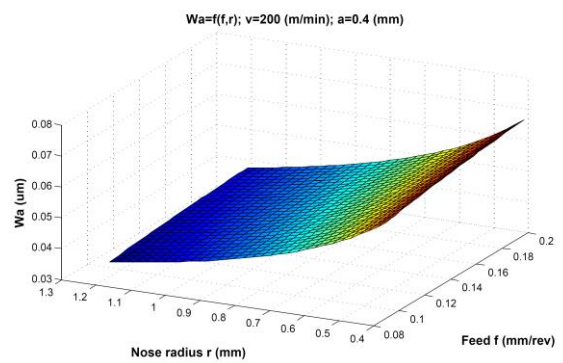


Figure 6. 3D graph for Wa, according to equation (3)

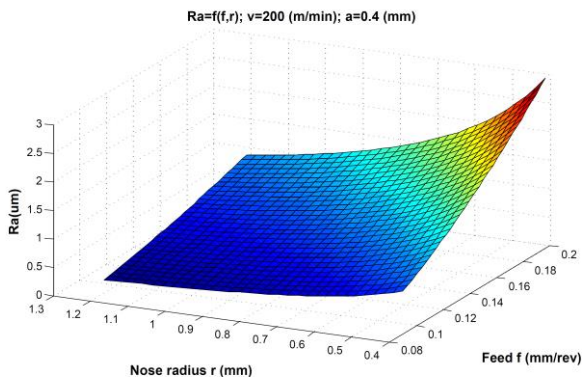


Figure 7. 3D graph for Ra, according to equation (4)

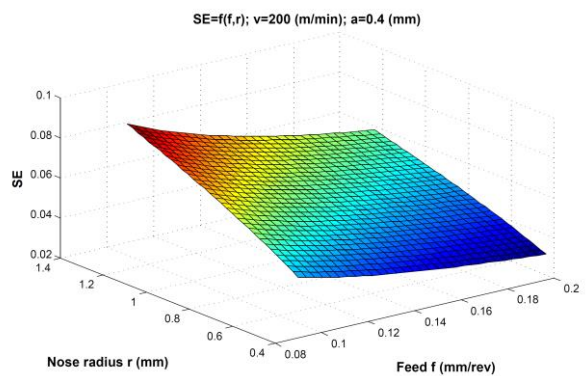


Figure 8. 3D graph for SE, according to equation (5)

If we compare the mathematical models for the Pa and the Ra parameters, equations (2) and (4), we will note a great similarity with respect to the input variables constants and exponents. There the feed (f) and the tool nose radius (r_ϵ) have a dominant influence. The increase of the cutting speed and the reduction of the depth of cut, although not significant, can contribute to the increase of the values of Pa and Ra . Figure 9 presents a 3D diagram showing the modelled surfaces for the Pa and Ra parameters. Figure 9 clearly demonstrates that Pa and Ra behave identically throughout the investigated hyperspace.

If we analyze the mathematical model for the Wa parameter, we will also conclude that the feed (f) and the tool nose radius (r_ϵ) have a dominant influence. However, their influence, especially the influence of f is significantly reduced, as shown by the value of their exponents. The comparison between the Ra mathematical model and the Wa mathematical model shows an increased influence of the cutting speed (v) and a sign change of the exponent for

the depth of cut (a_p). Although, according to DIN 4760, the causes of 2nd order deviations (waviness) do not include the feed (f), the tool nose radius (r_ϵ), the cutting speed (v) and the depth of cut (a_p), when combined they can still cause some tool vibrations or elastic deformations on the work piece, which can directly impact the waviness.

It is interesting to compare the Wa mathematical model and the SE mathematical model, equations (3) and (5), Figure 10. The increase of the value of f can increase the value of Wa and reduce the value of SE , i.e., the increase of the r_ϵ value leads to a reduction of the Wa and an increase of the SE . This suggests that while waviness decreases, the stochastic character of the primary profile and the roughness profile, expressed by the SE parameter, increases. Still, we need to mention that the waviness profile derives from the mean line of the primary profile. The mean line of primary profile is obtained using profile filters. Any “imperfection” in obtaining the mean line does influence the shape of the waviness profile.

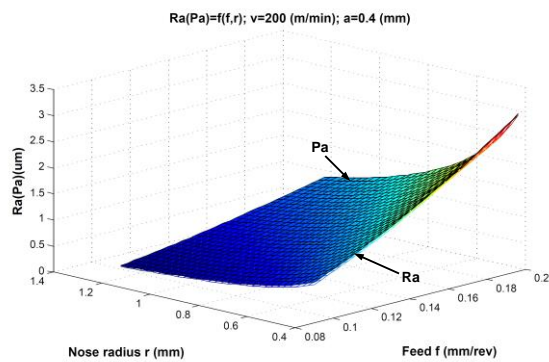


Figure 9. 3D graph for correlation between Pa and Ra

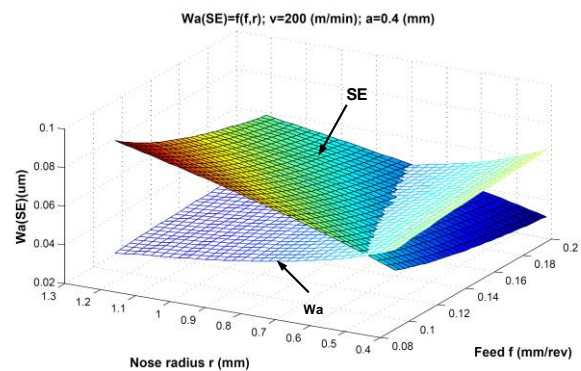


Figure 10. 3D graph for correlation between Wa and SE

Table 3. Dispersion analysis

	Degrees of freedom	Sum of squares	Dispersion s/f	Dispersion ratios	Table value	Model adequacy evaluation	
	f	s		fr	ft		
Pa	Residual sum	15	0.264080	0.017605	8.510	8.740	fr<ft adequate
	Experiment error	3	0.007536	0.002512			
	Model adequacy	12	0.256544	0.021379			
Multiple regression coefficient: R=0.9899							
Ra	Residual sum	15	0.198609	0.013241	6.820	8.740	fr<ft adequate
	Experiment error	3	0.007023	0.002341			
	Model adequacy	12	0.191586	0.015966			
Multiple regression coefficient: R=0.9928							
Wa	Residual sum	15	1.889	0.125933	7.014	8.740	fr<ft adequate
	Experiment error	3	0.065015	0.021672			
	Model adequacy	12	1.824	0.151998			
Multiple regression coefficient: R=0.6384							
SE	Residual sum	15	1.779	0.118613	7.988	8.740	fr<ft adequate
	Experiment error	3	0.053990	0.017997			
	Model adequacy	12	1.725	0.143767			
Multiple regression coefficient: R=0.7526							

5. Conclusion

The research presented in this paper showed that there is a strict correlation between the primary profile (P-profile), the waviness profile (W-profile) and the roughness profile (R-profile) during hard turning. The SE parameter, particularly its small values, shows the stability of the hard turning process employed in this research. The great similarity between the Pa and the Ra parameters, especially the small value for the Wa parameter for all 20 experiments, perhaps provides the justification for emphasizing the roughness profile and the roughness parameters when modeling the geometric structure of the surface.

Acknowledgments

The authors of this paper would like to use this opportunity to express a great deed of gratitude to prof. Mikolaj Kuzinovski Ph.D (in memoriam) for the invaluable contribution to the realization of the research in this study, "ZM RezniAlati DOO -Skopje" (representative in Republic North Macedonia for the Tungaloy Corporation company) for the donated turning tools used in the research, as well as to the company "SVEMEK DOOEL-Skopje" for the technical assistance provided in the processing of the work pieces and measuring the surface roughness.

References

- [1]. C.L. He, W.J. Zong, J.J. Zhang, "Influencing factors and theoretical modeling methods of surface roughness in turning process: State-of-the-art". *International Journal of Machine Tools and Manufacture* 129 (2018) 15–26.
- [2]. Bartaryaa G., Choudhury S.K., "Effect of cutting parameters on cutting force and surface roughness during finish hard turning AISI52100 grade steel". *Procedia CIRP* 1, 2012, 651-656.
- [3]. Mohruni A.S., Yanis M., Edwin K., "Development of surface roughness prediction model for hard turning on AISI D2 steel using cubic boron nitride insert". *JurnalTeknologi (Sciences & Engineering)*, 2018, 80(1), 173–178.
- [4]. Kumar S, Singh D, Kalsi NS., "Surface quality evaluation of AISI 4340 steel having varying hardness during machining with TiN-coated CBN inserts". *Journal of Engineering Tribology* 2016; 231 (7):925-933.
- [5]. Agrawal A, Goel S, Rashid W Bin, Price M. "Prediction of surface roughness during hard turning of AISI 4340 steel (69 HRC)". *Applied Soft Computing Journal* 2015; 30: 279–286.
- [6]. Bartaryaa G., Choudhury S.K., "Effect of cutting parameters on cutting force and surface roughness during finish hard turning AISI52100 grade steel". *Procedia CIRP* 1, 2012, 651-656.
- [7]. Panda, A., Sahoo, A.K., Rout, A.K., "Investigations on surface quality characteristics with multi-response parametric optimization and correlations". *Alexandria Engineering Journal*, 2016, 55, 1625–1633.
- [8]. Xio Z, Lio X, Long Z, Li M., "Effect of cutting parameters on surface roughness using orthogonal array in hard turning of AISI 1045 steel with YT5 tool". *International Journal of Advanced Manufacturing Technology* 2017; 93:273–282.
- [9]. Das SR, Panda A, Dhupal D., "Experimental investigation of surface roughness, flank wear, chip morphology and cost estimation during machining of hardened AISI 4340 steel with coated carbide insert". *Mechanics of Advanced Materials and Modern Processes* 2017; 3:1–14.
- [10] J. Jena, A. Panda, A. K. Behera, P. C. Jena, Sudhansu Ranjan Das, D. Dhupal, "Modeling and Optimization of Surface Roughness in Hard Turning of AISI 4340 Steel with Coated Ceramic Tool". *Innovation in Materials Science and Engineering, Proceedings of ICEMIT 2017*, 2. 151-160.
- [11]. Meddour I, Yallese MA, Khattabi R, Elbah M, Boulanour L., "Investigating and modeling of cutting forces and surface roughness when hard turning of AISI 52100 steel with mixed ceramic tool: cutting conditions optimization". *International Journal of Advanced Manufacturing Technology* 2015;77:1387–1399.
- [12]. Zerti O, Yallese MA, Khattabi R, Chaoui K, Mabrouki T. "Design optimization for minimum technological parameters when dry turning of AISI D3 steel using Taguchi method". *International Journal of Advanced Manufacturing Technology* 2016; 89:1915–1934.
- [13]. Khellaf A, Aouici H, Smaiah S, Boutabba S, Yallese MA, Elbah M., "Comparative assessment of two ceramic cutting tools on surface roughness in hard turning of AISI H11 steel: including 2D and 3D surface topography". *International Journal of Advanced Manufacturing Technology* 2016; 89:333-354.
- [14]. Kacal A, Yildirim F., "Application of grey relational analysis in high-speed machining of hardened AISI D6 steel". *Journal of Mechanical Engineering Science* 2012; 227:1566–1576.
- [15]. Gunay M, Yucel E., "Application of Taguchi method for determining optimum surface roughness in turning of high-alloy white cast iron". *Measurement* 2013; 46:913–919.
- [16]. Tang L, Gao C, Huang J, Shen H, Lin X., "Experimental investigation of surface integrity in finish dry hard turning of hardened tool steel at different hardness levels". *International Journal of Advanced Manufacturing Technology* 2015; 77:1655–1669.
- [17]. Derakhshan E.D., Akbari A.A., "Experimental investigation on the effect of workpiece hardness and cutting speed on surface roughness in hard turning with CBN tools". *Proceedings of the World Congress on Engineering 2009 Vol II WCE 2009, July 1 - 3, 2009, London, U.K.*
- [18]. Mia M, Dhar NR., "Optimization of surface roughness and cutting temperature in high-pressure coolant-assisted hard turning using Taguchi method". *International Journal of Advanced Manufacturing Technology* 2017; 88:739–753.
- [19]. Chinchankar S, Salve AV, Netake P, More A, Kendre S, Kumar R., "Comparative evaluations of surface roughness during hard turning under dry and with water-based and vegetable oil-based cutting fluids". *Procedia Materials Science* 2014; 5:1966–1975.
- [20]. Naigade DM, Patil DK, Sadaiah M., "Some investigations in hard turning of AISI 4340 alloy steel in different cutting environments by CBN insert". *International Journal of Machining and Machinability of Materials* 2013; 14:165–193.
- [21]. Khannaa N., Agrawal C., Dograb M., Pruncuc C.I., "Evaluation of tool wear, energy consumption, and surface roughness during turning of inconel 718 using sustainable machining technique". *Journal of Materials Research and Technology* 2020; 9(3); 5794-5804.
- [22]. Kannan A, Mohan R, Viswanathan R, Sivashankar N. Experimental investigation on surface roughness, tool wear and cutting force in turning of hybrid (Al7075+SiC+Gr) metal matrix composites. *Journal of Materials Research and Technology* 2020; 9(6); 16529-16540.
- [23]. Tian F.C., Jiang H., Chen C., Accurate Modeling and Numerical Control Machining for Spiral Rotor of Double Rotor. *Jordan Journal of Mechanical and Industrial Engineering (JJMIE)* 2021; 15 (1); 15-21.
- [24]. TomovM, KuzinovskiM, CichoszP, "A new parameter of statistic equality of sampling lengths in surface roughness measurement". *StrojnickiVestnik* 2013; 59(5):339-348.

Data Envelopment Analysis in the Presence of Correlated Evaluation Variables

Mohammad Bastani^a, Saeedeh Ketabi^b, Reza Maddahi^{*c}, Roya M. Ahari^a

^aDepartment of Industrial Engineering, Najafabad Branch, Islamic Azad University, Najafabad, Iran.

^bDepartment of Management, University of Isfahan, Isfahan, Iran

^c Department of Mathematics, Najafabad Branch, Islamic Azad University, Najafabad, Iran.

Received March 19 2020

Accepted June 21 2021

Abstract

Data Envelopment Analysis (DEA) is a technique for evaluating homogeneous Decision-Making Units (DMUs) that consume similar inputs to produce similar outputs. An essential principle in this method is to identify inputs and outputs; the identified inputs (outputs) must be independent of each other. However, in the real world, there are situations where there is a correlation between two or more inputs (outputs), and then one of them should be considered in the performance evaluation. This issue can cause problems in practice. The main question, in this case, will be that "Which of these two or more correlated variables should be considered in evaluating DMUs?". In this paper, a method for determining an essential variable using a DEA model is presented. In this way, the basic models of DEA have been integrated with the 0-1 programming to achieve the above objective. The proposed method is then improved by using Centralized Data Envelopment Analysis (CDEA) model, followed by refining the performance evaluation variables. At last, the application of the proposed method has been verified for different examples. Results show that the proposed method selects the appropriate variable from among the correlated variables. Also, improving the method using a centralized approach leads to the selection of a variable that increases the total efficiency. The application and implementation of the proposed method is simple and does not have computational complexity. It also does not need experts' judgment, so it is a cost-effective way.

© 2021 Jordan Journal of Mechanical and Industrial Engineering. All rights reserved

Keywords: Centralized Data Envelopment Analysis, Correlated variables, Performance evaluation, Filtering variables;

1. Introduction

Data Envelopment Analysis (DEA) was first introduced by Charnes et al. [1], which is a method for evaluating the relative performance of a set of Decision Making Units (DMUs) with multiple inputs and outputs. Manufacturing units, firms, hospital wards, bank branches, and individuals can be mentioned as examples of DMUs. So far, this method has been widely used for efficiency analysis in production and services as well as in the public and private sectors. Emrouznejad and Yang [2] describe an extensive list of DEA-related articles includes developing the theory and methodology and actual applications in various scenarios.

Today, Institutions that provide services or produce products are bound to perform effectively because of the intense competitive environment and limited resources. The performance of these institutions is critically linked to the correct selection of input and output variables [3]. Also, the selection of variables is essential because DEA is a nonparametric approach and loses discriminatory power with increasing dimensions of production space. The reason is that when the number of inputs and outputs increases, the observations in the dataset are projected in a large number of orthogonal directions, and the Euclidean distance between observations increases. As a result, many of the observations placing on the frontier; accordingly, DEA loses its discriminatory power [4]. Thus, selecting

appropriate input and output variables is one of the key and significant issues in the DEA.

One of the basic principles of the DEA is that efficiency measurement depends on the interrelationships between inputs and outputs. The nonlinear multiplier formula, efficiency, has calculated the ratio of a weighted sum of outputs to a weighted sum of inputs [5]. Available DEA models assume that the inputs or outputs of DMUs are independent of each other at all times [6]. However, in terms of Pedraja-Chaparro et al. [7], one of the four factors that influence the results of DEA models is the degree of correlation between inputs and outputs. In many practical applications of DEA, there may be a correlation between two or more selected input variables or output variables. In some of the articles relating to the DEA, to reduce computations and increase efficiency discrimination between DMUs, it is described that if the correlation coefficient between each pair of input or output vectors is a strong and positive, one of the input or output vectors could be omitted [8-16].

Dyson et al. [17] stated this issue as one of the pitfalls in DEA and showed that omitting a highly correlated variable can have a significant impact on the efficiency measurement of some DMUs. In general, whether there is a correlation between inputs, between outputs or between inputs and outputs, is ignored when constructing models by analysts or experts [5]. So, the selection of variables between two or more variables cannot be done by the expert and was based on subjective judgment. Therefore, the need to select a

* Corresponding author e-mail: reza.maddahi.esf@gmail.com.

variable is based on a scientific method. Based on the mentioned points, the main question is, "Which of the two or more correlated variables should be considered in evaluating DMUs?"

Researchers have proposed different ways to solve these problems. Farzipoor Sean et al. [9] specify the correlation coefficient threshold beyond which the elimination of one or more input vectors has no statistically significant effect on the efficiency mean. They point out that some DEA articles have stated that if the correlation coefficient between each pair of input (output) vectors is 0.9 and above 0.9, one of the inputs (outputs) vectors can be removed.

Kao et al. [18] presented a two-stage approach combining Independent Component Analysis (ICA) and DEA to improve the discriminatory capability of DEA results. They first used ICA to extract input variables to produce independent components (ICs). Then independent components were selected as independent sources of input variables and inputted into the DEA model.

Some researchers have combined DEA and principal component analysis (PCA) to reduce the number of variables. The idea of combining DEA and PCA methodologies was first introduced by [19] and then was developed by [20] and [21]. The PCA-DEA approach is used to replace the main inputs or outputs with a set of uncorrelated components that each of them is linear combinations of the main variables. The obtained uncorrelated components are called principal components (PC) that are obtained from the eigenvalues of the covariance matrix or correlation matrix of the main variables. However, this approach can avoid inaccurate computation of efficiency for DMUs with correlated inputs and outputs but has high computational complexity. It is also often difficult to correct the interpretation of the PCs that are linear combinations of the main variables.

Dario and Simar [22] to reduce the production possibility space dimensionality, integrate highly correlated inputs and outputs into a single input and a single output by eigenvalues. [4] state that the [22] method is very similar to PCA-DEA. Their final model should have only one input and one output; therefore, it is not as public as other methods and has little practical application.

Pastor et al. [23] presented a methodology for analyzing the relevance of a variable about its contribution to efficiency. Two radial DEA formulas are considered, one with the tested variable (candidate) and the other without it. A binomial statistical test specifies that if this variable affects efficiency measure, the candidate variable is important for the production process.

Banker [24] surveys statistical tests to show the importance of input or output variables in the production process. The null hypothesis is that the tested variable does not affect the production process. Simulation studies have been performed, and the results show that these tests are better than Corrected Ordinary Least Squares (COLS) based tests.

Sirvent et al. [25] using Monte Carlo simulation for compared [23] method with [24] tests regarding various factors such as sample size, model size, the specification of returns to scale, and the type and level of inefficiency. The results show that the [23] method is more robust than the [24] tests in terms of the inefficiency distribution and the assumption of a return to scale type.

Jenkins and Anderson [26] describe a systematic statistical method that eliminates variables containing minimum information using partial correlation as a measure of information content. Information in the input or output

variable is measured as the variance on the set of production units. Zero variations show that all observed production units have the same value for that variable. They indicated that the removal of highly correlated variables could have the main impact on efficiency scores; therefore, multivariate statistical method using partial correlation measures to determine the relevance of a given variable is useful.

Adler and Yazhemsy [27] demonstrated that PCA-DEA accomplishes better than [26] method, especially when analyzing relatively small datasets. They argue that comparing the methodologies shows that PCA-DEA provides a more powerful tool than the [26] method with more accurate results.

Ruggiero [28] proposed a variable selection method in which a main measure of efficiency is acquired from a set of known production variables and developed guidelines for selection. After that, efficiency regressed against a set of candidate variables. If the coefficients in the regression are statistically significant and have an appropriate sign, the variables are related to the production process. This analysis is repeated. The analysis stops when there are no other variables with appropriate and significant signs coefficients.

Fanchon [29] presented a method that specifies the optimal number of variables and the contribution of each variable to the measure of efficiency. A five-step approach defines a set of variables that best describes the output behavior and then uses the DEA repeatedly to analyze the increase in the number of efficient observations. Two regressions were performed to validate the inserted variables, one with only efficient observations and the other with efficient and inefficient observations. A statistical significance of the regression coefficients represents the validity of the variable. An example in the computer industry for separate efficient and inefficient firms is used to explain the proposed method. The method proposed by [29] is similar to the [28] method [4].

Simar and Wilson [30] propose statistical tests for measuring the relevance of inputs and outputs, as well as tests to consider potentially aggregating inputs and outputs. They use bootstrap methods to obtain the appropriate critical values for these tests. Monte Carlo experiments show the true sizes and power of the proposed tests.

Nataraja and Johnson [4] analyzed the four methods of PCA-DEA, [23], [30], [28] by Monte Carlo simulation to determine the advantages and disadvantages of each approach.

Xia and Chen [6] was used Choquet integral to consider the correlation between the input or output variables by the DEA. First, self-efficacy models based on Choquet integral were applied, which could achieve more efficiency values than existing ones. The idea was then extended to the cross-efficiency models, including the game cross-efficiency models. Based on the regret theory, the optimal DEA analysis was also examined. Various models have been developed to estimate the ranking distances of DMUs. They argue that models of interaction between inputs and outputs can achieve wider ranking intervals.

Ji et al. [31] have developed a new fuzzy DEA model using fuzzy Choquet integral as a cumulative tool to evaluate DMUs' efficiency. This model can be used to evaluate DMUs efficiency with interactive fuzzy inputs or outputs. Finally, numerical examples are used to show the proposed model performance. They state that their study has prepared a theoretical fuzzy DEA framework, but the proposed model has high computational complexity.

Li et al. [32] presented method for choosing DEA Inputs/outputs based on the Akaike's information criteria

(AIC)approach. Wagner and Shimshak [33]developed stepwise procedure to variable selection. Morita and Avkiran [34]used diagonal layout experiments, which is a statistical approach for selecting inputs and outputs in DEA. Some researchers have also used the mixed integer linear programming Approach to select the variable [35-37].The models that have been proposed for issue of correlated inputs/outputs selection in DEA are presented in Table 1.

Reviewing various studies in the literature, reveals that various studies have been conducted to address the issue of correlated inputs and outputs in DEA. The selection of inputs/outputs is a main step in DEA that is typically performed before DEA models are implemented. This issue affects the discriminatory power of DEA and the efficiency score of DMUs. Therefore, the decision to choose from correlated variables is one of the important issues in the literature. An essential aspect of this issue is the development and improvement of practical models for selecting a variable from several correlated variables. This paper proposes DEA-based models for selecting correlated variables inefficiency evaluation of the DMUs.The proposed models in this study are easy to understand for managers and decision makers compared to previous methods and do not require experts' judgment, extensive calculations and statistical analysis. These models also provide valuable management information to managers and decision makers for decision making, and are a good guide for selecting input (output) variables for them. Variables with a correlation of 0.9 and above 0.9 are considered in this paper.

The structure of this research is as follows; In Section 2, the basic DEA models and centralized data envelopment analysis (CDEA) models used in this research are reviewed. In Sections 3, 4, 5 the proposed method is presented. Then, in Sections 6 and 7, a numerical example and a case study are illustrated to describe the method. Finally, the conclusions and recommendations are discussed in Sections8 and 9.

2. Introducing the basic DEA and CDEA models

In this study, a method for determining an essential variable among the correlated variables for DEA andCDEA models is presented. Then the proposed method is used for refining the performance evaluation variables. Therefore, it is necessary to have a brief Introduction with each of these models. Thus in this section, first the basic DEA models and then CDEA model are introduced.

2.1. BCC input and output-oriented models

DEA is a well-known mathematical approach applied to assess the relative efficiency of a set of similar DMUs. This method measures the relative efficiency of each DMU based on its inputs and outputs[38]. The objective function of the DEA model tries to identify the DMUs that produce the maximum outputs with the minimum input. Although this method has been used as a useful tool in management and economics, however, it has recently found many applications in engineering problems[39-40].DEA models can be divided into two categories: input-oriented and output-oriented. The purpose of input-oriented models is to reducing the number of used resources (inputs) by keeping the output constant and output-oriented models seeking to increase the output values by keeping the number of used resources constant[40].In this subsection, the basic input and output-oriented models are reviewed[41]. These models are known as BCC models using the first names of their providers. The input and output BCC envelopment models for the evaluation are shown below in models (1) and (2), respectively. These models, which are called variable returns to scale models, arise with the basic DEA models that assume constant returns to scale and presented by[1].To solve these models, we used GAMS software.

Table 1. Proposed models correlated inputs/outputs selection in DEA

Year and author	Research method								
	ANOVA	DEA	ICA	PCA	eigenvalues	multivariate statistical	Choquet integral	Fuzzy Choquet integral	0-1 programming
Ueda and Hoshiai (1997)		✓		✓					
Jenkins and Anderson(2003)						✓			
Farzipoor Saen et al. (2005)	✓								
Dario and Simar (2007)					✓				
Kao et al. (2011)		✓	✓						
Xia and Chen (2017)							✓		
Ji et al. (2018)								✓	
This paper		✓							✓

Min θ

$$\begin{aligned}
 s.t \quad & \sum_{j=1}^n \lambda_j x_{ij} \leq \theta x_{ik}, i = 1, 2, \dots, m, \\
 & \sum_{j=1}^n \lambda_j y_{rj} \geq y_{rk}, r = 1, 2, \dots, s, \quad (1) \\
 & \sum_{j=1}^n \lambda_j = 1, \\
 & \lambda_j \geq 0, j = 1, 2, \dots, n.
 \end{aligned}$$

Max φ

$$\begin{aligned}
 s.t \quad & \sum_{j=1}^n \lambda_j x_{ij} \leq x_{ik}, i = 1, 2, \dots, m, \\
 & \sum_{j=1}^n \lambda_j y_{rj} \geq \varphi y_{rk}, r = 1, 2, \dots, s, \quad (2) \\
 & \sum_{j=1}^n \lambda_j = 1, \\
 & \lambda_j \geq 0, j = 1, 2, \dots, n.
 \end{aligned}$$

In the above models it is assumed that there are n DMUs, each DMU used m inputs (x_{ij}) to produce s output (y_{rj}). DMU $_k$ is the DMU to be evaluated. Also, if the objectives function value of the above models in the optimal solution equals one, under evaluation unit is efficient, and otherwise, it is called inefficient.

2.2. Centralized Data Envelopment Analysis (CDEA) Model

Since conventional DEA models set separate goals for each DMU and do not consider total input consumption and total output production, models are presented as the centralized resource allocation in which there is a centralized decision-maker who oversees all the units in operation. The main purpose of this model is to optimize total input consumption and output production.

Lozano and Villa [42] present a model called centralized input-oriented resource allocation, in which the centralized decision-maker optimizes the total input consumption. This model ensures that the total output production is not reduced. In the centralized model analysis, all units are projected on the efficient frontier as is common in conventional DEA models, but the process is done in an integrated way rather than in separate ways. In other words, in the centralized model, only one linear programming model is used to project all units on the efficient frontier, whereas in the conventional DEA models, a separate model is used for each unit, and each unit is projected separately on the efficient frontier. Another significant difference between the centralized input-oriented model is that, instead of reducing the inputs of each unit, the goal is to reduce the total input consumption of all units.

CDEA has a wide variety of applications in various sectors, such as fast-food restaurants [43], schools[44], recycling municipalities [45], and public service organizations[46].

The radial centralized input-oriented model consists of two phases. In the first phase, a proportional reduction is sought for all inputs, and the second phase is followed by a further decrease in each input and an increase in each output non-radially. These models are as follows [42]:

$$\begin{aligned}
 \theta^* = \text{Min } \theta \\
 s.t \quad & \sum_{j=1}^n \sum_{l=1}^n \lambda_{lj} x_{ij} \leq \theta \sum_{j=1}^n x_{ij}, i = 1, 2, \dots, m, \\
 & \sum_{j=1}^n \sum_{l=1}^n \lambda_{lj} y_{rj} \geq \sum_{j=1}^n y_{rj}, r = 1, \dots, s, \quad (3) \\
 & \sum_{l=1}^n \lambda_{lj} = 1, \forall_j \\
 & \lambda_{lj} \geq 0, \theta \text{ free}
 \end{aligned}$$

By solving the first phase of the model, θ^* will be obtained as the optimal value of model number 3. So, the second phase of the radial centralized input-oriented model is as model (4) [42]:

$$\begin{aligned}
 \text{Max } \quad & \sum_{i=1}^m s_i + \sum_{r=1}^s t_r \\
 s.t \quad & \sum_{j=1}^n \sum_{l=1}^n \lambda_{lj} x_{ij} = \theta^* \sum_{j=1}^n x_{ij} - s_i, i = 1, \dots, m \\
 & \sum_{j=1}^n \sum_{l=1}^n \lambda_{lj} y_{rj} = \sum_{r=1}^s y_{rj} + t_r, r = 1, 2, \dots, s, \quad (4) \\
 & \sum_{l=1}^n \lambda_{lj} = 1, \forall_j \\
 & \lambda_{lj}, s_i, t_r \geq 0.
 \end{aligned}$$

In the next section, the proposed method is presented to select an essential variable from the correlated variables.

3. Proposed models in order to select among the correlated variables

In DEA, there are three types of correlation between variables: 1- Correlation between outputs variables on inputs variables. 2- Correlation between outputs variables. 3- Correlation between inputs variable. Correlation between outputs variables on inputs variable is necessary. On the other hand, the inputs (outputs) variables must be independent of each other. In this section, the proposed method is presented in order to select from correlated variables, whether input or output, on several different bases. In the first part, the basic DEA models provide the basis for the first method, and the second part uses the CDEA (second method). The proposed models have been formulated following a few steps. Fig.1 depicts the framework of proposed models.

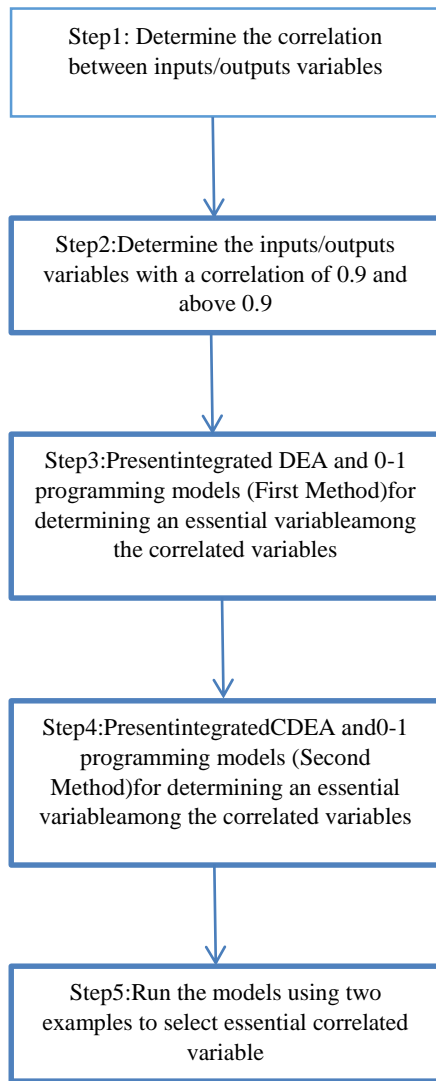


Figure 1. Framework showing the proposed models to select among the correlated variables

3.1. Selection of correlated variables Using Basic DEA Models (First Method)

According to the subjects mentioned in the previous section, there may be two general situations for dealing with correlated variables. First, a situation in which only the correlation between the inputs variables is considered and the select between them is considered. Second, a situation in which only the correlation between the outputs variables is considered and the select between them is considered. In this section, the output-oriented BCC model is used to select from the correlated input variables, and the input-oriented BCC model is used to select from the correlated output variables. The reason for this choice is that in the selection of correlated input variables, the value of the output-oriented efficiency, and in the selection of correlated output variables, the value of the input-oriented efficiency DMUs is desired. This cross selection causes the simultaneous impact of the input correlated variables on the outputs, and the output correlated variables on the inputs are examined in terms of efficiency. To simplify, we first select between two correlated variables in each section, and then this

method is generalized to more correlated variables. The following paragraphs explained the proposed models mathematically.

3.1.1. Select between two correlated input variables using basic DEA Models

In this section for more simplicity and understanding of the proposed method, first, the procedure of choice between two correlated inputs variables and then the choice between two correlated output variables are raised. First, suppose that two input variables are correlated. Without reducing the generality of the proposed method, it is assumed for simplicity that the first two input variables are the correlated variables. The method proposed in this research section consisted of two stages. At first, each DMU is allowed to select one of the two above variables as input, by developing an output oriented envelopment model into a 0-1 programming model. In the second stage, a criterion for selecting that variable as the first input in the evaluation of all units is presented (Method A and Method B). The same process can be used for the case where the two output variables are correlated; the difference is that in this case, the input-oriented envelopment model is used to select the output variable from the two correlated outputs. Consider the following 0-1 programming model:

$$\begin{aligned}
 \varphi_k^* &= \text{Max } \varphi \\
 s.t \quad &\sum_{j=1}^n \lambda_j x_{ij} \leq x_{ik}, \quad i = 2, \dots, m, \\
 &\sum_{j=1}^n \lambda_j x_{1j} \leq x_{1k} + \mu M_1, \\
 &\sum_{j=1}^n \lambda_j x'_{1j} \leq x'_{1k} + (1 - \mu) M_2, \quad (5) \\
 &\sum_{j=1}^n \lambda_j y_{rj} \geq \varphi y_{rk}, \quad r = 1, 2, \dots, s, \\
 &\sum_{j=1}^n \lambda_j = 1, \\
 &\lambda_j \geq 0, \quad \mu \in \{0, 1\}
 \end{aligned}$$

In model (5), M_1 and M_2 considered as two very large positive numbers, so if the μ variable which is 0-1 variable in this model is equal to zero in the optimal solution, the constraint related to the first correlated variable x_{1j} () activate in the model and the constraint related to the second correlated variable (x'_{1j}) was ineffective in the optimal model and solution. Otherwise, if the μ is equal one in the optimal answer, the opposite will happen.

It is imperative to note that Model (5) alone cannot be used to evaluate DMUs because the homogeneity of the DMUs in this model is violated. That is maybe, the first input genus for two different units considered different that this is inconsistent with DEA principles. In different ways, using the optimal solutions of the model (5), can decide about select the first input from two correlated variables (second stages). Two methods are suggested in this section:

Method A: The number of times that x_{1j} and x'_{1j} have been considered as inputs can be considered as a criterion for their selection as the first input of units.

Method B: It can be used to compare the sum of the efficiency of the units that selected the above variable as inputs. That is, compared the sum of φ_k^* that related to two groups to each other. Suppose that the sets D and D' respectively indicate the set of indexes corresponding to the DMUs that have chosen x_{1j} and x'_{1j} as the first input variable, then if $\sum_{k \in D} \varphi_k^* < \sum_{k \in D'} \varphi_k^*$, x_{1j} selected as the first input and otherwise x'_{1j} is selected. In output-oriented model if $\varphi_k^* = 1$, the unit under evaluation is efficient, and if $\varphi_k^* > 1$ the unit is inefficient, thus less $\sum \varphi_k^*$ is the variable selection criterion.

Therefore, the proposed method in this section to select an input variable in the presence of two types of correlated input variables is briefly proposed in the following framework (see Fig. 2):

1. Solve model (5) for all DMUs.
2. Determine the suitable input using the optimum objective function values of the model (5) by Method A or Method B.

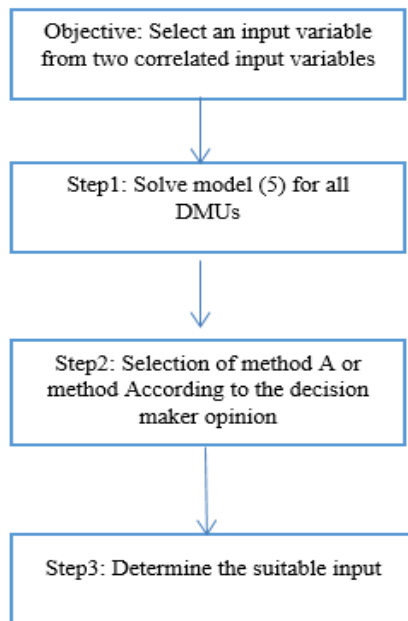


Figure 2. Framework for selecting an input variable from two correlated input variables

3.1.2. Select between two correlated output variables using basic DEA Models

In this section, the proposed model is developed to select from two correlated output variables. If the correlated variables are from the type of outputs, Model (1) can be used as the basis for suitable choosing between two correlated outputs y_{1j} and y'_{1j} . The reason for this choice is that in the selection of correlated output variables, the value of the input-oriented efficiency DMUs is desired. So model (1) changes as follows:

$$\begin{aligned}
 &\theta_k^* = \text{Min } \theta \\
 \text{s.t. } &\sum_{j=1}^n \lambda_j x_{ij} \leq \theta x_{ik}, \quad i = 1, 2, \dots, m, \\
 &\sum_{j=1}^n \lambda_j y_{rj} \geq y_{rk}, \quad r = 2, \dots, s, \\
 &\sum_{j=1}^n \lambda_j y_{1j} \geq y_{1k} + \mu N_1, \quad (6) \\
 &\sum_{j=1}^n \lambda_j y'_{1j} \geq y'_{1k} + (1 - \mu) N_2, \\
 &\sum_{j=1}^n \lambda_j = 1, \\
 &\lambda_j \geq 0, \mu \in \{0, 1\}
 \end{aligned}$$

In model (6), N_1 and N_2 considered as two small negatives numbers that with become zero or one of μ 0-1 variable, make the corresponding constraints active or inactive in the model.

3.1.3. Select from t correlated input variables

The process described in the previous sections can be generalized to cases where more than two variables are correlated. For this purpose, suppose among the m variables known as input variables variables are correlated, and the aim is to select only one of them as input. In this case, model (5) can be rewritten as follows:

$$\begin{aligned}
 &\varphi_k^* = \text{Max } \varphi \\
 \text{s.t. } &\sum_{j=1}^n \lambda_j x_{ij} \leq x_{ik}, \quad i \in ID, \\
 &\sum_{j=1}^n \lambda_j x_{ij} \leq x_{ik} + (1 - \mu_i) M_i, \quad i \in D, \\
 &\sum_{j=1}^n \lambda_j y_{rj} \geq \varphi y_{rk}, \quad r = 1, 2, \dots, s, \quad (7) \\
 &\sum_{j=1}^n \lambda_j = 1, \\
 &\sum_{i \in D} \mu_i = 1, \\
 &\lambda_j \geq 0 \quad \forall j, \mu_i \in \{0, 1\} \quad \forall i.
 \end{aligned}$$

In model (7), D is the set of indexes related to the t correlated input variables, and ID is a set of indexes for independent variables. μ_i variables are the 0-1 variables.

Due to constraint, $\sum_{i \in D} \mu_i = 1$ only one of them can be

applied in the optimal solution of the model. Also M_i considered as vast positive numbers. Therefore in the optimal solution of model (7), only one constraint as related to the correlated variables is considered. As a result, only one of the correlated variables is considered in performance

evaluation. Similarly, model (6) can be extended if the number of correlated outputs is more than two outputs.

4. Selection of correlated variables Using CDEA Models (Second Method)

In Section 3.1, the Basic DEA Models provide the basis for presenting a method for selecting among the correlated variables. As mentioned in section 2.2, there are situations where the CDEA model should be used. So in this section, the selection of correlated variables is based on the CDEA model. The above method is provided for both correlated inputs and correlated outputs.

4.1. Selection from two correlated input variables using the CDEA model

This section presents a 0-1 programming model based on the CDEA model and using it to determine which of the correlated inputs/outputs should be select for evaluating DMUs. Suppose DMU_j , ($j = 1, 2, \dots, n$) each DMU used m inputs (x_{ij}) to produce s output (y_{rj}). Without reducing the generality of the proposed method and in order to simplify, it is assumed that instead of the first input (x_{1j}), the (x'_{1j}) variable can also be considered for evaluating DMUs but there is correlation between these two input variables, namely (x_{1j}) and (x'_{1j}), it is also not possible to combine these two variables and consider a hybrid variable. In such cases, some DMUs maybe agree to selected (x_{1j}) as the first input and others by selected (x'_{1j}). The main question is, "Which of these two variables should be selected as the first input?". To answer this question, 0-1 programming model is integrated with the CDEA model and recommended as follows:

$$\begin{aligned} \varphi^* &= \text{Max } \varphi \\ s.t \quad &\sum_{j=1}^n \sum_{l=1}^n \lambda_{lj} x_{ij} \leq \sum_{j=1}^n x_{ij}, \quad i = 2, \dots, m (\forall_i), \\ &\sum_{j=1}^n \sum_{l=1}^n \lambda_{lj} x_{1j} \leq \sum_{j=1}^n x_{1j} + M_1 (1 - \mu), \\ &\sum_{j=1}^n \sum_{l=1}^n \lambda_{lj} x'_{1j} \leq \sum_{j=1}^n x'_{1j} + M_2 \mu, \quad (8) \\ &\sum_{j=1}^n \sum_{l=1}^n \lambda_{lj} y_{rj} \geq \varphi \sum_{j=1}^n y_{rj}, \quad r = 1, 2, \dots, s, \\ &\sum_{l=1}^n \lambda_{lj} = 1, \forall_j \\ &\lambda_{lj} \geq 0, \mu \in \{0,1\} \end{aligned}$$

Where M_1 and M_2 considered as two vast positive numbers, and the variable μ is a 0-1 variable in the model (8). If it was $\mu^* = 1$ in the optimal solution of this model, the constraint on the first correlated variable (x_{1j}) activated in the model, and the constraint related to input (x'_{1j}) in the model becomes ineffective. Also, if was

$\mu^* = 0$ the opposite would happen, that is mean (x'_{1j}) selected as an input, and the constraint related to (x_{1j}) was disabled in the model. Therefore, firstly, in the optimal solution, one of the two correlated inputs is selected as input. Secondly, from the two correlated input variables, a variable is selected as the input that increases the total efficiency value (efficiency of the CDEA model).

4.2. Selection from two correlated output variables using the CDEA model

A similar method can be used for a state where there are two correlated output variables; Except that in this case, the input-oriented CDEA model is used as follows:

$$\begin{aligned} \theta^* &= \text{Min } \theta \\ s.t \quad &\sum_{j=1}^n \sum_{l=1}^n \lambda_{lj} x_{ij} \leq \theta \sum_{j=1}^n x_{ij}, \quad i = 1, 2, \dots, m, \\ &\sum_{j=1}^n \sum_{l=1}^n \lambda_{lj} y_{rj} \geq \sum_{j=1}^n y_{rj}, \quad r = 2, \dots, s, \\ &\sum_{j=1}^n \lambda_{lj} y_{1j} \geq \sum_{j=1}^n y_{1j} + \mu N_1, \quad (9) \\ &\sum_{j=1}^n \lambda_{lj} y'_{1j} \geq \sum_{j=1}^n y'_{1j} + (1 - \mu) N_2, \\ &\sum_{l=1}^n \lambda_{lj} = 1, \forall_j \\ &\lambda_{lj} \geq 0, \mu \in \{0,1\} \end{aligned}$$

Where N_1 and N_2 considered two tiny negatives numbers and without reducing the generality of the proposed method, it is assumed that y_{1j} and y'_{1j} were two correlated output variables.

4.3. Extend the model (8) to more than two variables

We generalize this process to cases where more than two variables are correlated. Suppose of the m variables known as input variables, t variables are correlated, and the aim is to select only one of them as input. Then rewrite model (8) as follows:

$$\begin{aligned} \varphi^* &= \text{Max } \varphi \\ s.t \quad &\sum_{j=1}^n \sum_{l=1}^n \lambda_{lj} x_{ij} \leq \sum_{j=1}^n x_{ij}, \quad i \in ID \\ &\sum_{j=1}^n \sum_{l=1}^n \lambda_{lj} x_{ij} \leq \sum_{j=1}^n x_{ij} + M_i (1 - \mu_i), \quad i \in D \\ &\sum_{j=1}^n \sum_{l=1}^n \lambda_{lj} y_{rj} \geq \varphi \sum_{j=1}^n y_{rj}, \quad r = 1, 2, \dots, s, \quad (10) \\ &\sum_{l=1}^n \lambda_{lj} = 1, \forall_j \\ &\sum_{i \in D} \mu_i = 1 \\ &\lambda_{lj} \geq 0, \mu \in \{0,1\} \end{aligned}$$

In model (10), D is the set of indexes related to the t correlated input variables, and ID is a set of indexes for

independent variables. μ_i variables are the 0-1 variables, which, due to constraint, $\sum_{i \in D} \mu_i = 1$ only one of them can

be active in the model. Also M_i considered as vast positive numbers. Therefore in the optimal solution of model (10), only one constraint as related to the correlated variables is considered. As a result, only one of the correlated variables is considered. In the same way, model (9) can be extended if the number of correlated outputs is more than two outputs.

Notice that, in the previous sections, only the way to select between correlated inputs and correlated outputs was provided. In the following, a model is presented to select a certain number of variables from the input and output variables based on the proposed model.

5. Refining the variables using the proposed model

The first step for performance evaluation in any research is to identify the variables. If the number of variables was high, the essential variables need to be refined in the next step and used in performance evaluation. There are several methods to do this. These methods include three general categories: 1- Exogenous methods Such as Delphi method and brainstorming that is done using expert opinion. 2- Endogenous methods Such as Shannon entropy which uses the manner and information of the data itself to refine it. 3- Combined methods that both of experts' opinion and their manner data is used. In this section, by applying the proposed method in this study, an endogenous method is proposed based on the DEA efficiency to refine performance evaluation variables. Fig.3 illustrates this method.

For example, the following studies can be mentioned in this field. Fefer et al. [47] Use the Delphi method to identify critical elements for effective and sustainable tourists. Katcher et al. [48] identify and rate home injury hazard risks for children aged 1–5 years using the modified Delphi method. Mohamadi et al. [49] using a fuzzy screening method to identify the effectual factors in the assessment of contractors, and then the weights of criteria were measured through a combination of Fuzzy AHP and fuzzy Shannon's entropy.

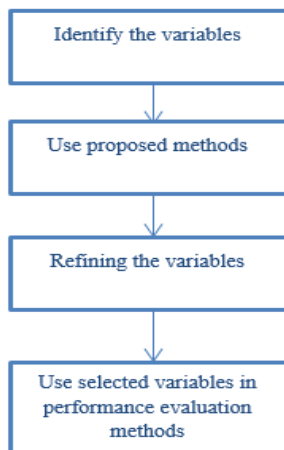


Figure 3. Proposed Framework to refine the variables

In the following, the proposed method in this study is presented to refine the variables using the proposed model. Firstly, the basic DEA Model is the basis for presenting the method, and then, the CDEA model is used. To this end, suppose between m input variables and s the output

variables, k_1 variables as input and k_2 variables as the output should be used in performance evaluation. In this case, model (5) can be rewritten as follows:

$$\begin{aligned}
 &\varphi_k^* = \text{Max } \varphi \\
 &s.t \\
 &\sum_{j=1}^n \lambda_j x_{ij} \leq x_{ik} + M_i (1 - \mu_i), i = 1, 2, \dots, m, \\
 &\sum_{j=1}^n \lambda_j y_{rj} \geq \varphi y_{rk} + N_r (1 - \xi_r), r = 1, 2, \dots, s, \quad (11) \\
 &\sum_{j=1}^n \lambda_j = 1, \\
 &\sum_{i=1}^m \mu_i = k_1 \\
 &\sum_{r=1}^s \xi_r = k_2 \\
 &\lambda_j \geq 0 \forall j, \mu_i, \xi_r \in \{0,1\}
 \end{aligned}$$

In model (11), the μ_i and ξ_i variables are 0-1 variables due to constraint $\sum_{i=1}^m \mu_i = k_1$ only k_1 variables, endue to

constraint, $\sum_{r=1}^s \xi_r = k_2$ only k_2 variables can be applied in the optimal solution of the model. Also, M_i are vast positive numbers and N_r are tiny negative numbers.

Therefore, in the optimal solution of model (11), only k_1 constraints related to the input variables constraints, and only k_2 constraints related to the output variables constraints are considered. As a result, only $k_1 + k_2$ variables are included in the performance evaluation.

The proposed method can be applied for the case between m input variables and s output variables, selection of k_1 variables as input and k_2 variables as output is considered in performance evaluation, presented based on the CDEA model. When using a centralized model, the advantages of this model are stated, including solving a model instead of solving (n) models, and selecting variables that increase the total efficiency value are considered in refining the variables. The proposed model is as follows:

$$\begin{aligned}
 &\varphi^* = \text{Max } \varphi \\
 &s.t \\
 &\sum_{j=1}^n \sum_{l=1}^n \lambda_{lj} x_{ij} \leq \sum_{j=1}^n x_{ij} + M_i (1 - \mu_i), i = 1, 2, \dots, m \\
 &\sum_{j=1}^n \sum_{l=1}^n \lambda_{lj} y_{rj} \geq \varphi \sum_{j=1}^n y_{rj} + N_r (1 - \xi_r), r = 1, 2, \dots, s, \quad (12) \\
 &\sum_{l=1}^n \lambda_{lj} = 1, \forall j \\
 &\sum_{i=1}^m \mu_i = k_1 \\
 &\sum_{r=1}^s \xi_r = k_2 \\
 &\lambda_{lj} \geq 0, \mu_i, \xi_r \in \{0,1\}
 \end{aligned}$$

Also, in the model (12), the μ_i and ξ_i variables are 0-1 variables, according to the constraint $\sum_{i=1}^m \mu_i = k_1$ only k_1 variables, and according to the constraint, $\sum_{r=1}^s \xi_r = k_2$ only k_2 variables can be active in the model. Also, M_i are vast positive numbers and N_r are minimal negative numbers. Thus, in the optimal solution of model (12), only k_1 constraints related to the input variables constraints, and only k_2 constraints related to the output variables constraints are considered. As a result, only $k_1 + k_2$ variables are included in the performance evaluation.

6. Numerical example

In this section, a numerical example to choose from the correlated variables is provided to describe the presented models. This example is adapted from a journal paper [17].As Table 2 shows, the three inputs($I_1, I_2,$ and I_3) and two outputs(O_1 and O_2) are considered for each DMUs. The pairwise correlation between the first and second inputs is 1, between the first and third inputs is 0.97, and between the second and third inputs is 0.97 [17].Therefore, all three input variables are correlated and one of them must be selected. In this example, of both methods, the first method (Using basic DEA models)and the second method(Using the CDEA model)are used in order to select from the correlated input variables. Therefore, models (7) and (10) are used to select one of these three inputs as the only DMUs input. The results of applying model (7) for each of the DMUs are presented in Table 3.

Table2. Inputs and outputs values of numerical example

DMUs	O ₁	O ₂	I ₁	I ₂	I ₃
Unit1	6	7	4	8	4.5
Unit2	10.5	3	6	10	5.5
Unit3	9	2	4	8	4.5
Unit4	8	5	6	10	6.5
Unit5	7	6	5	9	5.5
Unit6	2	8	5	9	4.5
Unit7	12.6	10.5	7	11	7.5
Unit8	4.2	2	2	6	1.5
Unit9	2.25	5.7	3	7	2.5

Table3. Model solution results

DMUs	Selected input	φ_k^* values
Unit1	I ₃	1.08
Unit2	I ₂	1.086
Unit3	I ₁	1
Unit4	I ₁	1.425
Unit5	I ₃	1.332
Unit6	I ₁	1.021
Unit7	I ₁	1
Unit8	I ₂	1
Unit9	I ₃	1

After using the model (7),the input variable does not determine yet, and to determine the desired input from the three correlated inputs must use one of the methods A and B that was introduced in Section 3.1.1.

Method A:Suppose the decision maker is willing to use method A. According to Table 3 input 1 (I_1) 4 times (For Unit 3, Unit 4, Unit 6, Unit 7),Input 2 (I_2) 2 times(For Unit2, Unit8)and input 3 (I_3) 3 times (for Unit 1, Unit 5, Unit 9)have been selected as input. Thus, according to method A, since input 1 has the maximum number of selection, it is selected from the three inputs as the main input for performance evaluation.

Method B:Suppose sets D, D' and D'' represent the set of indexes for the DMUs that select $I_1, I_2,$ and I_3 as the first input variable, respectively. According to the values of the third column of Table 3, $\sum_{k \in D'} \varphi_k^* < \sum_{k \in D''} \varphi_k^* < \sum_{k \in D} \varphi_k^*$ that is mean $2.086 < 3.412 < 4.446$.So I_2 is selected.

In the following, the second method (using the proposed method based on the CDEA model) apply for select one variable as the main input from the three correlated input variables in this example. Therefore, model (10) should be used. After solving this model for the above example data, given that $\mu_1 = 1$ in the optimal solution, as a result, I_1 is selected as the main input for performance evaluation. The results of using the first method (A and B), and the second method are presented in Table 4.Although the method (A) and the second method have the same answer, for method (A) n models must be solved, but for the second method, it is enough to solve a model.

Table4. Results of the first method (A and B) and the second method

methods	method (A)	method (B)	second method
Selected input	I_1	I_2	I_1

7. Case study

In this section, the proposed methods are examined for a set of real data extracted from the paper[50].The information to compare the efficiency performance of the 14 bank branches is presented in Table 5. The outputs used in their study include 17 bank transactions: loan applications, new passbook loans, life insurance sales, new accounts, closed accounts, travelers checks sold, bonds sold, bonds redeemed, deposits, withdrawals, checks cashed, treasury checks issued, B5 checks, loan payments, passbook loan payments, life insurance payments, mortgage payments. In the following management, reduce the number of outputs based on the complexity and resources required was regarded to be approximately the same. Management proposed reducing the 17 transactions to four transaction types (Output 1, Output 2, Output 3, and Output 4).Finally, this comparison is based on three inputs and four outputs. Input 1(I_1): rent (thousands of dollars),Input 2 (I_2): full time equivalent personnel per branch, Input 3 (I_3): supplies (thousands of dollars) and the output 1(O_1) includes: loan applications, new pass-book loans, life insurance sales, Output 2 (O_2): new accounts, closed accounts, Output 3(O_3): travelers checks sold, bonds sold, bonds redeemed, Output 4(O_4): deposits, withdrawals, checks cashed, treasury checks issued, B5 checks, loan payments, passbook loan payments, life insurance payments, mortgage payments.

Table5. 14 Bank branches information

DMU	Input 1	Input 2	Input 3	Output 1	Output 2	Output 3	Output 4
1	140,000	42,900	87,500	484,000	4,139,100	59,860	2,951,430
2	48,800	17,400	37,900	384,000	1,685,500	139,780	3,336,860
3	36,600	14,200	29,800	209,000	1058,900	65,720	3,570,050
4	47,100	9,300	26,800	157,000	879,400	27,340	2,081,350
5	32,600	4,600	19,600	46,000	370,900	18,920	1,069,100
6	50,800	8,300	18,900	272,000	667,400	34,750	2,660,040
7	40,800	7,500	20,400	53,000	465,700	20,240	1,800,250
8	31,900	9,200	21,400	250,000	642,700	43,280	2,296,740
9	36,400	76,000	21,000	407,000	647,700	32,360	1,981,930
10	25,700	7,900	19,000	72,000	402,500	19,930	2,284,910
11	44,500	8,700	21,700	105,000	482,400	49,320	2,245,160
12	42,300	8,900	25,800	94,000	511,000	26,950	2,303,000
13	40,600	5,500	19,400	84,000	287,400	34,940	1,141,750
14	76,100	11,900	32,800	199,000	694,600	67,160	3,338,390

The correlation matrix of the inputs is as Table6[51]:

Table 6. 14 Bankbranches input variables correlation

	Input 1	Input 2	Input 3
Input 1	1	0.31977	0.93579
Input 2	0.31977	1	0.3679
Input 3	0.93579	0.3679	1

Table 6 shows the correlation values between the input variables. Since the correlation between the first and third inputs (rent and supplies) is greater than 0.9, Therefore, there is a correlation between the rent and supplies variables. Thus, one of these two inputs must be selected for use in the DEA model. Since model (5) is to choice between the two inputs correlated variables, so we use that model. Of course, as mentioned, conventional DEA models must be run separately for each DMU. As a result, since there are 14 bank branches (DMUs) in our case study, the model runs 14 times. The results of selecting the input variable for each DMU are shown in Table (7).

Then the manager or decision maker has to decide on the appropriate variable to choose from among the rent and supplies variables. For this purpose, he/she can use methods A or B. The choice of each of these two methods depends on the approach of the manager or decision maker. In method A, the variable frequency is selected. But in method B, The criterion is the sum of the efficiency resulting from the variable selection. According to the results of Table (7), if we use method A, rent variable 9 times (For Unit14, Unit13, Unit11, Unit9, Unit3, Unit4, Unit6, Unit1, Unit2) and supplies variable 5 times (for Unit8, Unit5, Unit7, Unit10, Unit12) have been selected as input. Therefore, because the frequency of choice of rent variable is higher than the supplies variable, this variable is selected. If the manager or decision maker wants to use method B to select the variable, the $\sum \varphi_k^*$ of each variable must be calculated.

This amount according to the results of Table (7) for the rent

variable is 9 and for the supplies variable is 5.672. In output-oriented model if $\varphi_k^* = 1$, the unit under evaluation is efficient, and if $\varphi_k^* > 1$ the unit is inefficient, thus less $\sum \varphi_k^*$ is the variable selection criterion. Therefore, the supplies variable is selected.

In the following, if wanted by the second method (using the proposed method based on the CDEA model), select one of the above-correlated input variables using the model (8). After solving this mode for case study data since in the optimal solution $\mu = 1$, as a result, I_1 (rent variable) is selected. The results of using the first method (A and B), and the second method are presented in Table 8.

Table 7. Model solution results

DMUs	Selected input	φ_k^* values
DMU 1	I_1	1
DMU 2	I_1	1
DMU 3	I_1	1
DMU 4	I_1	1
DMU 5	I_3	1
DMU 6	I_1	1
DMU 7	I_3	1.287
DMU 8	I_3	1.092
DMU 9	I_1	1
DMU 10	I_3	1.089
DMU 11	I_1	1
DMU 12	I_3	1.204
DMU 13	I_1	1
DMU 14	I_1	1

Table 8. Results of the first method (A and B) and the second method

methods	method (A)	method (B)	second method
Selected input	I_1	I_3	I_1

8. Results and Discussion

In this article two general methods for determining an essential variable among the correlated variables have been used. The first method used basic DEA models. For more simplicity and understanding of the proposed method, we first examined the special case where there are two correlated inputs/outputs (section 3.1.1 and section 3.1.2). Then we expanded to more complete case in section 3.1.3. In the first method, the criteria for selecting the essential variable from the correlated variables are two general criteria: 1- A variable that makes more DMUs efficient (Method A). 2- A variable that has the greatest impact on the efficiency of each DMUs (Method B).

The second method used CDEA models. Also in this, for more simplicity and understanding of the second method, we first examined two correlated inputs/outputs selection (section 4.1 and section 4.2). Then we expanded the model to more than two correlated variables in section 4.3. In the second method, the criteria for selecting the essential variable from the correlated variables are the use of total efficiency value of DMUs. That is, a variable is selected that increases the total efficiency of DMUs. The manager or decision maker can also use centralized method based on the case study case. Using this method compared to the previous model has the following advantages:

1. In this method, instead of solving n DEA model, one DEA model is solved. Therefore, the amount of calculations is significantly reduced.
2. In the centralized method, a variable is selected that increases the total efficiency.

It is necessary to mention that in all two general methods, the criterion for selecting the correlated variable is efficiency.

In the following, the application of the proposed methods has been verified for two examples. Finally, a method was proposed to refine the variables using the proposed models. First, the basic DEA model was the basis for presenting the method and then the CDEA model was used (section 5).

9. Conclusions

Understanding the problems of using standard models and providing solutions to solve these problems is essential for useful research. DEA is a technique that is spreading rapidly. One of the major advantages of DEA is its ability to change information on different inputs and outputs into a single measure of efficiency [52]. So, the utility of the DEA model (as a standard and applicable model) depends on its ability to compute the DMUs' relative efficiency using different inputs and outputs. It is a reasonable approach to remove variables that, by their correlations, have the least additional information for the DEA, particularly when we hope that fewer variables lead to better categorization of DMUs [26]. Therefore, determining an essential variable among the correlated variables is very important. Hence in this paper, a method using basic DEA models is presented to solve this problem. In this way, the basic DEA models were integrated with the 0-1 programming model to achieve the above objective. For this purpose, first an algorithm for selecting between two correlated input variables and then

for selecting from between two correlated output variables using basic DEA models were presented. Also, the described process was generalized to cases where more than two correlated input/output variables. Then this method was developed to select between two correlated input/output variables and then to select from more than two correlated variables using the CDEA model. Thus, in the optimal solution of the developed CDEA model, from the two correlated inputs variable, a variable is selected as the input that increases the total efficiency value (efficiency derived from the CDEA model). Finally, using the proposed method in this study, a method based on the efficiency of DEA was presented to refine performance evaluation variables. For this purpose, first the basic DEA Model was the basis for presenting the method, and then, the CDEA model was used. The results showed that the proposed method has several advantages. It is easy to use, and implementation, and there is no computational complexity. Computational complexity means the existence of big data and the use of supercomputers to solve models, while the proposed method does not require advanced software equipment to solve the models. Also, the presented method does not have the complexity of statistical topics. It also does not need experts' judgment, so it is a cost-effective way. Another advantage of the proposed method is that it can be easily used for other types of input-oriented or output-oriented DEA models with variable returns to scale or constant returns to scale.

Researchers can use the proposed method in various aspects of future research. Considering different datasets, such as ambiguous, negative, or fuzzy data, can be interesting research topics. Other DEA models with correlated variables can also be studied. The presented method can be used in other DEA application areas such as manufacturing, universities, agriculture, and other organizations. For future research, we suggest a framework considering in the modeling and selection variables one step with the experts. In this case, it is possible to conduct a comparison with the method (free of judgment) and was suggested by the experts. Instead of the criteria for selecting the correlated variable in the first method (Method A and Method B), other criteria can be considered as future research and the results can be compared with this research.

References

- [1] Charnes, A., Cooper, W.W. and Rhodes, E, "Measuring the efficiency of decision making units". *European Journal of Operational Research*, Vol. 2 No. 6, 1978, 429–444.
- [2] Emrouznejad, A. and Yang, G. Liang, "A survey and analysis of the first 40 years of scholarly literature in DEA: 1978–2016". *Socio-Economic Planning Sciences*, Elsevier Ltd, Vol. 61, 2018, 4–8.
- [3] Alpay, O. and Akturk, E, "Copula approach to select input / output variables for DEA". *An International Journal of Optimization and Control: Theories & Applications*, Vol. 7 No. 1, 2017, 28–34.
- [4] Nataraja, N.R. and Johnson, A.L, "Guidelines for using variable selection techniques in data envelopment analysis". *European Journal of Operational Research*, Elsevier B.V., Vol. 215 No. 3, 2011, 662–669.

- [5] López, F.J., Ho, J.C. and Ruiz-Torres, A.J., "A computational analysis of the impact of correlation and data translation on DEA efficiency scores". *Journal of Industrial and Production Engineering*, Vol. 33 No. 3, 2016, 192–204.
- [6] Xia, M. and Chen, J.X., "Data Envelopment Analysis Based on Choquet Integral". *International Journal of Intelligent Systems*, Vol. 32 No. 12, 2017, 1312–1331.
- [7] Pedraja-Chaparro, F., Salinas-Jiménez, J. and Smith, P., "On the quality of the data envelopment analysis model". *Journal of the Operational Research Society*, Vol. 50 No. 6, 1999, 636–644.
- [8] Dong, F., Mitchell, P.D. and Colquhoun, J., "Measuring farm sustainability using data envelope analysis with principal components: The case of Wisconsin cranberry". *Journal of Environmental Management*, Elsevier Ltd, Vol. 147, 2015, 175–183.
- [9] Farzipoor Sean, R., Memariani, A. and Lotfi, F.H., "The effect of correlation coefficient among multiple input vectors on the efficiency mean in data envelopment analysis". *Applied Mathematics and Computation*, Vol. 162 No. 2, 2005, 503–521.
- [10] Lewin, A.Y., Morey, R.C. and Cook, T.J., "Evaluating the administrative efficiency of courts". *Omega*, Vol. 10 No. 4, 1982, 401–411.
- [11] Seifert, L.M. and Zhu, J., "Identifying excesses and deficits in Chinese industrial productivity (1953-1990): A weighted data envelopment analysis approach". *Omega*, Vol. 26 No. 2, 1998, 279–296.
- [12] Smith, P., "Model misspecification in Data Envelopment Analysis". *Annals of Operations Research*, Vol. 73, 1997, 233–252.
- [13] Sueyoshi, T., "Estimation of stochastic frontier cost function using data envelopment analysis: An application to the at& divestiture". *Journal of the Operational Research Society*, Vol. 42 No. 6, 1991, 463–477.
- [14] Thanassoulis, E., "DEA and its use in the regulation of water companies". *European Journal of Operational Research*, Vol. 127 No. 1, 2000, 1–13.
- [15] Charnes, A., Cooper, W.W. and Sueyoshi, T., "A Goal Programming/Constrained Regression Review of the Bell System Breakup". *Management Science*, Vol. 34 No. 1, 1988, 1–26.
- [16] Kao, C., Chang, P. and Hwang, S.N., "Data Envelopment Analysis in Measuring the Efficiency of Forest Management". *Journal of Environmental Management*, Vol. 38 No. 1, 1993, 73–83.
- [17] Dyson, R.G., Allen, R., Camanho, A.S., Podinovski, V. V., Sarrico, C.S. and Shale, E.A., "Pitfalls and protocols in DEA". *European Journal of Operational Research*, Vol. 132 No. 2, 2001, 245–259.
- [18] Kao, L.J., Lu, C.J. and Chiu, C.C., "Efficiency measurement using independent component analysis and data envelopment analysis". *European Journal of Operational Research*, Elsevier B.V., Vol. 210 No. 2, 2011, 310–317.
- [19] Ueda, T. and Hoshiai, Y., "Application of principal component analysis for parsimonious summarization of DEA inputs and/or outputs". *Journal of the Operations Research Society of Japan*, Vol. 40 No. 4, 1997, 477–478.
- [20] Adler, N. and Golany, B., "Evaluation of deregulated airline networks using data envelopment analysis combined with principal component analysis with an application to Western Europe". *European Journal of Operational Research*, Vol. 132 No. 2, 2001, 260–273.
- [21] Adler, N. and Golany, B., "Including principal component weights to improve discrimination in data envelopment analysis". *Journal of the Operational Research Society*, Vol. 53 No. 9, 2002, 985–991.
- [22] Dario, C., Simar, L., *Advanced Robust and Nonparametric Methods in Efficiency Analysis*, Springer Verlag, US, 2007, p. XXII -248.
- [23] Pastor, J.T., Ruiz, J.L. and Sirvent, I., "A Statistical Test for Nested Radial Dea Models". *Operations Research*, Vol. 50 No. 4, 2002, 728–735.
- [24] Banker, R.D., "Hypothesis tests using data envelopment analysis". *Journal of Productivity Analysis*, Vol. 7 No. 2–3, 1996, 139–159.
- [25] Sirvent, I., Ruiz, J.L., Borrás, F. and Pastors, J.T., "A Monte Carlo evaluation of several tests for the selection of variables in DEA models". *International Journal of Information Technology and Decision Making*, Vol. 4 No. 3, 2005, 325–343.
- [26] Jenkins L. and Anderson M., "A multivariate statistical approach to reducing the number of variables in data envelopment analysis". *European Journal of Operational Research*, Vol. 147, 2003, 51–61.
- [27] Adler, N. and Yazhemy, E., "Improving discrimination in data envelopment analysis: PCA-DEA or variable reduction". *European Journal of Operational Research*, Elsevier B.V., Vol. 202 No. 1, 2010, 273–284.
- [28] Ruggiero, J., "Impact assessment of input omission on DEA". *International Journal of Information Technology and Decision Making*, Vol. 4 No. 3, 2005, 359–368.
- [29] Fanchon, P., "Variable selection for dynamic measures of efficiency in the computer industry". *International Advances in Economic Research*, Vol. 9 No. 3, 2003, 175–188.
- [30] Simar, L. and Wilson, P.W., "Testing restrictions in nonparametric efficiency models". *Communications in Statistics Part B: Simulation and Computation*, Vol. 30 No. 1, 2001, 159–184.
- [31] Ji, A.B., Chen, H., Qiao, Y. and Pang, J., "Data envelopment analysis with interactive fuzzy variables". *Journal of the Operational Research Society*, Taylor & Francis, Vol. 0 No. 0, 2018, 1–9.
- [32] Li Y , Shi X , Yang M , Liang L . "Variable selection in data envelopment analysis via akaike's information criteria". *Annal Oper Res*, 253(1) 2017,453–76.
- [33] Wagner J , Shimshak D . "Stepwise selection of variables in data envelopment analysis: procedures and managerial perspectives". *Eur J Oper Res*, 180(1) ,2007,57–67.
- [34] Morita, H. and N. K. Avkiran., "Selecting inputs and outputs in data envelopment analysis by designing statistical experiments". *Journal of the Operations Research Society of Japan*, 52(2), 2009,163-173.
- [35] Limleamthong, P. and G. Guillen-Gosalbez., "Mixed-integer programming approach for dimensionality reduction in data envelopment analysis: Application to the sustainability assessment of technologies and solvents". *Industrial & Engineering Chemistry Research*, 57, 2018, 9866–9878.
- [36] Benítez-Peña, S., P. Bogetoft, and D. R. Morales., "Feature selection in data envelopment analysis: A mathematical optimization approach". *Omega*. Volume 96, 2020, 102068.
- [37] Peyrache, A., Rose, C., & Sicilia, G., "Variable selection in Data Envelopment Analysis". *European Journal of Operational Research*. Volume 282, Issue 2, 2020, 644-659.
- [38] Bastani M, Ketabi S, Maddahi R, Ahari RM. "Efficient Resource Allocation to Social Security Organization Hospitals in Iran by Using Centralized Data Envelopment Analysis". *J Health Man & Info*, 7(1), 2020, 59-67.
- [39] Al-Refaie, A., Najdawi, R., Sy, E., "Using DEA window analysis to measure efficiencies of blowing machines in plastics industry". *Jordan Journal of Mechanical and Industrial Engineering*. Volume 10 Number 1, 2016, 27- 38.
- [40] Mahmoud, I.A., Fahmyaly, M., Mohib, A., Afefy, I.H., "Integration of Benchmarking with Overall Equipment Cost Loss for Industrial Process Improvement". *Jordan Journal of Mechanical and Industrial Engineering*. 13. 2019, 49 - 59.

- [41] Banker, R.D., Charnes, A. and Cooper, W.W., "Some Models for Estimating Technical and Scale Inefficiencies in Data Envelopment Analysis". *Management Science*, Vol. 30 No. 9, 1984, 1078–1092.
- [42] Lozano, S. and Villa, G., "Centralized resource allocation using data envelopment analysis". *Journal of Productivity Analysis*, Vol. 22 No. 1–2, 2004, 143–161.
- [43] Giménez-García, V.M., Martínez-Parra, J.L. and Buffa, F.P., "Improving resource utilization in multi-unit networked organizations: The case of a Spanish restaurant chain". *Tourism Management*, Vol. 28 No. 1, 2007, 262–270.
- [44] Mar-Molinero, C., Prior, D., Segovia, M.M. and Portillo, F., "On centralized resource utilization and its reallocation by using DEA". *Annals of Operations Research*, Vol. 221 No. 1, 2014, 273–283.
- [45] Lozano, S., Villa, G. and Adenso-Díaz, B., "Centralised target setting for regional recycling operations using DEA". *Omega*, Vol. 32 No. 2, 2004, 101–110.
- [46] Asmild, M., Paradi, J.C. and Pastor, J.T., "Centralized resource allocation BCC models". *Omega*, Vol. 37 No. 1, 2009, 40–49.
- [47] Fefer, J.P., De-Urioste Stone, S., Daigle, J. and Silka, L., "Using the Delphi Technique to Identify Key Elements for Effective and Sustainable Visitor Use Planning Frameworks". *SAGE Open*, Vol. 6 No. 2, 2016, 1–16.
- [48] Katcher, M. L., Meister, A. N., Sorkness, C. A., Staresinic, A. G., Pierce, S. E., Goodman, B. M., Peterson, N. M., Hatfield, P. M., Schirmer, J. A., "Use of the modified Delphi technique to identify and rate home injury hazard risks and prevention methods for young children". *Injury prevention : journal of the International Society for Child and Adolescent Injury Prevention*, Vol. 12 No. 3, 2006, 189–194.
- [49] Mohamadi, S., Ebrahimi, A. and Alimohammadlou, M., "An application of fuzzy screening, fuzzy AHP and fuzzy Shannon's entropy on identification and prioritisation of effective factors in assessment of contractors in Fars Electric Power Distribution Company, Iran". *International Journal of Procurement Management*, Vol. 10 No. 2, 2017, 194–226.
- [50] Sherman, H.D. and Gold, F., "Evaluation with Data Envelopment Analysis". Vol. 9, 1985, 297–315.
- [51] Ji, A., Liu, H., Qiu, H.J. and Lin, H., "Data envelopment analysis with interactive variables". *Management Decision*, Vol. 53 No. 10, 2015, 2390–2406.
- [52] Gilsa, C.V., Lacerda, D.P., Camargo, L.F.R., Souza, I.G. and Cassel, R.A. "Longitudinal evaluation of efficiency in a petrochemical company". *Benchmarking: An International Journal*, Vol. 24 No. 7, 2017, 1786-1813.

Study of the Effect of some Deflector's Geometry Factors on the Reduction of the Aerodynamic Drag of the Car Model

Mohamed MAINE^{a*}, Mohamed EL OUMAMI^b, Otmane BOUKSOUR^b, Boujemâa NASSIRI^c

^aHigher National School of Electricity and Mechanics, University Hassan II of Casablanca, Road of El Jadida, km 7, PB: 8118, Oasis, Casablanca, Morocco.

^bLaboratory of Production, Mechanics and Industrial Engineering, Higher School of Technology, University Hassan II of Casablanca, km 7, PB: 8118, Oasis, Casablanca, Morocco.

^cSustainable Innovation and Applied Research Laboratory, Universtapolis, Bab Al Madina, Tilila, P.B: 8143, Agadir, Morocco.

Received April 15 2021

Accepted June 23 2021

Abstract

In this article, passive flow control around a generic car model has been investigated numerically. A deflector installed on the rear window of the Ahmed model at 25° was used to study the aerodynamic effect. The study involves the analysis of a set of eight two-level deflector-related factors with the aim of assessing their effects on aerodynamic drag. The assays were determined by establishing a Plackett-Burman screening plan and the results are studied by JMP Pro 14 software. It was observed that the factors (type of deflector, inlet velocity and length's ratio) have a significant effect on reducing aerodynamic drag. The optimal test conditions proposed by the Plackett-Burman plan were investigated numerically and the value obtained was slightly higher than the value of the screening design. It was concluded that the model of Ahmed with optimal deflector gives the best drag reduction, compared to the model without deflector. Installing the optimal deflector on Ahmed's body widens the wake area and eliminates chainstay vortex.

© 2021 Jordan Journal of Mechanical and Industrial Engineering. All rights reserved

Keywords: Aerodynamic drag, Generic car, Ahmed model, Deflector, Plackett-Burman plan;

Nomenclature

<i>ANN</i>	Artificial Neural Network
<i>ANOVA</i>	Analysis Of Variance
<i>CFD</i>	Computational Fluid Dynamic
<i>CPU</i>	Central Processing Unit
<i>EARSM</i>	Explicit Algebraic Reynolds Stress Model
<i>RANS</i>	Reynolds Average Navier-Stokes
<i>RSM</i>	Response Surface Method
<i>SST</i>	Shear stress transport
<i>L</i>	Ahmed body length
<i>W</i>	Ahmed body width
<i>l_D</i>	Deflector's length
<i>w_D</i>	Deflector's width
<i>Th</i>	Deflector's thickness
<i>θ</i>	Deflector's angle of inclination
<i>α</i>	Ends angle of the deflector
<i>C_D</i>	Drag coefficient
<i>C_L</i>	Lift coefficient
<i>U₀</i>	Inlet velocity
<i>S_x</i>	Projected area in x direction
<i>ρ</i>	Specific density of the air
<i>k</i>	Turbulent kinetic energy
<i>ω</i>	Specific dissipation rate
<i>ε</i>	Dissipation rate
<i>μ_t</i>	Turbulent viscosity
<i>R²</i>	Coefficient of determination

1. Introduction

The current energy and environmental context requires the search for effective strategies to reduce the energy consumption of ground vehicles. Researchers in the automotive industry have developed methods of modifying the flow around a car [1]. These techniques are mainly divided into two categories, namely: active control and passive control [2]. The first method is to change the shape of the vortices in the wake area, adding additional energy using an instrument installed in a specific location on the vehicle body. Among the active control methods we can cite: synthetic jets [3]; micro-jets with regular blowing [4]; aspiration [5]; fluidic oscillators [6]; Plasma actuator [7] and winglet devices [7, 8].

The passive flow control method involves modifying the flow around the vehicle by adding devices in specific locations. This method uses several techniques: deflectors [10]; rear plates [11]; lateral guide vanes [12]; underbody diffuser [13]; vortex generators [14]; streaks [15]; non-smooth surface [16]; jet boat tail [17]; linking tunnels [18] and rounded edges [19].

There are also several coupled control techniques, namely: Coanda jet effect [20]; ventilation in the slots [21]; blowing and variations of the front geometry [22] and vortex generator network and rear spoiler [23]. Compared to active control, passive control methods do not require sophisticated actuators and electronic control systems,

* Corresponding author e-mail: mmdmaine@gmail.com.

which ensures greater reliability. In addition, passive control methods have another obvious advantage since they do not require any power supply [24]. In this article, we are interested in using the deflector with optimal parameters as a passive method of reducing aerodynamic drag of cars.

Significant optimization efforts have been made around ground vehicles to minimize the aerodynamic drag. (Krajnovic) [25] used the Response Surface Method (RSM) for aerodynamic optimization of the flow around a train. The overall optimization of the drag coefficient and crosswind stability was obtained by applying the genetic algorithm on the polynomials of the response surface methodology. (Zheng et al.) [26] used artificial neural networks (ANNs) formed by a relatively small number of CFD simulations for aerodynamic optimization. It was found that the ANN approximation reduces the cost of calculations.

(Beigmoradi et al) [27] studied the optimization of the rear of Ahmed model taking into account aerodynamic and acoustic objectives. The Taguchi method with four factors was chosen to reduce the number of simulations. (Wang et al.) [16] performed numerical studies to investigate the reduction in aerodynamic drag of Ahmed model using a fitted non-smooth surface. An aerodynamic optimization method based on a Kriging substitution model was used to design the non-smooth honeycomb surface. Four structure parameters were selected as design variables, and a 16-level experimental design method based on orthogonal tables was used to analyze the sensitivities and influences of the variables on the drag coefficient.

This article looks at the study of the variation of a set of parameters related to the deflector installed on the rear window of Ahmed's model. The Plackett and Burman plan is used to optimize testing in an experiment design method. To our knowledge, this is the first time such an approach has been used to determine the factors that influence aerodynamic drag.

2. Studied model

2.1. Ahmed model

The complexity of the study of flows around cars requires a simple and standard model to compare the results of different numerical and experimental studies. (Ahmed et al.) proposed a simplified road vehicle model for better analysis and understanding of three-dimensional airflows around the vehicle [28]. Several authors have used Ahmed's model as a reference to study the aerodynamics of road vehicles. It is a generic car geometry comprising a front plate with rounded parts and a sloping rear top surface. The slant angle is adjustable and is the main variable parameter of the model in the experimental research of (Ahmed et al.). Most of the body drag is due to the pressure drag triggered from the rear. The wake structure is very complex with a parting zone and counter-rotating vortices generated at the intersection between the back bank angle and the side edges. The dimensions of the Ahmed model are $1044 \times 389 \times 288$ mm. The bottom surface of Ahmed's model is 50 mm above

the ground, and four feet are used to support the model. The origin of the coordinates is fixed to the ground at the midpoint of the rear face and the directions of the coordinates are as in Figure 1. In this way, the rear base is tilted 25° .

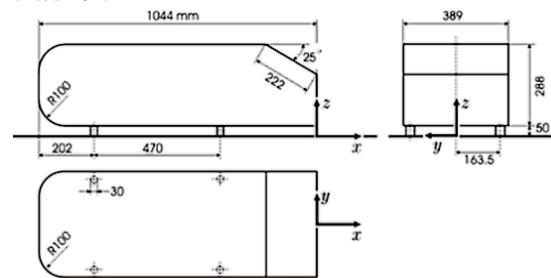


Figure 1. Dimensions of Ahmed model [28].

2.2. Deflector

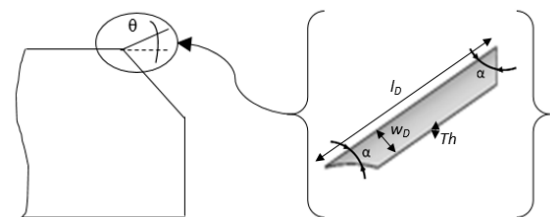


Figure 2. Deflector installed at on the rear slant of Ahmed model

The deflector is a device installed on the rear window of the Ahmed model. It has a length ratio (l_D/L), a width ratio (w_D/W) and a thickness (Th); l_D , w_D , L and W are respectively, the length, the width of the deflector, the length and the width of the Ahmed model. The ends of the deflector are cut with an angle α . The deflector's angle of inclination is θ (Figure 2).

In recent years, various works have been carried out around the deflector. (Fourrié et al.) [10] and (Hanfeng et al.) [24] carried out an experimental study on the deflector installed at the rear slant of the Ahmed model for Reynolds numbers between 7.7×10^5 and 8.7×10^5 . (Raina et al.) [29,30] carried out a numerical study using the RANS model with two different turbulence equations (SST $k-\omega$ and $k-\epsilon$), for Reynolds numbers between 7.7×10^5 and 9.4×10^5 . (Fourrié et al.) [10] and (Raina et al.) [29,30] used a 1:1 scale model; while (Hanfeng et al.) [24] have used a 1:2 scale model. The deflector's angle varied from 0° to 5° . The obtained reduction in aerodynamic drag is between 6.6 and 11.8 % compared to their references values cited in Table 1.

The values of the drag coefficient obtained from the two turbulence models are very different. Perhaps this variation is due to the lack of prediction of the near wall sublayer. It has been observed that the drag is influenced by the angle of inclination of the deflector and the Reynolds number. In these studies, the authors used a straight deflector. Their decision variables are mainly the angle of inclination and the flow velocity. They suggest that flow control on such geometries should take into account any flow structures that contribute to wake flow.

Table 1. Research work on the Ahmed model with deflector

Author, year	Fourrié, 2011 [10]	Hanfeng, 2016 [24]	Raina, 2017 [29]	Raina, 2018 [30]
Model	Ahmed model with rear slant angle of 25°			
Deflector's angle	5°	0°	5°	5°
Deflector's dimension	389×20×1.2	194.5×10×1.2	389×20×1.2	
Study	Experimental		Numerical	
Turbulence equations	--	--	SST k- ω	k- ϵ
Re	7.7×10 ⁵	8.7×10 ⁵	7.7×10 ⁵	9.4×10 ⁵
U ₀ (m.s ⁻¹)	40	25	40	50
C _D	0.259	0.381	0.318	0.271
Reference *	0.285	0.432	0.340	0.290
% reduction	9 %	11.8 %	7 %	6.6 %

* C_D for Ahmed model with rear slant angle of 25° without deflector

3. Mathematical model

3.1. RANS turbulence models

3.1.1. Reynolds average

This average describes the velocity fields statistically. The turbulent flow is divided into two terms (Eqn. 1):

$$u_i = U_i + u'_i \quad (1)$$

Where U_i is the average value of the freestream velocity and u'_i is its fluctuation compared to the average value U_i (with $U_i = \bar{u}_i$ and $\bar{u}'_i = 0$).

The average of this decomposition therefore makes it possible to remove the fluctuating variables. The average was applied to the continuity and Navier-Stokes equations for incompressible flow by decomposing the variables u and P . These equations are given in Eqn. 2 and Eqn. 3.

$$\frac{\partial U_i}{\partial x_i} = 0 \quad (2)$$

$$\frac{\partial U_i}{\partial t} + U_j \frac{\partial U_i}{\partial x_j} = -\frac{1}{\rho} \frac{\partial P}{\partial x_i} + \nu \frac{\partial^2 U_i}{\partial x_i \partial x_j} - \frac{\partial \overline{u'_i u'_j}}{\partial x_j} \quad (3)$$

Where ρ the specific density, P the average value of the pressure and ν the kinematic viscosity of the fluid. An additional term appeared, namely in Eqn. 4:

$$-\frac{\partial \overline{u'_i u'_j}}{\partial x_j} \quad (4)$$

One approach for closing these equations is to use the Boussinesq approximation defined in Eqn. 5:

$$-\rho \overline{u'_i u'_j} = \mu_t \left(\frac{\partial u_i}{\partial x_j} + \frac{\partial u_j}{\partial x_i} \right) - \frac{2}{3} \left(\rho k + \mu_t \frac{\partial u_k}{\partial x_k} \right) \delta_{ij} \quad (5)$$

Where, μ_t is the turbulent viscosity, k is the turbulent kinetic energy and δ_{ij} is the Kronecker symbol. The turbulent viscosity μ_t can be obtained by solving additional transport equations. The number of these equations depends on the chosen turbulence model. In this work, the emphasis will be on the k- ω (SST) model [31].

3.1.2. Turbulence model k- ω (SST)

The k- ω SST (Shear Stress Transport) model developed by (Menter, 1994) combines the precision of the k- ω model in the near wall and the k- ϵ model in the far field region. Such an approach was made by transforming the model k- ϵ into a k- ω formulation with the addition of a blending function between the two regions [32]. The k- ω (SST) model is capable of modeling a wide range of flow profiles with increased precision. The transport equations for the k- ω (SST) model are given by the Eqn. 6 and the Eqn.7.

$$\frac{\partial}{\partial t} (\rho k) + \frac{\partial}{\partial x_i} (\rho k u_i) = \frac{\partial}{\partial x_j} \left[\Gamma_k \frac{\partial k}{\partial x_j} \right] + \tilde{G}_k - Y_k \quad (6)$$

$$\frac{\partial}{\partial t} (\rho \omega) + \frac{\partial}{\partial x_i} (\rho \omega u_i) = \frac{\partial}{\partial x_j} \left[\Gamma_\omega \frac{\partial \omega}{\partial x_j} \right] + G_\omega - Y_\omega + D_\omega \quad (7)$$

\tilde{G}_k and G_ω represent the production conditions of k and ω . Y_k and Y_ω represent the terms of dissipation of k and ω . Γ_k and Γ_ω represent the effective diffusivity of k and ω . Finally, D_ω represents the term of cross diffusion. The turbulent kinetic energy k and specific dissipation rate ω are determined as in the Eqn. 8 and the Eqn.9. These equations are used to calculate the initial conditions parameters.

$$k = \frac{3}{2} (U_0 I)^2 \quad (8)$$

$$\omega = \rho \frac{k}{\mu} \left(\frac{\mu_t}{\mu} \right)^{-1} \quad (9)$$

Where U_0 is the mean velocity and I the turbulence intensity defined as the ratio of the root-mean-square of the velocity fluctuations u'_i to the mean flow velocity U_i . A blending function F_1 , between the near wall region and the far field was integrated in the terms of the production derivation, dissipation, diffusivity and cross diffusion as in Eqn 10.

$$\phi = F_1\phi_1 + (1 - F_1)\phi_2 \quad (10)$$

Where ϕ_1 regroup all the constants of the original k- ω model and ϕ_2 regroup all the constants of the transformed k- ϵ model. ϕ is the resulting constant of the model and F_1 is the blending function, which is equal to one in the near wall and zero far from the surface.

3.2. Aerodynamics coefficients

Determining the air stresses on the car consists in measuring the main component of the aerodynamic torsor, which is the drag coefficient. It is the ratio of the aerodynamic torsor, to the dynamic pressure relative to the reference velocity, over the projected area in the main direction of flow. It is defined as:

$$C_D = \frac{F_x}{\frac{1}{2}\rho U_0^2 S_x} \quad (11)$$

4. Numerical study

4.1. Geometry and mesh of the 3D model

A 3D model was created and simulated on the ANSYS software. Since steady flow was assumed, a XOZ symmetry plane was used to cut the model in half to reduce the computational time. The dimensions of the simulation area are $11044 \times 1194.5 \times 1839$ mm. The upstream and downstream boundary distances from the body were respectively 3.26 L and 6.32 L. The upper wall of the far field is 1.5 L and the width of the domain is 1 L (where L is the length of the model). These dimensions are recommended by ERCOFTAC in the modeling of refined turbulence [33]. The dimensions of the computation domain imply a blocking factor equal to 5.23%. To capture the flow on the boundary layer, a coefficient of $y^+ = 1$ was chosen. The rate of expansion of the mesh starting from the boundary layer of the model is 1.2. The mesh elements are hexahedral near the model contours and the bottom wall of the domain, and tetrahedral in the far field region (Figure 3). The boundary conditions are presented in Table 2. Numerical calculations were carried out on a CPU of 3 processors and 8 GB of RAM. The residuals of the equations of continuity, velocity and k- ω are limited to 10^{-6} . The second-order upwind scheme was employed for the terms of the momentum and turbulence closure model equations [34].

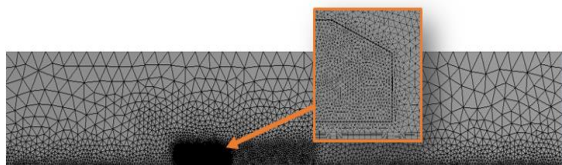


Figure 3. Mesh of the domain around Ahmed's model

Table 2. Boundary conditions

Zone	Boundary conditions	Inputs parameters
Upstream	Velocity-Inlet	$u_x = U_0$; $u_y = 0$; $u_z = 0$
Downstream	Pressure-Outlet	free
Road	Wall	u_x ; u_y ; $u_z = 0$
Top	Wall	u_x ; u_y ; $u_z = 0$
Symmetry	Symmetry	$u_x = U_0$; $u_y = 0$
Side	Wall	u_x ; u_y ; $u_z = 0$
Ahmed model	Wall	u_x ; u_y ; $u_z = 0$

4.1. Study of the mesh sensitivity

To ensure an independent solution of the mesh for all the simulations, a sensitivity study was carried out on the model of Ahmed without deflector, for the Reynolds number of 7.89×10^5 . Three types of meshes M1, M2 and M3 were used and are coarse, medium and fine mesh, respectively. The percentage difference in the drag coefficient (C_D) between two successive meshes was less than 3% (Table 3). For M2 (664 818 elements), increasing the number of elements by 53.1% to obtain M3 (1 417 521 elements), gives 2.88 % change in (C_D). Globally, a mesh independence solution was obtained for M2. Therefore, this mesh will be used for all other simulations.

Table 3. Mesh sensitivity

Mesh	No. elements	Drag coefficient (C_D)	Difference
M1	287 819	0.3001	6.07 %
M2	664 818	0.2819	2.88 %
M3	1 417 521	0.2738	--

4.2. Comparison with literature

For a Reynolds number $Re = 7.89 \times 10^5$ corresponding to the inlet velocity $U_0 = 40 \text{ m.s}^{-1}$, the value of the mean mesh (M2) is compared with the data in the literature (Table 4). The differences of the drag coefficient obtained compared to (Thomas and Agarwal) k- ω SST [35] and (Guilmineau et al.) EARSM [36] are respectively 2.46 % and 0.53 %. These values may be due to the refinement of the mesh and the difference in the number of elements used. For the experimental data, a difference of 1.09 % was observed compared to (Ahmed et al.) [28] and of 5.92 % compared to (Meile et al.) [37].

Table 4. Comparison of the drag coefficient obtained with the literature

Type of study	Drag coefficient (C_D)
Present work	0.2819
(Thomas et Agarwal) k- ω SST [35]	0.2890
(Guilmineau et al.) EARSM [36]	0.2804
(Ahmed et al.) [28]	0.2850
(Meile et al.) [37]	0.2990

5. Optimal simulation plan

5.1. Plackett-Burman Plan Concept

Plackett-Burman plan is generally 2-level, resolution III screening designs. In this category of design, the main

effects are aliased with the two-factor interactions. The design of the Plackett-Burman plan is an efficient screening method for identifying the important factors among a large number of factors that influence a Y response [38].

5.2. Definition of factors

Eight factors were raised on the deflector installed on the rear window of Ahmed's body, namely: i) Length ratio (A); ii) Width ratio (B); iii) Thickness (C); iv) Ends angle (D); v) Angle of inclination (E); vi) Type of curvature (F); vii) Radius of curvature (G) and viii) Inlet velocity (H). Each factor was evaluated based on two levels: (-1) for the low level and (+1) for the high level (Table 5).

The choice of these factors, as well as their levels, is obtained mainly from the preliminary study carried out as well as the bibliographic data of previous works [8,24,29,30]. The application of the Plackett-Burman model in current research has identified a series of 12 parameter combinations to be analyzed on the ANSYS simulation software to optimize the deflector. JMP Pro 14 software was used for the experimental design and data analysis of the model. Figure 4 summarizes the 12 tests of the Plackett-Burman plan selected. The 3D drawings of the Ahmed model with deflector, of the different configurations are made by the CAD software SolidWorks.

Table 5. Levels of factors tested by the Plackett-Burman plan

ID	Factors	Symbol	Numerical Value	
			Low Level (-)	High Level(+)
A	Length Ratio	l_D/L [%]	3	6
B	Width Ratio	w_D/W [%]	50	100
C	Thickness	Th [m]	0.001	0.005
D	Ends angle	α [°]	0	45
E	Angle of inclination	θ [°]	-5	5
F	Type of curvature	CO	Concave	Convex
G	Radius of Curvature	R [m]	0.05	0.5
H	Inlet velocity	U_0 [m.s ⁻¹]	20	40

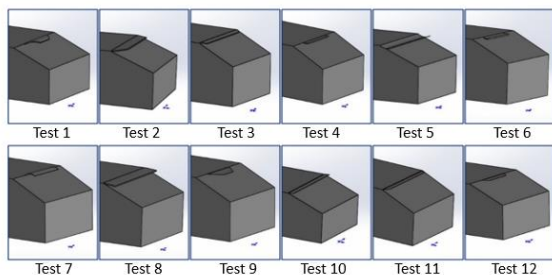


Figure 4. Deflector installed on the rear slant of the Ahmed model according to the 12 tests provided by the Plackett-Burman plan.

6. Results and Discussion

Statistical analysis of the obtained results was performed to evaluate the analysis of the variance between factors (ANOVA). The analysis includes the

Fisher Snedecor test (F test), its associated probability P(F), and the coefficient of determination (R^2), which measures the fit quality of the regression model. The experimental design as well as data analysis of the model were carried out via the JMP Pro 14 software.

6.1. Matrix of Experiences

Table 6 presents the model matrix of the simulation and forecast results after a numerical study on the ANSYS simulation software of the various tests given by the Plackett-Burman plan. From the results obtained, it can be seen that the best simulation conditions leading to a remarkable drag coefficient ($C_D = 0.2624$) were observed during the following combination: length ratio (6 %); width ratio (50 %); thickness (0.001 m); ends angle (0 °); angle of inclination (5 °); type of curvature (Concave); radius curvature (0.05 m) and inlet velocity (40 m.s⁻¹). This configuration is associated to a predicted value of response at the level of the aerodynamic drag ($C_D = 0.2618$).

Table 6. Matrix of test results established by the Plackett-Burman plan

TEST	Drag Coefficient	
	Simulation result	Predicted result
1	0.2673	0.2679
2	0.2746	0.2753
3	0.2699	0.2682
4	0.2847	0.2830
5	0.2818	0.2814
6	0.2776	0.2793
7	0.2624	0.2618
8	0.2686	0.2690
9	0.2782	0.2775
10	0.2653	0.2659
11	0.2841	0.2845
12	0.2734	0.2741

6.2. Quality assessment of the numerical model

Figure 5 shows a linear regression analysis of the observed drag coefficient values obtained by numerical simulation using ANSYS Fluent, versus predicted values of the JMP Pro 14. There is a regular and close distribution of the numerical values on either side of the theoretical line. It is observed that the value of $R^2 = 0.9813$ and adjusted $R^2 = 0.9313$ are significantly very close, this justifies that the value of the observed variation is explained by the direct effects of factors. Furthermore, the value of R^2 , which is very close to one, shows that the chosen Plackett-Burman plan has a high quality in the level of fitting.

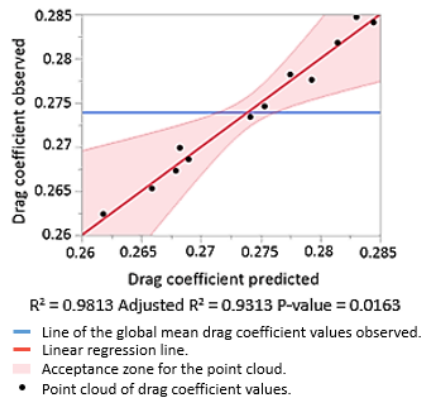


Figure 5. Graphical representation of the observed values versus the predicted response ones (Y).

6.3. Analysis of variance (ANOVA)

The appropriateness of the chosen model has been assessed by ANOVA analysis. This test was used to analyze the variance of the model established with respect to the variance of the residue, using the Fisher Snedecor test. The result was taken to be significant if ($F_{exp} \gg F_{\alpha, v \text{ model}, v \text{ residue}}$), where $v \text{ model} = 8$, $v \text{ residue} = 3$ and $\alpha = 0.05$. The results of the analysis of variance carried out show that the experimental value $F_{exp} = 19.6850$, which is the ratio between the mean square of the model and the mean square of the error, is much higher than the critical value $F_{(theo.)} = F_{(0.05 (8) (3))} = 8.85$ of the distribution F at a confidence interval of 5% at 8 and 3 degrees of freedom. In addition, the probability $\text{Prob.} > F_p = 0.0163$ was significantly inferior to 0.05. Consequently, the model for the coefficient of drag is validated.

6.4. Equation of the model according to the most influential factors

From the statistical analysis, it was observed that the aerodynamic drag of the model was significantly influenced by the type of curvature (F), the inlet velocity (H) and the length ratio (A). However, the impact of the other parameters were not significant, because, their p-value were higher than 0.05. The best model, which gives the determining factors that have a significant influence in the calculation of the drag coefficient of the Ahmed body with deflector installed on the rear window, is written as the Eqn. 12.

$$Y = 0.2740 - 0.0062F - 0.0027H - 0.0018A \quad (12)$$

6.5. Optimal deflector

A model of Ahmed with a deflector was designed on SolidWorks by using the optimal factors obtained from JMP Pro 14 software (Figure 6). The numerical study was conducted on the ANSYS Fluent software. After about 550

iterations, the convergence of the residuals of the simulation was observed. Table 7 presents a comparison between the value of the drag coefficient obtained by the JMP Pro 14 software, according to the Plackett-Burman screening plan ($C_D = 0.261951$), and the value obtained by the numerical study on the CFD Fluent software ($C_D = 0.265789$). It is observed that the value obtained by the screening plan is slightly inferior to that obtained by the numerical simulation, with a relative deviation estimated at 1.465%. The value obtained by the simulation allows a drag reduction of up to 5.75% compared to the Ahmed's body without deflector.

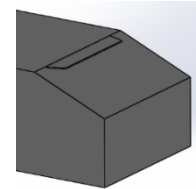


Figure 6. Deflector installed on the Ahmed model according to the optimal factors obtained by JMP Pro 14.

Table 7. Optimal values of the factors and the obtained drag coefficient

ID	Optimal Values	Drag Coefficient obtained		Relative Gap [%]
		Plackett-Burman Plan	Simulation	
A	6%			
B	100%			
C	0.003 m			
D	0°	0.261951	0.265789	1.465
E	4.5°			
F	Concave			
G	0.275m			
H	40 m.s ⁻¹			

Figure 7 below represents a comparison of the turbulent kinetic energy (TKE) in the plane of symmetry of Ahmed's model for two cases (without and with a deflector obtained from the optimal factors). The maximum TKE values were observed to be in the closest wake zone to the base of the model. For the first case (Model without deflector), there is a high concentration of TKE in the wake zone of the model near the ground between $X = 0.1$ m and $X = 0.2$ m. In this case, the size of the main vortices has been increased. On the contrary, in the second case (Ahmed's model with deflector obtained from the optimal factors), the wake zone is lengthened and the vortices dissipated. The maximum TKE was weakened and moved away from the model to be at position $X = 0.25$ m. It is found that the use of this type of deflector delays separation and disturbs vortices, which minimizes the depression created in the wake zone behind the vehicle, and then it decreases its aerodynamic drag.

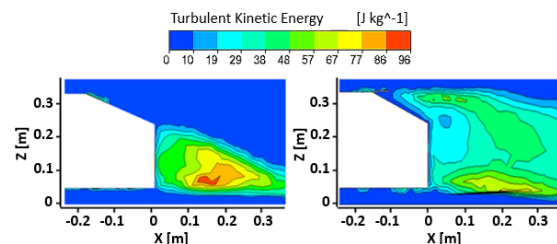


Figure 7. Comparison of the turbulent kinetic energy for the Ahmed model without deflector (left), and the model with optimal deflector (right).

7. Conclusion

The evaluation of the effect of many factors related to the deflector installed on the rear base of the Ahmed model was carried out via the screening concept. To determine the deflector factors that influence aerodynamic drag of cars, the Plackett-Burman plan was first used. Eight factors were analyzed and identified on two levels, namely: length ratio (3 % - 6 %), width ratio (50 % - 100 %), thickness (0.001 m - 0.003 m), ends angle (0 ° - 45 °), angle of inclination (-5 ° - 5 °), type of deflector (Convex, Concave), radius of curvature (0.05 m - 0.5 m) and inlet velocity (20 m.s⁻¹ - 40 m.s⁻¹). Twelve study models were performed by the SolidWorks software.

Besides, the numerical simulation was performed on the CFD software ANSYS. The impact of these factors was studied on a response (Y) which represents the coefficient of aerodynamic drag. The JMP Pro 14 software gives three significant factors: the type of deflector, the inlet velocity and the length ratio. The drag coefficient obtained from the optimal values was compared to that of simulation and thus a relative deviation of 1.46 % was observed. There was a reduction of about 5.75 % in the drag observed on Ahmed's model with optimal deflector, compared to the non-deflector model. In addition, installing the optimal deflector on the body of Ahmed widens the wake area and eliminates chain stay vortex.

Author Contributions

Conceptualization, M.M. and M.O.; methodology, B.N.; software, M.M.; validation, M.O., O.B.; formal analysis, M.M.; investigation, M.M.; resources, B.N.; data curation, M.M.; writing—original draft preparation, M.M.; writing, review and editing, M.M.; visualization, M.O.; supervision, O.B.; project administration, M.O. All authors have read and agreed to the published version of the manuscript.

Funding

This research received no external funding.

Declaration of Competing Interest

The authors declare that they have no known competing financial interests or personal relationships that could have appeared to influence the work reported in this paper.

References

- [1] F. Szodrai, "Quantitative Analysis of Drag Reduction Methods for Blunt Shaped Automobiles", *Applied Sciences*, vol. 10, n° 12, 2020, p. 4313.
- [2] M. Maine, M. E. Oumami, O. Bouksour, A. Tizliouine, "Review of research on cars wake flow control methods to reduce aerodynamic drag", *International journal of innovation and applied studies*, 2019, 25:1069-1089.
- [3] B. Wang, Z. Yang, H. Zhu, "Active flow control on the 25° Ahmed body using a new unsteady jet", *International Journal of Heat and Fluid Flow*, vol. 79, 2019, p. 108459.
- [4] T. Heinemann, M. Springer, H. Lienhart, S. Kniesburges, C. Othmer, S. Becker, "Active flow control on a 1:4 car model", *Experiments in Fluids*, vol. 55, n° 5, 2014.
- [5] A. A. Moussa, R. Yadav, J. Fischer, "Aerodynamic Drag Reduction for A Generic Sport Utility Vehicle Using Rear Suction", vol. 4, n° 8, 2014, p. 7.
- [6] M. Metka, J. W. Gregory, "Drag reduction on the 25-deg Ahmed model using fluidic oscillators", *Journal of Fluids Engineering*, vol. 137, n° 5, 2015, p. 051108.
- [7] Shimizu K, Nakashima T, Sekimoto S, Fujii K, Hiraoka T, Nakamura Y, Nouzawa T, Ikeda J, Tsubokura M., "Aerodynamic drag reduction of a simplified vehicle model by promoting flow separation using plasma actuator", *Mech. Eng. Lett.*, (5):1-9, 2019.
- [8] A. Hossain, P. R. Arora, A. Rahman, A. A. Jaafar, "Analysis of Longitudinal Aerodynamic Characteristics of an Aircraft Model with and Without Winglet", *Jordan Journal of Mechanical and Industrial Engineering*, vol. 2, n° 3, 2008, p. 143-150.
- [9] A. Hossain, A. Rahman, J. Hossen, P. Iqbal, N. Shaari, et G. K. Sivaraj, "Drag reduction in a wing model using a bird feather like winglet", *Jordan Journal of Mechanical and Industrial Engineering*, vol. 5, n° 3, 2011, p. 267-272.
- [10] G. Fourrié, L. Keirsbulck, L. Labraga, P. Gilliéron, "Bluff-body drag reduction using a deflector", *Experiments in Fluids*, vol. 50, n° 2, 2011, p. 385-395.
- [11] R. B. Sharma, R. Bansal, "CFD simulation for flow over passenger car using tail plates for aerodynamic drag reduction", *IOSR Journal of Mechanical and Civil Engineering (IOSR-JMCE)*, vol. 7, n° 5, 2013, p. 28-35.
- [12] E. Wahba, H. Al-Marzooqi, M. Shaath, M. Shahin, T. El-Dhmarshawy, "Aerodynamic drag reduction for ground vehicles using lateral guide vanes", *CFD Letters*, vol. 4, n° 2, 2012, p. 68-79.
- [13] S. Bayraktar, Y. O. Bilgili, "Effects of under body diffuser on the aerodynamics of a generic car", *International Journal of Automotive Engineering and Technologies*, vol. 7, n° 2, 2018, p. 99-109.
- [14] A. Dubey, S. Chheniya, A. Jadhav, "Effect of Vortex generators on Aerodynamics of a Car: CFD Analysis", *Inter. Journal of Innovations in Engineering and Technology*, vol. 2, n° 1, 2013, p.137-144.
- [15] G. Pujals, S. Depardon, C. Cossu, "Drag reduction of a 3D bluff body using coherent streamwise streaks", *Experiments in fluids*, vol. 49, n° 5, 2010, p. 1085-1094.
- [16] Y. Wang, C. Wu, G. Tan, Y. Deng, "Reduction in the aerodynamic drag around a generic vehicle by using a non-smooth surface", *Proceedings of the Institution of Mechanical Engineers, Part D: Journal of Automobile Engineering*, vol. 231, n° 1, 2017, p. 130-144.
- [17] T. Hirst, C. Li, Y. Yang, E. Brands, G. Zha, "Bluff body drag reduction using passive flow control of Jet Boat Tail", *SAE International Journal of Commercial Vehicles*, vol. 8, n° 2, 2015, p. 713-721.
- [18] B. Mohammadikalakoo, P. Schito, M. Mani, "Passive flow control on Ahmed body by rear linking tunnels", *Journal of Wind Engineering and Industrial Aerodynamics*, vol. 205, 2020, p. 104330.
- [19] F. Delassaux, I. Mortazavi, E. Itam, V. Herbert, C. Ribes, "Sensitivity analysis of hybrid methods for the flow around the Ahmed body with application to passive control with rounded edges", *Computers & Fluids*, vol. 214, 2021, p. 104757.
- [20] B. Khalighi, K.-H. Chen, G. Iaccarino, "Unsteady aerodynamic flow investigation around a simplified square-back road vehicle with drag reduction devices", *Journal of fluids engineering*, vol. 134, n° 6, 2012, p. 061101.
- [21] M. Varney, M. Passmore, A. Gaylard, "The Effect of Passive Base Ventilation on the Aerodynamic Drag of a Generic SUV Vehicle", *SAE Int. J. Passeng. Cars - Mech. Syst.*, vol. 10, n° 1, 2017, p. 345-357.
- [22] R. Tarakka, N. Salam, J. Jalaluddin, M. Ihsan, "Effect of blowing flow control and front geometry towards the reduction of aerodynamic drag on vehicle models", *FME Transactions*, vol. 47, n° 3, 2019, p. 552-559.
- [23] A. R. Paul, A. Jain, F. Alam, "Drag reduction of a passenger car using flow control techniques", *International Journal of Automotive Technology*, vol. 20, n° 2, 2019, p. 397-410.

- [24] W. Hanfeng, Z. Yu, Z. Chao, H. Xuhui, "Aerodynamic drag reduction of an Ahmed body based on deflectors", *Journal of Wind Engineering and Industrial Aerodynamics*, vol. 148, 2016, p. 34-44.
- [25] S. Krajnović, "Optimization of aerodynamic properties of high-speed trains with CFD and response surface models", in *The Aerodynamics of Heavy Vehicles II: Trucks, Buses, and Trains*, vol. 41, 2009, p. 197-211.
- [26] W. Zheng, W. Hu, J. Hai-jun, S. Ya-feng, "Study on Response Surface Methodology with Artificial Neural Networks Application in Aerodynamic Optimization", in *2009 WRI World Congress on Computer Science and Information Engineering*, Los Angeles, California USA, 2009, p. 620-626. doi: 10.1109/CSIE.2009.458.
- [27] S. Beigmoradi, H. Hajabdollahi, A. Ramezani, "Multi-objective aero acoustic optimization of rear end in a simplified car model by using hybrid Robust Parameter Design, Artificial Neural Networks and Genetic Algorithm methods", *Computers & Fluids*, vol. 90, 2014, p. 123-132.
- [28] S. R. Ahmed, G. Ramm, G. Faltin, "Some Salient Features Of The Time-Averaged Ground Vehicle Wake", in *SAE International Congress and Exposition*, 1984.
- [29] A. Raina, G. A. Harmain, M. I. U. Haq, "Numerical investigation of flow around a 3D bluff body using deflector plate", *International Journal of Mechanical Sciences*, vol. 131-132, 2017, p. 701-711.
- [30] A. Raina, A. Khajuria, « Flow control around a 3D-bluff body using passive device, *EPH-International Journal of Science and Engineering (ISSN: 2454-2016)*, vol. 4, n° 1, 2018, p. 08-13.
- [31] A. L. J. Pang, M. Skote, S. Y. Lim, "Modelling high Re flow around a 2D cylindrical bluff body using the $k-\omega$ (SST) turbulence model", *Progress in Computational Fluid Dynamics*, An International Journal, vol. 16, n° 1, 2016, p. 48-57.
- [32] F. R. Menter, "Two-equation eddy-viscosity turbulence models for engineering applications", *AIAA Journal*, vol. 32, n° 8, 1994, p. 1598-1605.
- [33] R. Manceau, J. P. Bonnet, M. Leschziner, F. Menter, "10th joint ERCOFTAC (SIG-15)/IAHR/QNET-CFD workshop on refined flow modelling", *Universite de Poitiers*, 2002.
- [34] C. A. R. Duarte, L. E. R. Duarte, B. S. de Lima, F. J. de Souza, "Performance of an optimized $k-\epsilon$ turbulence model for flows around bluff bodies", *Mechanics Research Com.*, vol. 105, 2020, p. 103518.
- [35] B. Thomas, R. K. Agarwal, "Evaluation of various RANS turbulence models for predicting the drag on an Ahmed body", in *AIAA Aviation 2019 Forum*, Dallas, Texas, juin 2019.
- [36] E. Guilmineau, G. B. Deng, A. Leroyer, P. Queutey, M. Visonneau, J. Wackers, "Assessment of hybrid RANS-LES formulations for flow simulation around the Ahmed body", *Computers & Fluids*, vol. 176, 2018, p. 302-319.
- [37] W. Meile, G. Brenn, A. Reppenhagen, B. Lechner, A. Fuchs, "Experiments and numerical simulations on the aerodynamics of the Ahmed body", vol. 3, p. 32-39, 2011.
- [38] R. L. Plackett, J. P. Burman, "The design of optimum multifactorial experiments", *Biometrika*, vol. 33, n° 4, 1946, p. 305-325.

Performance and Emission Characteristics of Waste Frying Oil Biodiesel Stored Under Optimized Condition

J. Pavalavana Pandian^{*a}, M. Pugazhivadivu^b, B. Prabu^b, K. Velmurugan^c,
V.S.K. Venkatachalapathy^c

^a Associate Professor, Department of Mechanical Engineering, Sri Manakula Vinayagar Engineering College, Madagadipet, Puducherry-605 107, India.

^b Professor, Department of Mechanical Engineering, Pondicherry Engineering College, Puducherry-605 014, India

^c Professor, Department of Mechanical Engineering, Sri Manakula Vinayagar Engineering College, Madagadipet, Puducherry- 605 107, India..

Received May 19 2020

Accepted June 24 2021

Abstract

Diesel engines are the most ideal prime-movers for automobiles, railways, and marine transport to generate power. A hasty switch to alternative fuels is crucial to meet the diesel fuel demand as well as to safeguard the environment from the pollution caused by the diesel fuel combustion. In recent periods, biodiesel becomes an established possible substitute fuel for Compression Ignition (CI) engines as it offers numerous important advantages like bio-degradability and renewability. It also produces comparable engine performance and relatively lowers toxic emissions. A single cylinder, 4.4 kW rated power CI engine was operated with biodiesel with Pyrogallol (PY) stored at optimized storage conditions (B100 (PY)), biodiesel stored at 4.5 months at ambient condition (B100) and diesel fuel. The engine performance results indicate that the brake specific fuel consumption by B100 (PY) was lower with 9.62% than that of B100 and 15.09% higher than the base line diesel fuel. The thermal efficiency of the engine fuelled with B100 (PY) was comparable with diesel. The engine thermal efficiency with diesel and B100 (PY) is 31.79% and 29.53% respectively. Further, there was no significant changes in combustion characteristics, viz. heat release rate and gas pressure available in cylinder between B100 (PY) and diesel fuel. The Nitrogen Oxides (NO_x) with B100 (PY) was 15.04% higher than diesel. This is because of 10 - 11% oxygen substance present in biodiesel. However, the NO_x concentration by B100 (PY) was 8.43% lower than B100. Similarly, the smoke density with B100 (PY) was 9.83% and 25.72% lower than B100 and diesel fuel respectively. The engine performance results thus showed that waste frying oil (WFO) biodiesel has to be stored under optimum conditions to obtain equivalent engine performance and lower emissions.

© 2021 Jordan Journal of Mechanical and Industrial Engineering. All rights reserved

Keywords: Biodiesel, waste frying oil, antioxidant, pyrogallol, storage stability, diesel engine;

1. Introduction

The declining of world fossil fuel supply needs a source of replacement. The resources of an alternative fuel resource will play a critical role to uproot the scarcity. The demand for fossil fuel raises due to the increasing transportation, mechanization and industrialization. Thus, limited sources and environmental pressure have necessitated the seek for alternative fuels [1], which partially solves the problems of environmental degradation, economy stability, energy security, constraints on fuel import and agricultural economy. Generally, diesel engines were operated by using fossil fuels blended with different biodiesel and their blends, which are approved as a power source with high efficiency of energy generation in the field of automobile. Biodiesel is a renewable fuel that is obtained from vegetable oils, such as sunflower, sesame, groundnut, cotton seed, soybean, canola, waste cooking oils, or animal fats. These

oils and fats undergo a chemical reaction with an alcohol, such as ethanol or methanol in the presence of a catalyst to form fatty acid methyl ester called as biodiesel. Biodiesel contains no aromatics, and has higher cetane number than diesel fuel, and with trifling oxygen and sulphur content [2]. Among these, biodiesel from waste cooking oil is considered as an important source. Waste frying oil (WFO) has dual benefits (i) waste oil disposal strategy for government saves environmental pollution, and (ii) lowering of gas emission, which in turn guards human health. The biodiesel can be utilised as a potential alternative fuel in conventional CI engines without any alteration in engine parts [3, 4]. In addition, biodiesel cost is twice the rate of conventional diesel due to the high cost of biodiesel feedstock [5]. The cost of biodiesel fuel can be trimmed down by using the waste animal fats, waste frying oils, for the biodiesel production[6].

Zhang et al. and Supple et al. has stated that the use of WFO as a replacement for raw vegetable oil to produce

* Corresponding author e-mail: jvpandian@yahoo.in.

biodiesel is a recommended approach to crash down the feedstock cost [7, 8]. Therefore, a search on cheaper feedstocks (inedible or waste feedstocks) for biodiesel production by the researchers is carried out to cut down the production costs. Low priced feedstocks as biodiesel source have been scrutinized, and few of them are described below. Lin and Li evaluated the engine performance and emissions with waste cooking oil and marine fish-oil biodiesel as the fuel. As a result they observed that the commercial biodiesel obtained from WFO, fish-oil biodiesel has higher NO_x emissions and black smoke opacity and a lower Carbon monoxide (CO) and Carbon dioxide emission (CO_2) and brake-specific fuel consumption rate (BSFC) [9]. The methyl ester produced from WFO used in a direct injection diesel engine was assessed by Utlu et al. They observed that the levels of emission, such as CO, CO_2 , NO_x , and smoke darkness of WFO biodiesel are less than the conventional diesel fuel [10].

Biodiesel has higher boiling point, high specific gravity and higher cetane number than diesel fuel and contains 10% oxygen. It is a low smoke emissions fuel and environmentally friendly. The ignition delay gets shorten due to its higher cetane number, which results in reduction of NO_x emissions in the initial phase of combustion process. Exhaust gas emissions such as CO, Hydro Carbons (HC), Particulate matters (PM), Sulphur Oxides (SO_x), polycyclic aromatic hydrocarbons, and smoke are also exhausted lower with biodiesel than with diesel [11-15]. On combustion biodiesel provides considerable reductions in CO emissions [16], PM emissions [17], and total HC emissions when compared to the conventional fossil fuels [18-20].

Agarwal and Das reported that better performance in terms of brake-specific energy consumption, thermal efficiency, exhaust emissions, components wear and smoke opacity was observed in the engine fuelled by biodiesel than that of diesel engines during the complete combustion [21]. Similar results were observed by many researchers with different biodiesel and its blends from various sources [22-25].

Gopal et al. have identified a remarkable reduction in smoke emission, CO and unburned HC, but NO_x seems to be slightly higher for biodiesel and its blends compared to diesel fuel [26]. Numerous studies on CI performance using WFO derived biodiesel are available in the literature. Biodiesel was obtained from waste palm oil [27, 28], waste peanut oil [29], waste coconut oil [30] etc., Many researches have been carried on the use of substitute input products like soybean and rapeseed waste oil in the production of biodiesel for use in CI engines [22, 31-37]. Engine performance parameters, such as ignition delay, thermal efficiency, specific fuel consumption (SFC), cylinder pressure, heat release rate, exhaust gas temperature (EGT), concentration of NO_x , HC and smoke were analyzed while running the CI engine using waste frying oil biodiesel [38-44].

Cetinkaya and Karaosmanoglu made a performance in an engine operating on waste frying oil biodiesel and showed that the smoke reduction was around 60% for B100 (100% biodiesel) when compared to conventional diesel fuel [23]. A 34 kW, direct injection, four stroke, three cylinder engine fuelled with biodiesel from waste fried olive oil shows the result with a reduction of CO (58%), CO_2 (8.6%), and SO_x emissions (57.7%). Any have, an increase

in SFC with 8.5% and 32% of NO_x emissions, were observed respectively [45].

The performance and emissions of an engine with soybean biodiesel by toting up by various antioxidants, such as Butylated hydroxyanisole (BHA) and tert-Butylhydroquinone (TBHQ) and found effectively on governing the NO_x discharge for soybean biodiesel, but the other additives have no effect on dropping the NO_x release [46]. Ryu, observed the efficacy of five different additives, such as Propyl Gallate (PG), Butylated hydroxytoluene (BHT), BHA, TBHQ, and α -tocopherol respectively. The BSFC of biodiesel fuel with additives was found to be shrunken compared to biodiesel fuel without antioxidant additive [47].

Ileri and Koçar, have determined that the 2-Ethyl Hexyl Nitrate (EHN) could be a potential additive for dropping NO_x emission at the increasing rate of the CO emission. EHN followed by BHA and BHT was found to be a best NO_x reducer [48]. Rizwanul et al. performed an experiment with BHA and BHT antioxidant at 1000 ppm concentration to palm biodiesel and observed the engine performance and emission characteristics [49]. Roy et al. reported that HC and CO emissions reduction were possible with the increase of blending ratio between biodiesel and diesel [50]. Balaji et al., reported that SFC and Brake thermal efficiency (BTE) are approximately similar with increase in ratio of PY as an additive for Neem oil biodiesel. And also found that HC emission lowered by 31% at full load compared with diesel, and a rise in CO_2 , CO and smoke emissions were noticed [51]. Varatharajan et al. examined diesel engine fuelled with soybean biodiesel added with P-Phenylenediamine (PPD) derived aromatic amine antioxidants and noted that a remarkable reduction in NO_x level [52].

No significant variation was found in BSFC and BTE for Neem oil biodiesel with A-tocopherol acetate as an additive and also HC, CO and smoke emissions were increased with antioxidant concentration [53]. Sharma and Murugan, studied the effect of long term storage by its IP of biodiesel with and without antioxidant and made a performance study on CI engine. In this study Jatropha biodiesel with waste tyre pyrolytic oil and its blends were added with four different antioxidants like TBHQ, PG and PY. The results showed that the totalling of antioxidant to the biodiesel make better the fuel performance. A decrease in BSFC was found to be with the fuel containing 20% blend and PY with a highest reduction on NO_x and HC emission. As a result it was concluded that biodiesel with PY shows good response towards long term storage while performance on diesel engine [54].

Palash et al. evaluated the engine performance and smoke emission of biodiesel blends obtained from Jatropha oil with and without the addition of antioxidant N,N'-diphenyl-p-phenylenediamine (DPPD). By adding the additive of 0.15% (m) DPPD in various proportions of blends, the reduction in NO_x emissions were observed under the full throttle condition compared to biodiesel blends without the additive [55]. Hess et al reported that the biodiesel with BHA / BHT shows a drastic reduction of NO_x emissions in diesel engines. As a summary, the antioxidants serve an additional purpose as well [46]. It is observed that the biodiesel oxidize more swiftly than petrodiesel and storage stability is a concern. To improve its storage stability, biodiesel blends are likely to be added with

antioxidants. Addition of additives makes a potential impact on the emission of biodiesel combustion[56].

In this study, the performance of a single cylinder, four stroke, 4.4 kW rated CI engine with 100% WFO biodiesel, WFO biodiesel stored at an optimum condition with pyrogallol as an additives and with diesel were carried out. The engine's operational factors, such as BSFC, BTE, brake power, heat release rate, total fuel consumption, cylinder gas pressure, and emissions were compared for three fuels namely 100% biodiesel, biodiesel with additive and diesel.

2. Materials and methods

2.1. Test fuel

Biodiesel obtained from waste frying oil collected from Indian fast food in which various food items, such as fish, chicken, beef were fried. The conversion of WFO to biodiesel was carried out by standard transesterification process. The engine testing and performance were carried out with the following three sources (i) 100% biodiesel maintained at optimum storage condition (B100 (PY)) i.e. stored at 45°C for 4 months with 435 ppm of pyrogallol as an antioxidant, the optimum condition of biodiesel was obtained by experimenting the biodiesel by treating with various composition of storage condition under response surface methodology (Box Behnken method), (ii) 100% biodiesel stored at atmospheric conditions for 4 months without the addition of antioxidant (B100) and (iii) Diesel. Table 1 shows the specification of test fuels. The fuel stored under optimum condition temperature is maintained in a electrical food warmer (Make: FW 554). The chemicals for the preparation of biodiesel, such as methanol, NaOH and antioxidant pyrogallol (Supplier:Merck) were procured from local chemical dealer. The engine operating performance and smoke emission tests were conducted at standard engine testing laboratory at Chennai, India.

2.2. Experimental setup

The engine experiments were conducted in an IC engine laboratory. A single cylinder, 4 strokes, air cooled, direct

injection CI engine was used. The engine specification is given in Table 2. An electrical dynamometer coupled with the engine with a rheostat with loading arrangement to supply the load and the setup is shown in Figure 1. The engine test laboratory equipped with a complete measuring facilities relating to diesel engine performance parameters and analysis of exhaust gas emissions. The engine was equipped with pressure sensor (make: Kistler, model: 6961A250), crank angle encoder (make: Kistler) and data acquisition system. Two separate tanks were used for biodiesel and diesel fuels. The consumption of fuel was measured by accounting the time taken for a preset quantity of fuel to flow into the engine. An exhaust gas analyser (make: AVL. 444, model: DI GAS) to quantify the CO, HC, and NOx concentrations in the exhaust gas. The smoke density was recorded using a Smoke meter (make: AVL, model: 415).

Table 1. Test fuel Specifications

Properties	B100	B100 (PY)	Diesel
Density at 15°C, (g/m ³)	0.857	0.871	0.860
Kinematic viscosity at 40°C, (cSt)	3.671	3.691	4.24
Flash point, °C	203	211	52
Heating value, (MJ/kg)	39.85	40.14	43.35
Cetane number	56.61	57.4	49
Iodine value (gI ₂ /100 g of oil)	71.33	73.42	80-135
Acid value (mg KOH/g of oil)	0.204	0.213	-

Table 2. Engine specifications

Make	Kirloskar
Rated power	4.4 kW
Bore diameter	87.5 mm
Compression ratio	17.5:1
Dynamometer	Electrical
Number of cylinder	One
Rated speed	1500 rpm
Stroke	110 mm
Cranking	Hand Cracking
Injection timing	23° bTDC

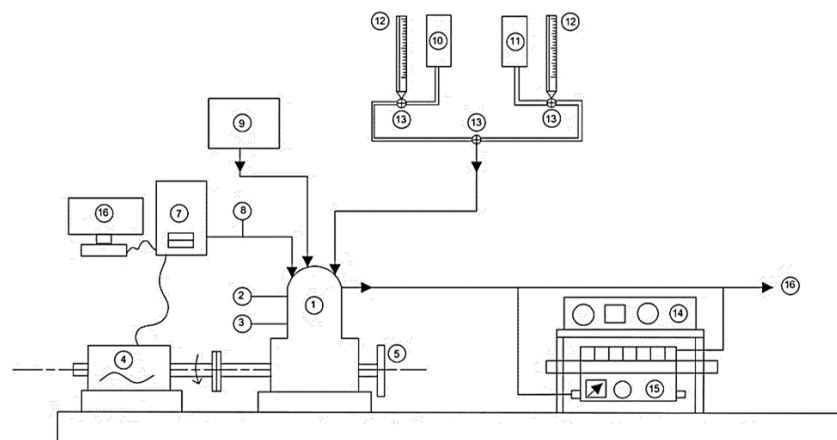


Figure 1. Schematic layout of experimental system

- | | | |
|------------------------------|----------------------------|-------------------------------|
| 1. Engine, | 2. Electrical dynamometer, | 3. Electrical load bank, |
| 4. Diesel fuel tank, | 5. Biodiesel fuel tank, | 6. Burette, |
| 7. Two way control valve, | 8. Pressure sensor, | 9. Personnel computer, |
| 10. Data acquisition system, | 11. Crank angle encoder, | 12. Exhaust gas thermocouple, |
| 13. Di gas analyzer, | 14. Smoke meter (FSN), | 15. Exhaust gas to air. |

2.3. Test methods

The engine was operated for a start-up period till the circulation water and oil attains a firm temperatures. The engine takes half an hour to attain its stable running condition. After warming up, the test procedures were set and the engine was permitted to attain a steady state prior to note of data. Regulatory test procedures were followed to verify and ensure conformity with the mandatory standards to measure the emissions.

The engine was started with required fuel and made to run for 15 – 20 mins. The engine was operated at various load conditions of 0, 25, 50, 75 and 100% of full load and at 1500 rpm. At each loading condition, the constant engine speed was maintained at 1500 rpm and the heat release data, crank angle vs. cylinder gas pressure, fuel consumption (time taken for 10 cc), exhaust gas temperature and gas emissions were taken. The parameters such as BSFC, TFC, BTE and brake power output were calculated based on the data collected. Emissions from exhaust gas were generally measured for every loading condition on a volumetric basis. The exhaust emissions measurements were calculated as a weighted average.

3. Results and discussion

The performance of a single-cylinder diesel engine was studied with the fuels listed below: (i) B100 (PY) - 100% waste frying oil biodiesel stored under optimum storage condition (waste frying oil biodiesel treated with 435 ppm PY and stored at 45°C for a period of 4 months), (ii) B100 – 100% waste frying oil biodiesel stored for 4.5 months at ambient condition without the addition of antioxidant, (iii) Base line diesel fuel.

The engine performance result with the three fuels is described in terms of brake specific fuel consumption, thermal efficiency, exhaust gas temperature, heat release data, cylinder pressure data, smoke, NO_x, and unburnt hydrocarbon in the exhaust gas.

3.1. Brake specific fuel consumption

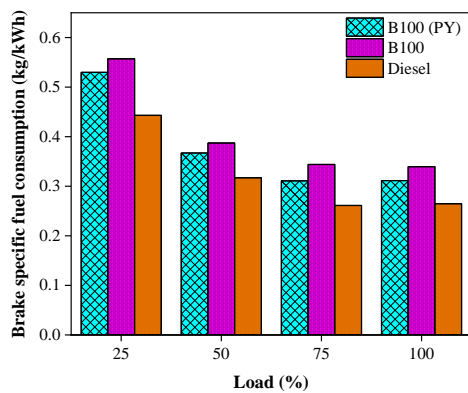


Figure 2. Brake specific fuel consumption vs load.

The engine's brake-specific fuel consumption (bsfc) at different loads while using B100 (PY), B100 and diesel fuel were shown in Fig 2. It is perceived that, for all the three test

fuels, the bsfc decreased up to 75% of its full load condition. And further, the bsfc was minimum with all three fuels at 75% full load and it was 0.312, 0.343 and 0.260 kg/kWh for B100 (PY), B100 and diesel respectively. Compared to diesel fuel operation, the bsfc was 15.08% and 24.04% higher respectively with B100 (PY) and B100 fuel operation. This may be due to the poor energy content of biodiesel.

Compared to B100, the bsfc with B100 (PY) was 9.62% and 9.06% lower at 75% and 100% full load respectively. As B100 (PY) was stored under optimum storage conditions, it would have undergone reduced oxidative degradation and its quality would have been maintained. Identical results were obtained by using B100 and B100 treated with antioxidants as fuels [47, 48, 51, 57-59]. At 100% full load, there was marginal increase in bsfc for all fuels because at this load, relatively more fuel would have been injected to produce the rated power output and the engine would have operated with an air fuel ratio closer to stoichiometric.

3.2. Brake thermal efficiency:

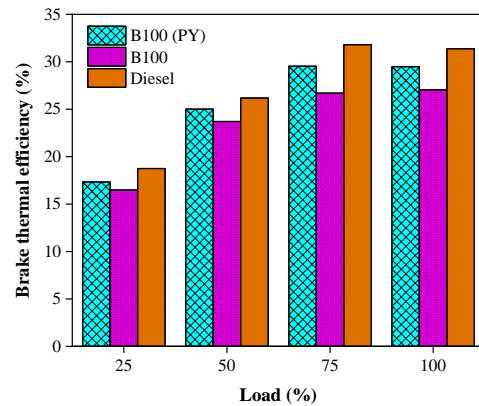


Figure 3. Brake thermal efficiency vs load.

The dissimilarity of thermal efficiency pertaining to engine load for the three fuels B100 (PY), B100 and diesel is given in Fig 3. For all the tested fuels, the thermal efficiency was seen to upsurge with load up to 75% load. And also it is seen that maximum BTE was obtained at 75% of full load. At 75% load, the thermal efficiency with diesel, B100 (PY) and B100 were found to be 31.79%, 29.53% and 26.69% respectively. However, with B100 (PY), the engine thermal efficiency is nearer to the diesel fuel operation.

The BTE with B100 (PY) and B100 were lower compared to conventional diesel fuel due to their low energy content. At full load, more fuel is injected and the engine runs with very little excess air and there is possibility for incomplete combustion of fuel which leads to a drop in thermal efficiency. The optimum storage condition of B100 with the presence of antioxidant in biodiesel reduces oxidation and promotes more complete combustion thereby improves the brake thermal efficiency. Venkatasubbaiah showed similar kind of result with rice bran oil biodiesel treated with N,N'-diphenyl-p-phenylenediamine antioxidant [60]. Kivevele et al., also showed this kind of trend while using *croton megalocarpus* biodiesel treated with pyrogallol [59]. Balaji and Cheralathan reported similar trend in thermal efficiency for Neem oil

biodiesel treated with L-ascorbic acid as antioxidant [61]. Varatharajan et al., obtained similar result for jatropha biodiesel added with antioxidant like BHT and α -tocopherol [62].

3.3. Exhaust gas temperature

Fig. 4. Shows the disparity of exhaust gas temperature at varied loads. It is found that the exhaust gas temperature increases with rise in increase in load, which may be because of the power output increase with respect to load. Due to this increased output, more fuel would have been injected, resulting in greater heat release rate and increase in EGT at high loads. All the tested fuels show a similar trend. At 75% full load, the maximum EGT attained while operating the engine with B100 (PY) was 252°C which is 5.55% higher than diesel and 6.34% lower than B100. Similar trend was documented by Balaji and Cheralathan, Kivevele et al., Zafer Aydin and Aykut Safa , and Ajay V. Kolhe et al., [58, 59, 70, 71]

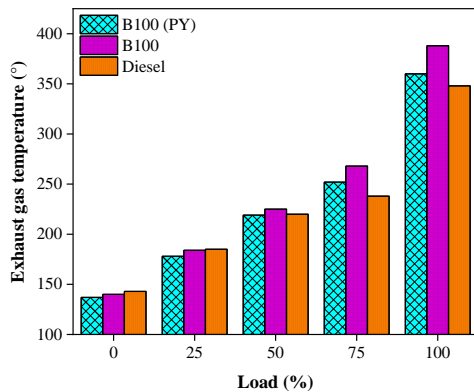


Figure 4. Exhaust gas temperature vs. Load

3.4. Cylinder gas pressure:

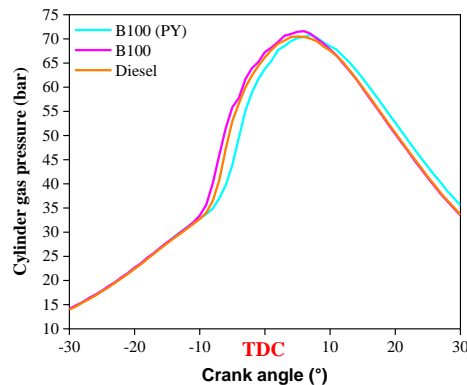


Figure 5. Cylinder gas pressure vs crank angle.

Fig.5.Shows the profiles of cylinder gas pressure with B100 (PY), B100 and diesel fuels at 75% load condition. There is no significant difference in cylinder gas pressure profiles among the biodiesel fuels and diesel fuel. The presence of

oxygen in biodiesel would have helped for the better combustion of biodiesel fuels [63-65]. The maximum pressure was found to be 71.822 bar, 70.826 bar and 70.494 bar respectively, for B100, B100 (PY) and diesel respectively.

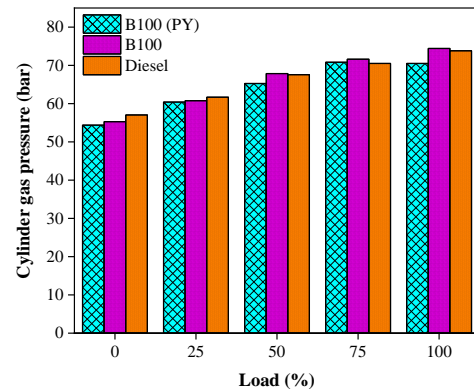


Figure 6. Cylinder gas pressure vs load.

Fig.6.Shows the maximum gas pressure in the cylinder at different engine loads. It is observed that the gas pressure in the cylinder increases with the respective engine load, which is due to more fuel injection at higher loads to produce more power output.

3.5. Heat release rate:

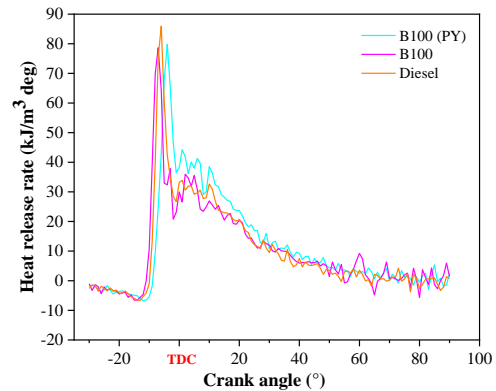


Figure 7. Heat release rate vs crank angle.

Fig 7. shows the variation of HRR with B100 (PY), B100 and diesel at 75% full load. Different stages of combustion like ignition delay period, rapid combustion, controlled combustion and after burning could be seen in the HRR diagram. It is found that the maximum HRR for B100 (PY), B100 and diesel are 79.79, 78.65 and 85.97 kJ/m³ deg respectively. The slight decrease in maximum heat release rate with biodiesel fuels may be owing to their lower content of energy and higher viscosity. Furthermore, no significant difference in maximum HRR between B100 and B100 (PY) is observed.

The data from HRRC graph was utilized to find the combustion factors such as start of fuel injection (SoI), start of combustion (SoC), ignition delay (ID) and maximum HRR.

The ignition delay was calculated by taking the difference in crank angle among SoI and SoC. Table 3. shows these parameters for diesel, B100 (PY), and B100 at 75% full load. In this work, start of injection was 23° bTDC as recommended by the supplier. Further, it is noticed that, the delay in ignition for B100 was the lowest followed by diesel and B100 (PY). The ignition delay slightly decreases with the use of B100 compared to diesel.

Table 3. Combustion parameters at 75% load

Fuel	SoI (° bTDC)	SoC (° bTDC)	ID (°CA)	Maximum gas pressure in cylinder (bar)	Maximum HRR (kg/m ³ deg)
B100 (PY)	23	8	15	70.824	79.772
B100	23	10	13	71.600	78.660
Diesel	23	9	14	70.496	85.981

Similar results were documented by Ryu et al., with soybean oil biodiesel mixed with antioxidants [47]. Sharma and Murugan, also pointed out similar trend for the diesel engine operated with Jatropha biodiesel treated with antioxidants [54].

3.6. NO_x concentration:

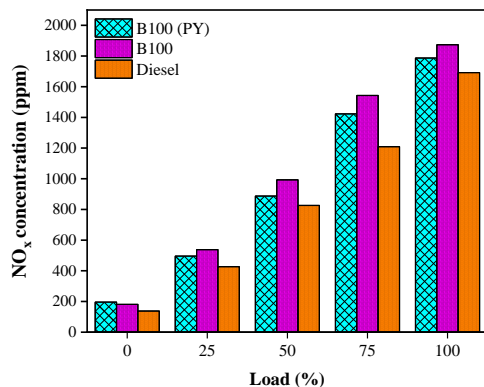


Figure 8. NO_x concentration vs load.

The variation of NO_x concentration with increase in load for B100 (PY), B100 and diesel is shown in Fig 8. It is well known that the major factors that affect the formation of NO_x are temperature and availability of oxygen [66]. It is seen that at all low loads (No load and 25% full load) the NO_x concentration is very less. This might be due to the lower combustion gas temperature. It is seen that the increase in exhaust gas with increase in engine loads for all the fuels tested. This could be due to the higher quantity of fuel undergoing combustion at higher loads to produce more power output which in-turn release a high combustion gas temperature.

The higher NO_x concentration from biodiesel fuels is observed than the diesel, because of the availability of oxygen in biodiesel, which promotes complete combustion resulting in higher gas temperature. It is reported that biodiesel contains

10 – 10% oxygen when compared to B100, B100 (PY) produces lower NO_x. This may be due to the presence of antioxidant in the biodiesel stored under optimum conditions. At 75% full load, B100 (PY) showed 8.42 % lower and 15.04% higher NO_x concentration with B100 and diesel respectively. Similar results were documented by many researchers [48, 67, 68, 72, 73].

3.7. Smoke density

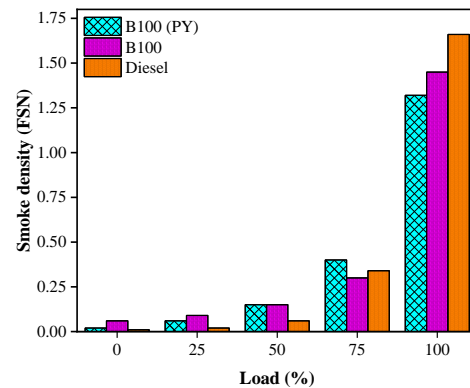


Figure 9. Smoke density vs load.

Fig.9. shows the difference in smoke density in terms of increase in engine load. An increase in smoke density is noted with a rise in engine load. At low and medium loads (no load to 50% load), the smoke density is less than 0.25FSN, because at these loads, the engine runs with larger quantities of excess air. Maximum smoke density was recorded at 100% full load for all the test fuels. At 75% and 100% loads, both biodiesel fuels showed lower smoke density. The smoke density of biodiesel was lower than diesel due to its oxygen content [69]. The use of B100 (PY) as fuel resulted in 9.83% and 25.72% lower smoke density compared to B100 and diesel respectively at 100% load. The presence of antioxidant in B100 (PY) would have resulted in more complete combustion resulting in lower smoke density. Similar results were obtained by many researchers [48, 58, 68].

3.8. HC emission

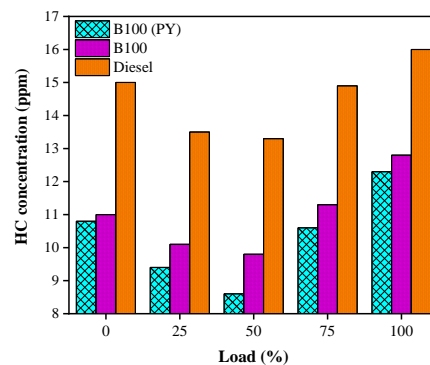


Figure 10. HC concentration vs load.

The variation of HC emission by B100 (PY), B100 and diesel are presented in Fig 10. The HC concentrations of the all fuels are found to be the maximum at full load. The oxygen content in biodiesel fuels namely resulted in lower HC concentration compared to diesel. The biodiesel stored under optimum condition showed lower HC compared to B100 and diesel. At 75% load, B100 (PY) has 33.31% lower HC concentration than diesel. Similar result was recorded in many research works [53, 67, 68, 72, 73].

Conclusion:

The Performance and emission parameters of a CI engine fuel by waste frying oil biodiesel stored under optimized condition (B100 (PY)) have been evaluated and likened with base line diesel fuel and B100. The storage conditions were optimized using response surface methodology. The optimized storage condition for waste frying oil biodiesel was found as antioxidant concentration 435 ppm, storage temperature 45°C and storage period 4 months. The engine performance results were summarised as follows:

- The brake specific fuel consumption with B100 (PY) was lesser than that of B100 because of oxidative degradation and operation by diesel fuel shows a higher rate, and causes the low content of energy in biodiesel.
- The BTE of B100 (PY) and B100 were lower compared to diesel due to their lower energy content. It is observed that at 100% load, more fuel is injected with very little excess air which leads to efficiency drop due to partial fuel combustion.
- Further, there was no significant difference in combustion characteristics, viz. cylinder gas pressure and heat release rate between B100 (PY) and diesel fuel.
- It is found that, the B100 has lowest ignition delay followed by diesel and B100 (PY).
- B100 (PY) shows high exhaust gas temperature than that of B100 and diesel fuel.
- The NO_x concentration was found to be higher for biodiesel fuels compared to diesel. This is due to the availability of oxygen in biodiesel.
- Biodiesel has lower smoke density than diesel due to its oxygen content. In addition to that, biodiesel with antioxidant have resulted low smoke density due to complete combustion .
- The biodiesel stored under optimum condition showed lower HC compared to B100 and diesel.
- The engine performance results indicate that biodiesel produced from waste frying oil has to be stored under optimum conditions to obtain comparable engine performance and lower emissions.

References

- [1] He, Chao, Yunshan Ge, Jianwei Tan, Kewei You, Xiukun Han, and Junfang Wang. "Characteristics of polycyclic aromatic hydrocarbons emissions of diesel engine fueled with biodiesel and diesel." *Fuel*, Vol. 89, no. 8, 2010, 2040-2046.
- [2] Alptekin, Ertan, and Mustafa Canakci. "Determination of the density and the viscosities of biodiesel–diesel fuel blends." *Renewable energy*, Vol. 33, no. 12, 2008, 2623-2630.
- [3] Arslan, Ridvan. "Emission characteristics of a diesel engine using waste cooking oil as biodiesel fuel." *African Journal of Biotechnology*, Vol. 10, no. 19, 2011. 3790-3794.
- [4] Hamasaki, Kazunori, Eiji Kinoshita, Hiroshi Tajima, Koji Takasaki, and Daizo Morita. "(3-09) Combustion Characteristics of Diesel Engines with Waste Vegetable Oil Methyl Ester ((AF-3) Alternative Fuels 3-Biomass Fuels and Fuel Design)." In *The Proceedings of the International symposium on diagnostics and modeling of combustion in internal combustion engines 01.204*, 55. The Japan Society of Mechanical Engineers, 2001.
- [5] Demirbas, Ayhan. "Importance of biodiesel as transportation fuel." *Energy policy*, Vol. 35, no. 9, 2007, 4661-4670.
- [6] Lebedevas, Sergejus, Galina Lebedeva, Violeta Makareviciene, Prutenis Janulis, and Egle Sendzikiene. "Usage of fuel mixtures containing ethanol and rapeseed oil methyl esters in a diesel engine." *Energy & Fuels*, Vol.23, no. 1, 2009, 217-223.
- [7] Supple, B., R. Howard-Hildige, Esther Gonzalez-Gomez, and J. J. Leahy. "The effect of steam treating waste cooking oil on the yield of methyl ester." *Journal of the American Oil Chemists' Society*, Vol. 79, no. 2, 2002, 175-178.
- [8] Zhang, Yen, M. A. Dube, D. D. L. McLean, and M. Kates. "Biodiesel production from waste cooking oil: 1. Process design and technological assessment." *Bioresource technology*, Vol. 89, no. 1, 2003, 1-16.
- [9] Lin, Cheng-Yuan, and Rong-Ji Li. "Engine performance and emission characteristics of marine fish-oil biodiesel produced from the discarded parts of marine fish." *Fuel Processing Technology*, Vol. 90, no. 7-8, 2009, 883-888.
- [10] Utlu, Zafer, and Mevlüt Süreyya Koçak. "The effect of biodiesel fuel obtained from waste frying oil on direct injection diesel engine performance and exhaust emissions." *Renewable energy*, Vol. 33, no. 8, 2008, 1936-1941.
- [11] Ramadhas, A. S., C. Muraleedharan, and S. Jayaraj. "Performance and emission evaluation of a diesel engine fueled with methyl esters of rubber seed oil." *Renewable energy*, Vol. 30, no. 12, 2005, 1789-1800.
- [12] Ryu, Kyunghyun, and Youngtaig Oh. "Combustion characteristics of an agricultural diesel engine using biodiesel fuel." *KSME International Journal*, Vol. 18, no. 4, 2004, 709-717.
- [13] Usta, N. "An experimental study on performance and exhaust emissions of a diesel engine fuelled with tobacco seed oil methyl ester." *Energy Conversion and Management*, Vol. 46, no. 15-16, 2005, 2373-2386.
- [14] Knothe, Gerhard. "Dependence of biodiesel fuel properties on the structure of fatty acid alkyl esters." *Fuel processing technology*, Vol. 86, no. 10, 2005, 1059-1070.

- [15] Xue, Jinlin, Tony E. Grift, and Alan C. Hansen. "Effect of biodiesel on engine performances and emissions." *Renewable and Sustainable energy reviews*, Vol. 15, no. 2, 2011, 1098-1116.
- [16] Mittelbach, Martin, and Peter Tritthart. "Diesel fuel derived from vegetable oils, III. Emission tests using methyl esters of used frying oil." *Journal of the American Oil Chemists' Society*, Vol. 65, no. 7, 1988, 1185-1187.
- [17] Lapuerta, Magin, José Rodríguez-Fernández, and John R. Agudelo. "Diesel particulate emissions from used cooking oil biodiesel." *Bioresource Technology*, Vol. 99, no. 4, 2008, 731-740.
- [18] Tat, Mustafa Ertunc. "Investigation of oxides of nitrogen emissions from biodiesel-fueled engines." 2003.
- [19] Canakci, Mustafa, and Jon H. Van Gerpen. "Comparison of engine performance and emissions for petroleum diesel fuel, yellow grease biodiesel, and soybean oil biodiesel." *Transactions of the ASAE*, Vol. 46, no. 4, 2003, 937.
- [20] Payri, F., V. Macián, J. Arregle, B. Tormos, and J. L. Martínez. Heavy-duty diesel engine performance and emission measurements for biodiesel (from cooking oil) blends used in the ECOBUS project. No. 2005-01-2205. SAE Technical Paper, 2005.
- [21] Agarwal, Avinash Kumar, and L. M. Das. "Biodiesel development and characterization for use as a fuel in compression ignition engines." *J. Eng. Gas Turbines Power*, Vol. 123, no. 2, 2001, 440-447.
- [22] Ulusoy, Yahya, Yucel Tekin, Merve Cetinkaya, and Filiz Karaosmanoglu. "The engine tests of biodiesel from used frying oil." *Energy Sources*, Vol. 26, no. 10, 2004, 927-932.
- [23] Cetinkaya, Merve, and Filiz Karaosmanoglu. "A new application area for used cooking oil originated biodiesel: generators." *Energy & fuels*, Vol. 19, no. 2, 2005, 645-652.
- [24] Kulkarni, Mangesh G., and Ajay K. Dalai. "Waste cooking oil an economical source for biodiesel: a review." *Industrial & engineering chemistry research*, Vol. 45, no. 9, 2006, 2901-2913.
- [25] Felizardo, Pedro, M. Joana Neiva Correia, Idalina Raposo, Joao F. Mendes, Rui Berkemeier, and Joao Moura Bordado. "Production of biodiesel from waste frying oils." *Waste management*, Vol. 26, no. 5, 2006, 487-494.
- [26] Gopal, K. Nantha, Arindam Pal, Sumit Sharma, Charan Samanchi, K. Sathyanarayanan, and T. Elango. "Investigation of emissions and combustion characteristics of a CI engine fueled with waste cooking oil methyl ester and diesel blends." *Alexandria Engineering Journal*, Vol. 53, no. 2, 2014, 281-287.
- [27] Kannan, G. R., and R. Anand. "Effect of injection pressure and injection timing on DI diesel engine fuelled with biodiesel from waste cooking oil." *Biomass and bioenergy*, Vol. 46, 2012, 343-352.
- [28] Kalam, M. A., H. H. Masjuki, M. H. Jayed, and A. M. Liaquat. "Emission and performance characteristics of an indirect ignition diesel engine fuelled with waste cooking oil." *Energy*, Vol. 36, no. 1, 2011, 397-402.
- [29] Humke, A. L., and N. J. Barsic. "Performance and emissions characteristics of a naturally aspirated diesel engine with vegetable oil fuels—(Part 2)." *SAE Transactions*, 1981, 2925-2935.
- [30] Masjuki, H. H., M. A. Kalam, M. A. Maleque, A. Kubo, and T. Nonaka. "Performance, emissions and wear characteristics of an indirect injection diesel engine using coconut oil blended fuel." *Proceedings of the Institution of Mechanical Engineers, Part D: Journal of Automobile Engineering*, Vol. 215, no. 3, 2001, 393-404.
- [31] Altıparmak, Duran, Ali Keskin, Atilla Koca, and Metin Gürü. "Alternative fuel properties of tall oil fatty acid methyl ester–diesel fuel blends." *Bioresource technology*, Vol. 98, no. 2, 2007, 241-246.
- [32] Felizardo, Pedro, M. Joana Neiva Correia, Idalina Raposo, Joao F. Mendes, Rui Berkemeier, and Joao Moura Bordado. "Production of biodiesel from waste frying oils." *Waste management*, Vol. 26, no. 5, 2006, 487-494.
- [33] Kaplan, Cafer, Ridvan Arslan, and Ali Sürmen. "Performance characteristics of sunflower methyl esters as biodiesel." *Energy Sources*, Vol. 28, no. 8, 2006, 751-755.
- [34] Kulkarni, Mangesh G., and Ajay K. Dalai. "Waste cooking oil an economical source for biodiesel: a review." *Industrial & engineering chemistry research*, Vol. 45, no. 9, 2006, 2901-2913.
- [35] Nachid, Marouane, Fatiha Ouanji, Mohamed Kacimi, Leonarda F. Liotta, and Mahfoud Ziyad. "Biodiesel from moroccan waste frying oil: the optimization of transesterification parameters impact of biodiesel on the petrodiesel lubricity and combustion." *International Journal of Green Energy*, Vol. 12, no. 8, 2015, 865-872.
- [36] Selvan, Tamil, and G. Nagarajan. "Combustion and emission characteristics of a diesel engine fuelled with biodiesel having varying saturated fatty acid composition." *International journal of green energy*, Vol. 10, no. 9, 2013, 952-965.
- [37] Ulusoy, Yahya, Ridvan Arslan, Cafer Kaplan, Alper Bolat, Haşmet Cedden, Alper Kaya, and Gürkan Günç. "An investigation of engine and fuel system performance in a diesel engine operating on waste cooking oil." *International journal of green energy*, Vol. 13, no. 1, 2016, 40-48.
- [38] Abu-Jrai, A., Jehad A. Yamin, H. Ala'a, and Muhanned A. Hararah. "Combustion characteristics and engine emissions of a diesel engine fueled with diesel and treated waste cooking oil blends." *Chemical Engineering Journal*, Vol. 172, no. 1, 2011, 129-136.
- [39] Lin, Yuan-Chung, Kuo-Hsiang Hsu, and Chung-Bang Chen. "Experimental investigation of the performance and emissions of a heavy-duty diesel engine fueled with waste cooking oil biodiesel/ultra-low sulfur diesel blends." *Energy*, Vol. 36, no. 1, 2011, 241-248.
- [40] Hirkude, Jagannath, and Atul S. Padalkar. "Experimental investigation of the effect of compression ratio on performance and emissions of CI engine operated with waste fried oil methyl ester blend." *Fuel processing technology*, Vol. 128, 2014, 367-375.

- [41] Tesfa, Belachew, Rakesh Mishra, C. Zhang, F. Gu, and A. D. Ball. "Combustion and performance characteristics of CI (compression ignition) engine running with biodiesel." *Energy*, Vol. 51, 2013, 101-115.
- [42] Gopal, K. Nantha, Arindam Pal, Sumit Sharma, Charan Samanchi, K. Sathyanarayanan, and T. Elango. "Investigation of emissions and combustion characteristics of a CI engine fueled with waste cooking oil methyl ester and diesel blends." *Alexandria Engineering Journal*, Vol. 53, no. 2, 2014, 281-287.
- [43] Ahmed, Sanjid, Masjuki Hj Hassan, Md Abul Kalam, SM Ashrafur Rahman, Md Joynul Abedin, and Ali Shahir. "An experimental investigation of biodiesel production, characterization, engine performance, emission and noise of Brassica juncea methyl ester and its blends." *Journal of cleaner production*, Vol. 79, 2014, 74-81.
- [44] Chuah, Lai Fatt, Abdul Rashid Abd Aziz, Suzana Yusup, Awais Bokhari, Jiří Jaromír Klemes, and Mohd Zamri Abdullah. "Performance and emission of diesel engine fuelled by waste cooking oil methyl ester derived from palm olein using hydrodynamic cavitation." *Clean Technologies and Environmental Policy*, Vol. 17, no. 8, 2015, 2229-2241.
- [45] Dorado, M. P., E. Ballesteros, J. M. Arnal, J. Gomez, and F. J. Lopez. "Exhaust emissions from a Diesel engine fueled with transesterified waste olive oil." *Fuel*, Vol. 82, no. 11, 2003, 1311-1315.
- [46] Hess, Melissa A., Michael J. Haas, Thomas A. Foglia, and William N. Marmar. "Effect of antioxidant addition on NO_x emissions from biodiesel." *Energy & Fuels*, Vol. 19, no. 4, 2005, 1749-1754.
- [47] Ryu, Kyunghyun. "The characteristics of performance and exhaust emissions of a diesel engine using a biodiesel with antioxidants." *Bioresource technology*, Vol. 101, no. 1 2010, 78-82.
- [48] Ileri, Erol, and Günnür Koçar. "Experimental investigation of the effect of antioxidant additives on NO_x emissions of a diesel engine using biodiesel." *Fuel*, Vol. 125, 2014, 44-49.
- [49] I.M. Rizwanul Fattah, H.H Masjuki, M.A Kalam, M. Mofijur, M.J Abedin, "Effect of antioxidant on the performance and emission characteristics of a diesel engine fueled with palm biodiesel blends". *Energy Conversion and Management*, Vol. 79, 2014, 265-272.
- [50] Roy, Murari Mohon, Wilson Wang, and Majed Alawi. "Performance and emissions of a diesel engine fueled by biodiesel–diesel, biodiesel–diesel-additive and kerosene–biodiesel blends." *Energy Conversion and Management*, Vol. 84, 2014, 164-173.
- [51] Balaji, S., R. Saravanan, and N. Kapilan. "Influence of pyrogallol antioxidant on performance and emissions of a CI fuelled with neem oil biodiesel." *International Journal of Mechanical Engineering and Technology*, Vol. 8, no. 8, 2017, 981-987.
- [52] Varatharajan, K., and M. Cheralathan. "Effect of aromatic amine antioxidants on NO_x emissions from a soybean biodiesel powered DI diesel engine." *Fuel processing technology*, Vol. 106, 2013, 526-532.
- [53] Balaji, G., and M. Cheralathan. "Experimental investigation of antioxidant effect on oxidation stability and emissions in a methyl ester of neem oil fuelled DI diesel engine." *Renewable Energy*, Vol. 74, 2015, 910-916.
- [54] Sharma, Abhishek, and S. Murugan. "Effect of blending waste tyre derived fuel on oxidation stability of biodiesel and performance and emission studies of a diesel engine." *Applied Thermal Engineering*, Vol. 118, 2017, 365-374.
- [55] Palash, S. M., M. A. Kalam, H. H. Masjuki, M. I. Arbab, B. M. Masum, and A. Sanjid. "Impacts of NO_x reducing antioxidant additive on performance and emissions of a multi-cylinder diesel engine fuelled with Jatropha biodiesel blends." *Energy Conversion and Management*, Vol. 77, 2014, 577-585.
- [56] Serrano, Marta, Abderrahim Bouaid, Mercedes Martínez, and José Aracil. "Oxidation stability of biodiesel from different feedstocks: influence of commercial additives and purification step." *Fuel*, Vol. 113, 2013, 50-58.
- [57] Varatharajan, K., M. Cheralathan, and R. Velraj. "Mitigation of NO_x emissions from a jatropha biodiesel fuelled DI diesel engine using antioxidant additives." *Fuel*, Vol. 90, no. 8, 2011, 2721-2725.
- [58] Balaji, G., and M. Cheralathan. "Experimental investigation to reduce emissions of CI (compression ignition) engine fuelled with methyl ester of cottonseed oil using antioxidant." *International Journal of Ambient Energy*, Vol. 35, no. 2014, 13-19.
- [59] Kivevele, Thomas T., Lukács Kristóf, Ákos Bereczky, and Makame M. Mbarawa. "Engine performance, exhaust emissions and combustion characteristics of a CI engine fuelled with croton megalocarpus methyl ester with antioxidant." *Fuel*, Vol. 90, no. 8, 2011, 2782-2789.
- [60] Venkata Subbaiah, G.. "An Investigation on the Performance Characteristics of a Diesel Engine using Diesel-Rice Bran Biodiesel Blends at Different Injection Pressures." *International Journal of Mechanical Engineering & Technology (IJMET)*, Vol. 6, no. 1, 2015, 20-27.
- [61] Balaji, G., and M. Cheralathan. "Experimental investigation to reduce exhaust emissions in a single cylinder CI engine fuelled with methyl ester of neem oil using antioxidant (L-ascorbic acid)." *Biofuels*, Vol. 7, no. 3, 2016, 305-312.
- [62] Varatharajan, K., and M. Cheralathan. "Effect of aromatic amine antioxidants on NO_x emissions from a soybean biodiesel powered DI diesel engine." *Fuel processing technology*, Vol. 106, 2013, 526-532.
- [63] Xiaoming, Lu, Ge Yunshan, Wu Sijin, and Han Xiukun. "An experimental investigation on combustion and emissions characteristics of turbocharged DI engines fuelled with blends of biodiesel. No. 2005-01-2199. SAE Technical Paper, 2005.
- [64] Szybist, James P., Andre L. Boehman, Joshua D. Taylor, and Robert L. McCormick. "Evaluation of formulation strategies to eliminate the biodiesel NO_x effect." *Fuel Processing Technology*, Vol. 86, no. 10, 2005, 1109-1126.
- [65] Knothe, Gerhard, and Robert O. Dunn. "Dependence of oil stability index of fatty compounds on their structure and concentration and presence of metals." *Journal of the American Oil Chemists' Society*, Vol. 80, no. 10, 2003, 1021-1026.
- [66] Heywood, J. B. "Internal Combustion Engine Fundamentals, McGraw-Hill, New York." 1988.
- [67] Balaji, G., and M. Cheralathan. "Study of antioxidant effect on oxidation stability and emissions in a methyl ester of neem oil fuelled DI diesel engine." *Journal of the Energy Institute*, Vol. 87, no. 3, 2014, 188-195.
- [68] Rashedul, H. K., Haji Hassan Masjuki, M. A. Kalam, Y. H. Teoh, H. G. How, and IM Rizwanul Fattah. "Effect of antioxidant on the oxidation stability and combustion–performance–emission characteristics of a diesel engine fuelled with diesel–biodiesel blend." *Energy Conversion and Management*, Vol. 106, 2015, 849-858.
- [69] Chauhan, Bhupendra Singh, Naveen Kumar, and Haeng Muk Cho. "A study on the performance and emission of a diesel

- engine fueled with Jatropha biodiesel oil and its blends." *Energy*, Vol. 37, no. 1, 2012, 616-622.
- [70] Zafer Aydin and Aykut Safa. "Performance and emission characteristics of waste frying oil biodiesel blends as pilot fuel on a dual fuel compression ignition engine". *Energy Sources, Part A: Recovery, Utilization, and Environmental Effects*, Vol. 11, 2020, 1-16.
- [71] Ajay V. Kolhe, R.E. Shelke and S.S. Khandare. "Performance and Combustion Characteristics of a DI Diesel Engine Fueled with Jatropha Methyl Esters and its Blends." *Jordan Journal of Mechanical and Industrial Engineering*, Vol. 8, No. 1, 2014, 7-12.
- [72] T. Venkateswara Rao. "Experimental Investigation of Pongamia, Jatropha and Neem Methyl Esters as Biodiesel on C.I. Engine", *Jordan Journal of Mechanical and Industrial Engineering*, Vol. 2, No. 2, 2008, 117-122.
- [73] A. Siva Kumar et al., "Comparison of Diesel Engine Performance and Emissions from Neat and Transesterified Cotton Seed Oil". *Jordan Journal of Mechanical and Industrial Engineering*, Vol. 3, No. 3, 2009, 190-197.

Impact of Carbon Nano Tubes on the Performance and Emissions of a Diesel Engine Fuelled with Pongamia Oil Biodiesel

N.Kapilan

Nitte Meenakshi Institute of Technology, Bengaluru, India

Received July 28 2020

Accepted June 23 2021

Abstract

Biodiesel is considered an immediate substitute for the fossil diesel as the fuel properties, such as calorific value, density, ash content and acid value are comparable to the diesel. In India, pongamia oil has considerable potential for the biodiesel production. The pongamia oil biodiesel has lower volatility and slightly higher viscosity than the diesel. Hence the pongamia oil biodiesel fuelled diesel engine results in lower thermal efficiency as compared to the diesel. The carbon nanotubes (CNTs) were used in this work as additive to the pongamia oil biodiesel, to enhance the atomization and to reduce the ignition delay of the pongamia oil biodiesel. The CNTs were added to the pongamia oil biodiesel with different dosages and subjected to ultrasonication for 60 min, to prepare homogenous mixture. The engine tests were conducted on a single cylinder diesel engine without making any modifications in the fuel injection system. The addition of CNTs to the pongamia oil biodiesel resulted in higher brake thermal efficiency at higher loads between 75 to 100 % of the full load. From the engine tests, it was observed that the CNTs improves the engine thermal efficiency and reduces the CO, HC and smoke emissions of the diesel engine depends upon the CNT dosage. This is due to shorten ignition delay caused by the CNTs which improves the combustion of the pongamia oil biodiesel. The optimum CNT dosage of 50 mg/l results in 4% increase in thermal efficiency and reduces the CO, HC and smoke emissions by 20.33, 25 and 12.5% respectively at full load.

© 2021 Jordan Journal of Mechanical and Industrial Engineering. All rights reserved

Keywords: pongamia oil, biodiesel, alternative fuel, carbon nanotubes, engine tests;

1. Introduction

Most of the countries worry about the recent increase in air pollution which causes environmental degradation. The increase in number of diesel vehicles will increase air pollution issues. The energy demand of the globe increases due to industrialization and fossil fuels supply the current energy requirements (Geetesh et al 2021). The energy sources greatly affect the country's economic growth and hence the energy sources should be affordable, accessible and environmentally friendly. It is reported that the energy demand of countries which are not members of the organization for economic co-operation and development Asian region is projected to increase during the period of 2015 to 2040 (eia., 2017). Over the past four decades, the world's rapid growth in energy demand has mainly been satisfied by fossil fuels. Oil, coal, natural gas, hydroelectric, nuclear energy, and renewables accounted for 33.6, 27.2, 23.9, 6.8, 4.4 and 4% of the world's primary energy consumption in 2018, respectively. On the other hand, fossil fuels accounted for 84.7% of world primary energy consumption in 2018 (BP 2019). The global social, economic, political, environmental and technological changes create a fundamentally different outlook for the international energy markets. It is expected that a different future would be characterized by shale oil and shale gas revolution (Ghasemian et al., 2020). It is estimated that the

world's oil demand will increase to 105.4 MMbpd in 2030 from the 96.9 MMbpd recorded in 2018 and hence alternative energy sources will be utilized to meet the energy demand of the world (Josiah et al 2020). The biodiesel is suggested as renewable replacement to diesel (Sameh et al., 2018) and is produced by transesterification reaction (GeeteshGoga, 2018). The biodiesel does not have sulphur, and thus results in lower sulfur dioxide emission as compared to diesel (Ajay et al., 2014).

In Asia, India is one of the largest energy consumers (Anindita et al., 2016) and India's biofuel policy encourages biodiesel production from non-edible oils to reduce the demand of fossil diesel (Mnre., 2018). This policy aims to ensure availability of minimum quantity of biofuels in the market (Gain., 2017). It reduces the oil import and to meet the regional energy demand by using non-food feed stocks (Gain., 2016). The production cost of biodiesel is high and hence newer technologies are being developed (Kapilan et al., 2014). The ultrasound assisted biodiesel production method results in higher biodiesel yield and reduces reaction time (Ibrahim et al., 2020). The biodiesel derived from rice bran oil can be blended with n-butanol, and thus can be used as a fuel in compression ignition engine (GeeteshGoga, 2019). In dual fuel mode, mass flowrate of biogas must be optimized (GeeteshGoga, 2020).

The ignition delay period of the biodiesel is higher than the diesel (Balaji et al., 2015) and hence the additives can be added with biodiesel to reduce the ignition delay period which enhances the combustion of the fuel. The diethyl

* Corresponding author e-mail: kapil_krecmech@yahoo.com.

ether can be used as oxygenated additive to enhance the ignition by decreasing the ignition delay of fuel in the compression ignition engine (Mohanan et al., 2003).

The addition of alumina nanoparticles to the biodiesel diesel blend increases the brake thermal efficiency and reduces the CO and HC emissions of the engine (Seyyed et al., 2017). The use of graphene oxide as additive in *ailanthus altissima* biodiesel results in higher power and reduces the CO and HC emissions (Hoseini et al., 2018). The addition of graphene nano-platelets to the *Jatropha* biodiesel diesel blend increases thermal efficiency of the engine as compared to biodiesel blend (Ahmed et al., 2018). The engine tests conducted on a variable speed compression ignition engine with CNTs added emulsion of water and diesel shows enhancement in thermal efficiency and reduction in smoke emission (Sadhik and Anand., 2011). It is reported that the CNTs improves the homogenization of mixture of fuel and air and reduces the emission levels of blends of biodiesel and diesel fuelled C.I. engine (Vivek and Kriplani 2016).

The cost of the CNTs varies between US \$ 15 to 35 per g, depends upon purity. The addition of CNTs to the biodiesel is in mg and hence a marginal increase in the operating cost. This cost is almost similar to the cost of higher alcohols or gaseous fuels. The fire hazards related to alcohols and gaseous fuels are very high and additional retrofitting are required to supply these fuels to the combustion chamber which increases investment cost. Hence, in recent years, researchers are using nanoparticles to enhance the performance of the fuel. From the literature, it is observed that biodiesel has lower volatility and higher viscosity. A small dosage of nanoparticles results in improvement in the properties and combustion of the biodiesel. It is also observed from the literature that, no work has been carried out to study the effect of CNT on the performance of constant speed diesel engine fuelled with biodiesel, without making any modification in the engine's injection timing and injection pressure. Hence in this work, an attempt was made to understand the effect of CNT on the performance and emissions of biodiesel fuelled constant speed engine which is most widely used in agricultural purpose. It is reported that the optimum multi walled carbon nanotubes dosage for the biodiesel blend is 30 mg/l for the variable speed engine (Ahmed et al 2016.). In this work, biodiesel was used as the fuel and hence higher dosages such as 40, 50 and 60 mg/l were considered.

The pongamia is a tree that grows to about 15 to 25 m height with a large canopy. It does not need much maintenance and grows in dry areas. The flowering generally starts after 3 to 4 years and the brown seed pods appear immediately after flowering. The pods are thick, and they contain one or two bean like brownish red seeds. Figure 1 shows the seeds.



Figure 1. Pongamia Seeds

Generally non-edible oils are used as raw material for the production of biodiesel (Kapilan et al., 2011) and non-

edible pongamia oil is cheap and has considerable potential for biodiesel production compared to waste cooking oil, eucalyptus oil, and linseed oil..etc. The pongamia oil biodiesel can be used as fuel in compression ignition engine without making any modifications in the fuel injection system (Noel et al., 2016). The volatility of the biodiesel can be enhanced with the addition of ethanol, and it is suggested that 5 to 10% of ethanol can be added with biodiesel which results in acceptable engine performance (Al-Hassan et al., 2012). The stability of the biodiesel diesel blend can be increased with ultrasonic treatment (Dong et al., 2019).

The pongamia oil biodiesel fuelled diesel engine results in lower thermal efficiency due to lower volatility and slightly higher viscosity of the biodiesel, and thus it is necessary to improve the performance of pongamia oil biodiesel fuelled engine. The nanoparticle which has better thermal and physical properties can be used to increase the properties of the biodiesel. The CNT has higher surface area to volume ratio and higher thermal conductivity and hence it was used as additive in this work. Also, we have optimized the dosage of CNT required for the biodiesel based on better thermal efficiency and lower emissions.

2. Materials and Methodology

The pongamia oil was used as raw materials to produce biodiesel using a two step transesterification process as the acid value of the pongamia oil was high. Methanol was used as the alcohol and the molar ratio of oil to methanol considered in this work was 1:6. The sulfuric acid was used as catalyst in the esterification reaction which is the first step to reduce the acid value of the pongamia oil to less than 1 and the reaction was carried out for 90 min. This treated pongamia oil was converted into biodiesel in transesterification reaction using potassium hydroxide as the catalyst and the reaction was carried out for 90 min. This method results in the biodiesel yield of 91 %. The fatty acid composition of pongamia oil biodiesel was determined using gas chromatography and it shows that this biodiesel contains oleic acid (36%), palmitic acid (10%), stearic acid (7%), behenic acid (6%), linoleic acid (19%) and arachidonic acid (1%). Table 1 shows the details of the chemicals used for the biodiesel production.

Table 1. Chemicals used for biodiesel production

Name of the Chemical	Manufacturer	Purity
Methanol	Merck	99 %
Sulfuric acid	Merck	98 %
Potassium hydroxide	Merck	99%

The CNTs were procured from NITK, Surathkal, India. The CNTs of 40, 50 and 60 mg were mixed in one litre of pongamia oil biodiesel and subjected to ultrasonication for 60 min using ultrasonic bath to prepare the homogenous mixture and is shown in the figure 2. The CNTs with the dosage of 40, 50 and 60 mg/l are represented in this work as BDCN40, BDCN50 and BDCN60. The properties of the diesel, biodiesel and biodiesel with different concentrations of CNTs were determined as per the ASTM procedures. A redwood viscometer was used to measure the kinematic viscosity (ASTM D 445-03) of the pongamia oil biodiesel. The calorific value (ASTM D 240-03) and density (ASTM D4052-96) of the pongamia oil biodiesel was determined using bomb calorimeter and relative density bottle,

respectively. A Cleveland open cup tester was used to measure the flash point of the biodiesel (ASTM D92-18).



Figure 2. Biodiesel subjected to ultrasonication

3. Engine experimental setup

A diesel engine which is most widely used for agricultural purpose was modified to work as an experimental setup. Figure 3 shows the engine used for the experiments. The diesel engine used in this work is a direct injection, water cooled, naturally aspirated compression ignition engine and its technical specifications details are given in the Table 2. The engine load is the force which resists the power produced by the engine. The load on the engine was varied using eddy current dynamometer as it significantly affects the thermal efficiency and engine emissions (Man et al., 2016). An eddy current dynamometer was attached to the engine using coupling. A load cell was attached to the dynamometer to measure the engine load. A rotameter was used to control the flow rate of water supplied to the engine. The engine was retrofitted with air box, fuel tank, manometer, fuel measuring unit, transmitters for fuel flow measurement and process indicator. The exhaust gas temperature was measured using K-Type thermocouple. The engine is naturally aspirated. The engine governor varies the fuel injected into the engine by adjusting fuel pump to meet the required load. All the engine tests were carried out on the same day. The engine brake power and brake thermal efficiency were determined using the equation I and II.

Table 2. Engine details

Engine	1 cylinder, 4 stroke, naturally aspirated, direct injection C.I engine
Make and model	Kirloskar; model TV1
Displacement (cc)	661
Maximum brake power (kW)	5.2 at 1500 rpm
Compression ratio of the engine	17.5 : 1
Engine bore (mm)	87.5
Engine stroke (mm)	110
Fuel injection time of engine	23 degree bTDC
Injector nozzle opening pressure (bar)	200



Figure 3. Engine experimental setup

$$\text{Brake Thermal Efficiency in \%} = \frac{\text{Brake Power}}{m_f \cdot C.V} \times 100 \quad (1)$$

$$\text{Brake Power in kW} = \frac{2 \pi N T}{60} \quad (2)$$

Where, m_f – Mass of fuel consumed, kg/s

C.V – Calorific Value of the fuel, kJ/kg

N – Engine speed, rpm

T – Torque on the engine, kN-m

4. Engine Tests Procedure

The engine tests were carried out with pongamia oil biodiesel to obtain baseline data and the engine tests were carried out at constant speed. The natural aspiration system is used in this engine. The schematic view of engine setup is shown in Figure 4. The emissions of the engine were measured using a gas analyzer and smoke meter and details are given in Table 3. The leak test and purging were carried out before emission test. The gas analyzer's probe was placed into the engine's exhaust tube to measure the emission level.

The engine tests were carried out with pure biodiesel (B100) to get baseline data at steady state condition. The engine was started by manual cranking and after reaching steady state condition, important observations were recorded at no load condition. Then the engine load was increased to 25% of the full load using eddy current dynamometer and important observations were recorded. Then the engine load was increased to 50, 75 and 100 % of full load and the observations were recorded. After the engine tests, the B100 was drained from the fuel tank and fuel filter. Then the BDCN40 was filled in the fuel tank and fuel nozzle was removed. The hand cranking of the engine results in discharge of BDCN40 in the fuel injector and it was collected to remove the traces of biodiesel. Then the fuel injector was fixed into its original position and engine was started with BDCN40 and run for 15 min. The important observations and emissions were recorded at steady state condition. Similar procedure was followed for BDCN50 and BDCN60.

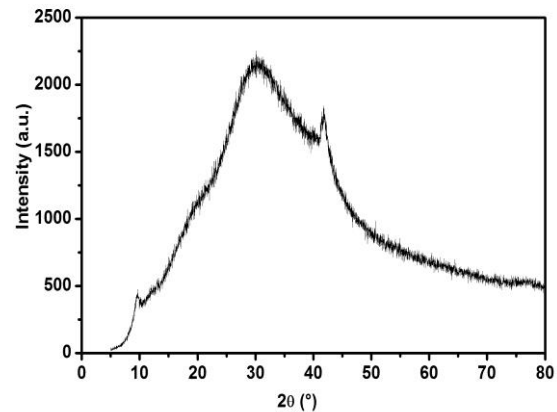
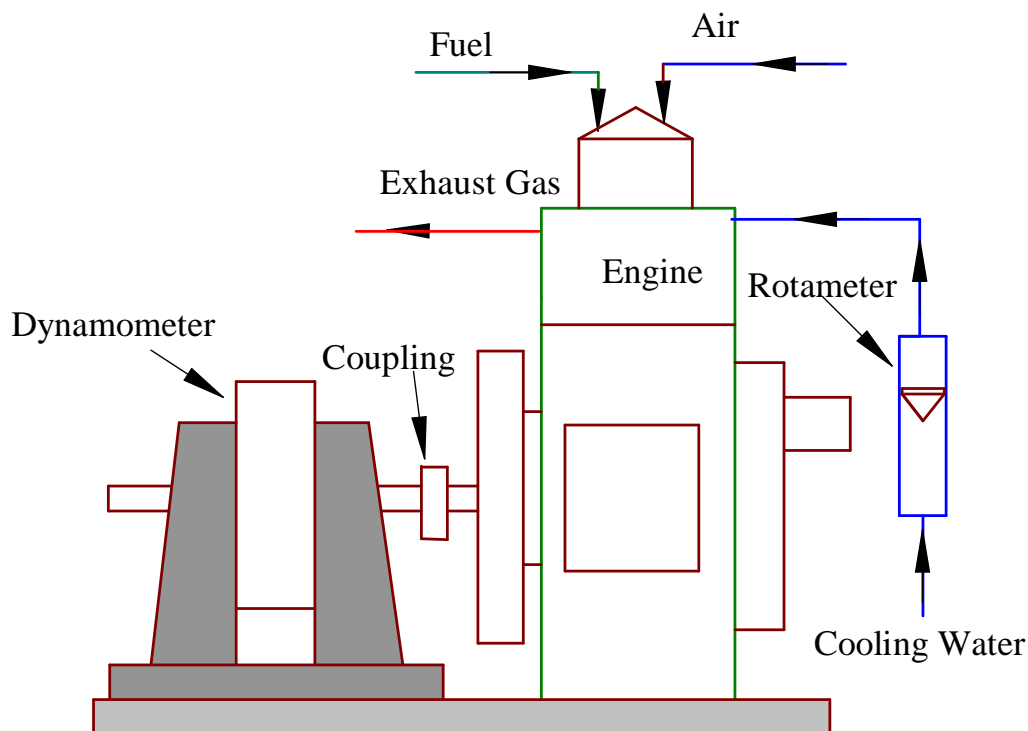
Table 3. Details of Engine Exhaust Gas Analyser

Make and model	AVL India; Digas 444 N		
Type of emission	Range	Accuracy	Uncertainty
CO emission (% vol)	0 to 15	±0.01	1.0
HC emission (ppm)	0 to 20000	±10.00	0.5
NOx emission (ppm)	0 to 5000	±50.00	1.0
Smoke meter			
Make and model	AVL; 437C		
Range (%)	0 to 100 %	±1.00	1.0

5. Results and Discussions

The biodiesel was produced from pongamia oil and CNTs were added with this biodiesel to study its effect on engine performance and emissions. Table 4 shows the properties of the diesel, biodiesel and biodiesel added with CNTs. Each property was measured three times and the average value was considered. This table shows that the addition of CNTs to the biodiesel affects the properties of the pongamia oil biodiesel. The flash point of the biodiesel decreases with the addition of CNTs. The calorific value of the biodiesel increases with the addition of CNTs. The structural properties of the CNT were measured using X-ray

diffraction. Figure 5 shows the X-ray diffraction image of the CNT. The XRD pattern of CNTs is close to those of graphite as CNTs is intrinsic in nature. The lower part of the X-ray diffraction peaks become broader as compared to graphite, due to crystallinity in carbon materials.

**Figure 5.** X-ray diffraction image of the CNT (Zahra et al. 2017)**Figure 4.** Schematic of the engine experimental setup**Table 4.** Comparison of fuel properties

S.No	Property	Diesel	B100	BDCN40	BDCN50	BDCN60	ASTM*
1	Flash Point of fuel (° C)	68	142	140	139	138	>130
2	Density of fuel (kg/m ³)	841	872	874	875	877	900
3	Viscosity of fuel at 40 ° C(mm ² /s)	2.7	4.8	4.83	4.86	4.88	1.9-6
4	Calorific Value of fuel (MJ/kg)	42.9	37.1	37.3	37.4	37.6	>33000

* Geetesh et al, 2019.

6. Fuel Droplet Size

When the fuel is injected into the combustion chamber, it is atomized and then fuel spray formation takes place. It is reported that the mean fuel droplet size of diesel and biodiesel are about 21 and 76 μm respectively. It shows that the biodiesel droplet size is about three times higher than the diesel. This is due to higher kinematic viscosity and surface tension of the biodiesel (Tizane et al., 2013). This large difference in fuel droplet size affects the fuel spread angle and spray penetration, which affects the mixing of fuel and air, fuel evaporation and combustion (Pawel&Róbert, 2018).

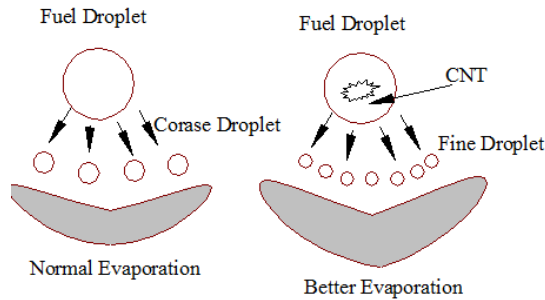


Figure 5. Schematic of fuel droplet breaking and evaporation

The fuel spray formation is affected by the surface tension and viscosity of the fuel. Figure 5 shows the schematic of fuel droplet breaking in the combustion chamber and evaporation of the tiny fuel droplets which form the fine spray. The biodiesel has higher viscosity, intermolecular bonding and surface tension and the addition of CNT reduces the intermolecular bonding and breaks the fuel droplets into tiny particles which increases the evaporation and causes better spray formation (Nikhil et al., 2020).

The engine tests were carried out without making any modifications in the fuel injection system. The effect of CNTs on the engine performance is discussed in the following paragraphs. The effect of CNTs on the brake thermal efficiency of the engine at different loads is shown in the figure 6. From the figure, it is observed that the brake thermal efficiency increases with increase in load. This is due to reduction in friction losses with increase in load. The viscosity and intermolecular attraction of the pongamia oil biodiesel is higher than diesel. This results in higher ignition delay and hence pongamia oil biodiesel has lower premixed combustion phase and higher diffusive combustion phase. The addition of highly reactive CNTs to the pongamia oil biodiesel helps to break the biodiesel droplets into small molecule which results in better evaporation and combustion of the fuel (Tizane et al., 2013). However, the CNT dosage affects the brake thermal efficiency, and it has to be optimized. The CNTs dosage with biodiesel, BDCN50, results in higher BTE as compared to the biodiesel and other CNT dosages at higher loads. The optimized dosage provides higher surface to volume ratio which enhances the heat transfer between the fuel droplets and improves the fuel droplet atomization and the combustion process. The higher dosage of CNT, BDCN60, affects the fuel atomization and spray formation. This phenomenon increases the ignition delay and affects the preflame reaction, cylinder pressure and heat release rate. It is reported in the literature (Pankaj et al., 2021 and Harish et al., 2020) that the higher dosage of nanoparticle results poor combustion which results in higher ignition delay, lower cylinder pressure and lower heat release rate as compared to

other dosages. Paramashivaiah et al reported that the higher dosage of graphene nanoparticle reduces the thermal efficiency of Simarouba biodiesel fuelled diesel engine due to poor atomization which increases fuel consumption and reduces the brake thermal efficiency.

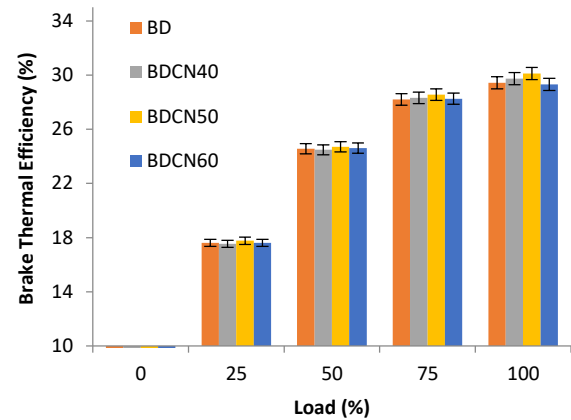


Figure 6. Brake Thermal Efficiency Vs Load

Figure 7 depicts the variation in exhaust gas temperature (EGT) of the engine at different loads with different dosages of CNTs. The exhaust gas temperature was measured at the outlet of the engine. From the figure, we observe that the exhaust gas temperature value increases with increase in engine load due to consumption of higher amount of fuel by the engine at higher loads. The exhaust gas temperature of BDCT60 is lower than the BDCT40 and BDCT50 at higher loads. This is due to poor atomization and spray formation (Brandão and Suarez, 2018). The exhaust gas temperature of BDCN50 is higher than other dosages due to reduction in ignition delay and improvement in premixed combustion which results in better combustion and higher combustion temperature. The higher combustion temperature results in higher exhaust gas temperature. In literature (Sadhik Basha J and R B Anand, 2011), it is reported that the addition of CNT reduces the ignition delay period of the fuel.

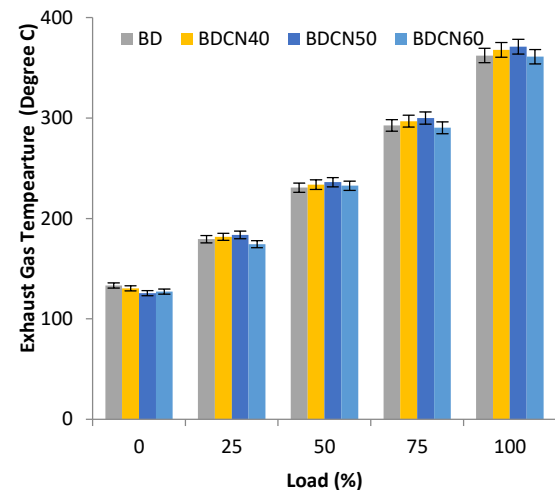


Figure 7. Exhaust Gas Temperature Vs Load

The poor mixing of fuel and air, locally rich zone and incomplete combustion of fuel results in higher carbon monoxide (CO) emission of the engine. The carbon monoxide also indicates poor combustion. The variation in carbon monoxide emission of the pongamia oil biodiesel fuelled engine with different CNTs dosage is represented in the Figure 8. It is observed that the carbon monoxide

emission of the engine increases from part load to full load due to reduction in air to fuel ratio. The compression ignition engine emits higher carbon monoxide with pongamia oil biodiesel at all loads as compared to other fuels. The addition of CNT to the pongamia oil biodiesel results in improvement in premixed and diffusion combustion phases. This results in lower carbon monoxide level (Balaji et al., 2015). The addition of CNT with the dosage of 50 mg/l, to the biodiesel reduces the carbon monoxide emission significantly as compared to other CNT dosages. This optimum CNT dosage results in reduction in ignition delay and enhanced fuel to air mixing which improves the premixed combustion. This phenomenon results in lower carbon monoxide level as compared to other dosages. The BDCT40 results in lower carbon monoxide level as compared to BDCT60 as the higher dosage causes poor atomization which results in incomplete combustion of fuel and higher CO emission (Paramashivaiah et al. 2018)

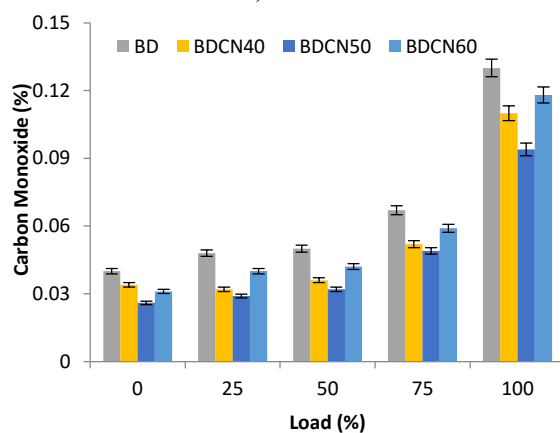


Figure 8. Carbon monoxide Vs Load

The incomplete combustion of the fuel causes the formation of unburned hydrocarbon (HC) emission in the compression ignition engine. Figure 9 depicts the HC emission of the engine with biodiesel, and biodiesel added with different dosages of CNTs, and it is observed that the hydrocarbon emission of the engine increases with load due to consumption of higher amount of fuel by the compression ignition engine. The addition of CNTs to the biodiesel reduces the hydrocarbon emission of the compression ignition engine. The higher viscosity of the biodiesel causes lower premixed combustion phase and higher diffusive combustion phase. The addition of highly reactive CNTs to biodiesel breaks the biodiesel droplets into small molecule and causes better mixing of fuel and air. This process improves evaporation of fuel and improves the premixed combustion. The improvement in the fuel evaporation and premixed combustion results in better combustion and reduces the hydrocarbon emission level. This behavior is similar to work done by Tizane et al., 2013. The BDCN50 results in lower hydrocarbon emission as compared to other CNT dosages due to its ability to improve the pre-mixed combustion as compared to other CNT dosages. The BDCN60 results in higher hydrocarbon emission due to poor combustion and this result is comparable to similar type of work reported in literature (Seyyed et al. 2017).

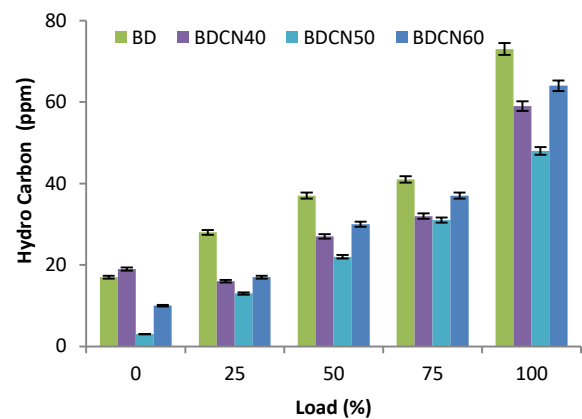


Figure 9. Hydro Carbon Vs Load

Figure 10 depicts the oxides of nitrogen (NOx) emission of the C.I. engine at various loads with pongamia oil biodiesel and pongamia oil biodiesel added with various dosages of the CNTs. The oxides of nitrogen emission is formed during the premixed combustion phase of the fuel. The improvement in premixed combustion causes better combustion and higher combustion temperature. The oxides of nitrogen emission level is low at lower loads due to lower combustion temperature. However as the load increases, the fuel consumption increases which result in higher combustion temperature and higher oxides of nitrogen emission level (Ahmet Uyumaz et al., 2020, Álvaro et al., 2019). The addition of CNTs to the biodiesel increases the oxides of nitrogen emission. The CNTs improve the fuel and air mixing and premixed combustion which results in better combustion and higher combustion temperature. This results in higher oxides of nitrogen emission. However, the oxides of nitrogen emission vary with the CNT dosage. The increase in CNT dosage increases the oxides of nitrogen level. The oxides of nitrogen emission of BDCN50 is higher than the other dosages due to better combustion of biodiesel which results in higher oxides of nitrogen emission. The BDCN60 results in lower oxides of nitrogen emission as compared to other dosages at higher loads.

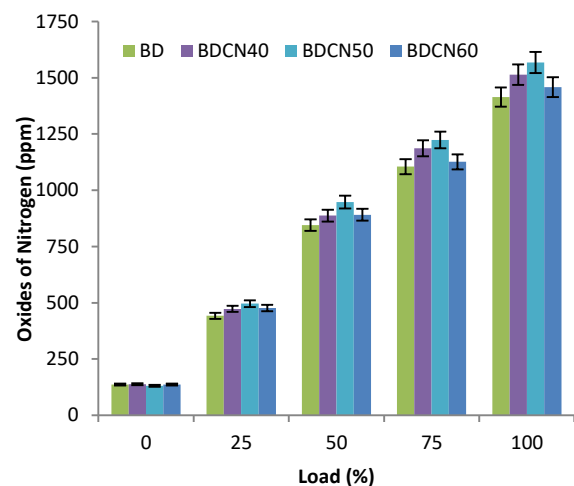


Figure 10. Oxides of Nitrogen Vs Load

The smoke opacity of the diesel engine with biodiesel and biodiesel added with different dosages of CNTs and at different loads is shown in the Figure 11. It is observed from the figure that the smoke emission increases with increase in load for all the fuels due to consumption of higher amount of fuel at higher loads. The CNT dosage impacts the smoke

emission. The BDCN60 results in higher smoke emission as compared to other CNT dosages at higher loads. The BDCN50 results in lower smoke emission due to improved heat transfer between the biodiesel particles due to higher surface area to volume ratio and higher chemical reactivity which increases molecule breakup during injection and ignition characteristics of the fuel (Gad&Jayaraj, 2020). The improved biodiesel oxidation and quick flame propagation reduces the engine smoke (Prabu et al., 2018). The higher dosage of CNT, BDCN60, results in higher smoke opacity and similar type of results were reported in literature (Ahmed et al 2016, Paramashivaiah et al 2018, SadhikBasha et al 2011)

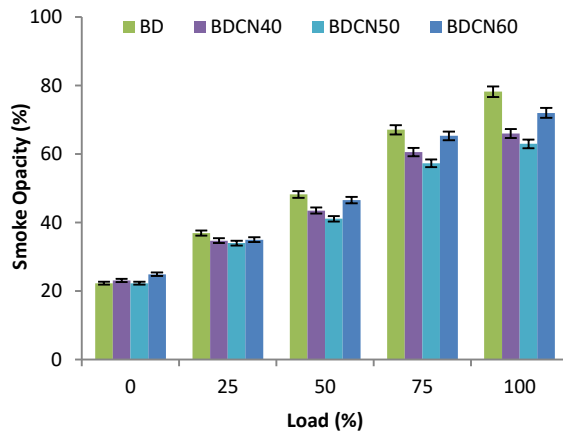


Figure 11. Smoke Opacity Vs Load

Conclusion

In this work, biodiesel was produced from non-edible pongamia oil using a two-step transesterification method. The pongamia oil biodiesel has lower volatility and slightly viscous and hence CNTs were added to the biodiesel. From the property analysis, it was observed that the addition of CNTs to the pongamia oil biodiesel improves the fuel properties of the biodiesel such as flash point and calorific value. The engine tests were carried out with biodiesel and biodiesel added with different dosage of CNTs. The CNTs dosage of 50 mg/l results in higher thermal efficiency and lower smoke, hydrocarbon and carbon monoxide emissions. The compression ignition engine emits higher hydrocarbon, carbon monoxide and smoke emissions at higher loads and the addition of CNT reduces these emissions significantly. However, these emissions were lower at lower loads. The cost of the biodiesel may be increased due to the addition of CNTs, however the reduction in hydrocarbon, carbon monoxide and smoke emission is significant. From this work, it is concluded that the CNTs can be added with the pongamia oil biodiesel to improve its properties and to enhance the performance of the diesel engine.

Acknowledgment

Authors thank Dr. Arun M Isloor of NITK, Surathkal for his help in providing CNTs and his help in ultrasonication.

References

[1] Ahmed I. EL-Seesy, Ali K. Abdel-Rahman, Mahmoud Bady, S. Ookawara, The Influence of Multi-Walled Carbon Nanotubes Additives into Non-Edible Biodiesel-Diesel Fuel

Blend on Diesel Engine Performance and Emissions, Energy Procedia, vol 100, (2016) 166 – 172.

[2] Ahmed I. El-Seesy, Hamdy Hassan, S. Ookawara, Effects of graphene nanoplatelet addition to jatropha Biodiesel–Diesel mixture on the performance and emission characteristics of a diesel engine, Energy, vol147 (2018) 1129-1152.

[3] Ahmet Uyumaz, Bilal Aydoğan, Emre Yılmaz, HamitSolmaz, FatihAksoy, İbrahim Mutlu, Duygüİpci, AlperCalam, Experimental investigation on the combustion, performance and exhaust emission characteristics of poppy oil biodiesel-diesel dual fuel combustion in a CI engine, Fuel, vol 280, 118588, (2020) 1-10.

[4] Ajay V. Kolhe, R.E.Shelke and S.S.Khandare, Performance and Combustion Characteristics of a DI Diesel Engine Fueled with Jatropha Methyl Esters and its Blends, Jordan Journal of Mechanical and Industrial Engineering, vol 8, no 1,(2014) 7-12.

[5] Al-Hassan. M, Mujafet H., Al-Shannag. M, An Experimental Study on the Solubility of a Diesel-Ethanol Blend and on the Performance of a Diesel Engine Fueled with DieselBiodiesel - Ethanol Blends, Jordan Journal of Mechanical and Industrial Engineering, vol 6, no 2, (2012)

[6] Álvaro Muelas, Pilar Remacha, Javier Ballester, Droplet combustion and sooting characteristics of UCO biodiesel, heating oil and their mixtures under realistic conditions, Combustion and Flame, vol 203, (2019) 190–203.

[7] AninditaChakrabarti, Ravinder Kumar Arora, India's Energy Security: Critical Considerations, Global Business Review, vol17, issue 6, (2016) 1–17.

[8] BalajiGnanasikamani, Effect of CNT as additive with biodiesel on the performance and emission characteristics of a DI diesel engine, International Journal of ChemTech Research, vol7, no.3, (2015) 1230-1236.

[9] Brandão, L. F. P., Suarez, P. A. Z. Study of Kinematic Viscosity, Volatility and Ignition Quality Properties of Butanol/Diesel Blends, Brazilian Journal of Chemical Engineering, vol 35, no. 4, (2018) 1405 – 1414.

[10] Dong, V.H., Le, Q.T., Physical Properties and Spray Characteristics of Ultrasound-assisted Emulsion based on Ultra Low Sulphur Diesel and Biodiesel. International Journal of Technology. vol 10, issue 2, (2019) 247-257.

[11] Hoseini, S.S., G. Najafi, B. Ghobadian, R. Mamat, TalalYusaf, Novel environmentally friendly fuel: The effects of nanographene oxide additives on the performance and emission characteristics of diesel engines fuelled with Ailanthus altissima biodiesel, Renewable Energy, vol 125, (2018) 283-294.

[12] https://gain.fas.usda.gov/Recent%20GAIN%20Publications/Biofuels%20Annual_New%20Delhi_India_6-27-2017.pdf (browsed on 21-3-2020)

[13] https://gain.fas.usda.gov/Recent%20GAIN%20Publications/Biofuels%20Annual_New%20Delhi_India_6-24-2016.pdf (browsed on 21-3-2020)

[14] https://mnre.gov.in/file-manager/UserFiles/biofuel_policy.pdf (browsed on 21-3-2020)

[15] [https://www.eia.gov/outlooks/ieo/pdf/0484\(2017\).pdf](https://www.eia.gov/outlooks/ieo/pdf/0484(2017).pdf) (browsed on 21-3-2020)

[16] Gad, M.S, Jayaraj, S. A comparative study on the effect of nano-additives on the performance and emissions of a diesel engine run on Jatropha biodiesel, Fuel, vol 267, 117168 (2020), 1-9.

[17] GeeteshGog, BhupendraSingh Chauhan, SunilKumar Mahla, HaengMuk Cho, AmitDhir, HeeChang Lim, Properties and characteristics of various materials used as biofuels: A review, Materials Today: Proceedings, Volume 5, Issue 14, Part 2, (2018) 28438-28445.

[18] GeeteshGoga, hupendra Singh Chauhan, Sunil Kumar Mahla, HaengMuk Cho, Performance and emission characteristics of

- diesel engine fueled with rice bran biodiesel and n-butanol, *Energy Reports*, vol 5, (2019) 78–83.
- [19] Geetesh Goga, Bhupendra Singh Chauhan, Sunil Kumar Mahla, Amit Dhir, Haeng Muk Cho, Effect of varying biogas mass flow rate on performance and emission characteristics of a diesel engine fuelled with blends of n-butanol and diesel, *Journal of Thermal Analysis and Calorimetry* (2020) 140:2831.
- [20] GeeteshGoga, Bhupendra Singh Chauhan, Sunil Kumar Mahla, Amit Dhir &HaengMuk Cho, Combined impact of varying biogas mass flow rate and rice bran methyl esters blended with diesel on a dual-fuel engine, *Energy Sources, Part A: Recovery, Utilization, and Environmental Effects* Vol 43, Issue 1, (2021).
- [21] Ghasemian S, Farizad A, Abbaszadeh P, Taklif A, Ghasemi A, Hafezi R, An overview of global energy scenarios by 2040: identifying the driving forces using cross-impact analysis method, *International Journal of Environmental Science and Technology*, 2020.
- [22] Harish Venu, PrabhuAppavu, Al₂O₃nano additives blended Polanga biodiesel as a potential alternative fuel for existing unmodified DI diesel engine, *Fuel*, 279 (2020) 118518
- [23] Ibrahim, H., Silitonga, A.S., Rahmawaty, Dharna, S., Sebayang, A.H., Khairil.,Sumartono, Sutrisno, J., Razak, A., An Ultrasound Assisted Transesterification to Optimize Biodiesel Production from Rice Bran Oil. *International Journal of Technology*. vol 11, issue 2, (2020) 225-234.
- [24] Josiah Pelelo, OmojolaAwogbemi, Freddie Inambao, Emmanuel I. Onuh, In-situ Hybridization of Waste Palm Oil: A Physicochemical, Thermal, and Spectroscopic analysis, *Jordan Journal of Mechanical and Industrial Engineering*, vol 14, no 4, (2020)
- [25] Man, X.J., Cheung, C.S., Ning, Z., Wei, L., Huang, Z.H., Influence of engine load and speed on regulated and unregulated emissions of a diesel engine fueled with diesel fuel blended with waste cooking oil biodiesel, *Fuel*, vol 180, (2016) 41–49.
- [26] Norhafana, M., Noor, M.M., Pshtiwan, M., Sharif, Hagos, F.Y., Hairuddin, A.A., Kadrigama, K., Ramasamy, D., Rahman,M.M., Alenezi,R. Hoang, A.T., A review of the performance and emissions of nano additives in diesel fuelled compression ignition-engines, *IOP Conf. Series: Materials Science and Engineering*, vol 469, paper id 012035, 2019.
- [27] Kapilan, N., Chandra Sekar, Production and evaluation of storage stability of honge biodiesel, *International Journal of Engineering*, vol IX, no3, (2011) 267-269.
- [28] Kapilan, N.; Birdar, Chandra Sekar, Effect of Antioxidants on the Oxidative Stability of Biodiesel Produced from Honge Oil , *Journal of Sustainable Energy Engineering* , vol 2, issue 1 , (2014) 52-56.
- [29] Mohanan, P., Kapilan, N., and Reddy, R., Effect of Diethyl Ether on the Performance and Emission of a 4 - S Di Diesel Engine," *SAE Technical Paper* 2003-01-0760, 2003.
- [30] Nikhil Sharma, William D. Bachalo, Avinash Kumar Agarwal, Spray droplet size distribution and dropletvelocity measurements in a firing optical engine, *Physics of Fluids*, vol 32, 023304, (2020) 1-18.
- [31] Noel, D, Venkata Ramesh Mamilla, Y. Bharat Kumar, V. Trinath,Performance on CI Engine Fuelled Honge Biodiesel Blended with Diesel, *Materials Today: Proceedings*, vol3, no 10, Part B, (2016) 3626-3631.
- [32] Pankaj Mohan Rastogi, Abhishek Sharma, Naveen Kumar, Effect of CuO nanoparticles concentration on the performance and emission characteristics of the diesel engine running on jojoba (*SimmondsiaChinensis*) biodiesel, *Fuel* 286 (2021) 119358.
- [33] Paramashivaiah, B. M., Banapurmath, N. R., Rajashekhar, C. R., Khandal, S. V., Studies on Effect of Graphene Nanoparticles Addition in Different Levels with Simarouba Biodiesel and Diesel Blends on Performance, Combustion and Emission Characteristics of CI Engine, *Arabian Journal for Science and Engineering* (2018) 43:4793–4801
- [34] Paweł Krause, RóbertLabuda, The Influence of Liquid Viscosity on Atomized Fuel Mean Droplet Size Determined By The Laser Diffraction Method, *New Trends in Production Engineering*, vol 1(10), (2018) 435-441.
- [35] Prabu, A., Nanoparticles as additive in biodiesel on the working characteristics of a DI diesel engine, *Ain Shams Engineering Journal*, vol9, (2018) 2343–2349.
- [36] SadhikBasha, J., Anand, R.B., An experimental investigation in a diesel engine using carbon nanotubes blended water-diesel emulsion fuel, *Proceedings of the Institution of Mechanical Engineers, Part A: Journal of Power and Energy*, volume 225, (2011) 279-288.
- [37] Sameh Nada, Ali M. Attia, M. S. Gad, Effect of Castor Biodiesel on Diesel Engine Performance, Emissions, and Combustion Characteristics, *Jordan Journal of Mechanical and Industrial Engineering*, vol 12, number 4, (2018) 261–268.
- [38] Seyyed Hassan Hosseini, Ahmad TaghizadehAlisaraei, Barat Ghobadian, Ahmad AbbaszadehMayvan, Effect of added alumina as nano-catalyst to diesel-biodiesel blends on performance and emission characteristics of CI engine, *Energy*, vol 124, (2017) 543-552.
- [39] Seyyed Hassan Hosseini, Ahmad Taghizadeh-Alisaraei, Barat Ghobadian, Ahmad Abbaszadeh-Mayvan, Performance and emission characteristics of a CI engine fuelled with carbon nanotubes and diesel-biodiesel blends, *Renewable Energy*, vol 111, (2017) 201-213.
- [40] TizaneDaho, Gilles Vaitilingom, Salifou K. Ouiminga, Bruno Piriou, Augustin S. Zongo, Samuel Ouoba, Jean Kouliadiati, Influence of engine load and fuel droplet size on performanceof a CI engine fueled with cottonseed oil and its blends with diesel fuel, *Applied Energy*, 111, (2013) 1046–1053.
- [41] Vivek W Khond, Kriplani V M, Effect of nanofluid additives on performances and emissions of emulsified diesel and biodiesel fueled stationary CI engine: A comprehensive review, *Renewable and Sustainable Energy Reviews*, vol 59, (2016) 1338–1348.
- [42] Zahra Fathi, Ramazan-Ali Khavari Nejad, HomaMahmoodzadeh, TaherNejadSatari, Investigating of a wide range of concentrations of multi-walled carbon nanotubes on germination and growth of castor seeds (*Ricinus communis L.*), *Journal of Plant Protection Research*, vol 57, no 3,(2017) 1-9.

Effect of Gable Roof Angle on Natural Ventilation for an Isolated Building

Lip Kean Moey^{a,*}, Man Fai Kong^b, Vin Cent Tai^a, Tze Fong Go^c, Nor Mariah Adam^d

^aCentre for Modelling and Simulation, Faculty of Engineering, Built Environment & Information Technology, SEGi University, Selangor, Malaysia

^bFaculty of Engineering, Built Environment & Information Technology, SEGi University, Selangor, Malaysia

^cCentre for Advance Materials and Intelligent Manufacturing, Faculty of Engineering, Built Environment & Information Technology, SEGi University, Selangor, Malaysia

^dDepartment of Basic Science and Engineering, University Putra Malaysia Bintulu Sarawak Campus, Sarawak, Malaysia

Received August 21 2020

Accepted June 30 2021

Abstract

Airflow characteristics around and within an isolated gable roof building were investigated using computational fluid dynamic with steady RANS equations. This study focuses on the following parameters: streamline of normalized velocity, pressure coefficient, and normalized turbulent kinetic energy. Three different roof pitches of the gable roof namely 15°, 25°, and 35° were considered. The streamline shows that an increase in roof pitch results in a corresponding increase of velocity at the window openings. Meanwhile, the streamline velocity at the roof opening varies across different roof angles. On the other hand, the pressure coefficient at the windward side and interior of the building decreases as the roof pitch becomes steeper. Variation in the flow fields of 25° and 35° roof pitch with window and roof opening, is relatively more apparent as compared to that of a 15° and 25° roof pitch. The turbulent kinetic energy at the leeward side of the building also becomes larger with the increase in roof pitch. Therefore, airflow behavior and characteristics are significantly dependent on the roof pitch which shows good agreement with the literatures. A higher roof pitch of gable roof building is, therefore, preferred for better ventilation rate.

© 2021 Jordan Journal of Mechanical and Industrial Engineering. All rights reserved

Keywords: Natural Ventilation, Gable Roof, CFD, Roof Pitch, Steady RANS, Ventilation Rate;

1. Introduction

Malaysia as a tropical country is exposed to long-term solar heat attacks, global warming, and greenhouse effects. The Earth surface temperature has risen by 1°C over the past century[1], and is predicted to further rise over a range of 3.7°C to 4.8°C in the coming century[2]. In tropical countries, this rise of surface temperature has led to a sharp increase of energy consumption over the past decade. According to the Malaysian Energy Information Hub (MEIH), residential energy consumption has increased from 22.53-Terawatt hour (TWh) to a highest record of 31.16 TWh between the years of 2010 to 2017[3]. Renewable energy sources such as wind can offer important environmental, social and economic benefits[4,5].

Ventilation is a process that aids in improving indoor air quality and comfort by introducing cool and fresh air from a clean source into the building, while expelling existing hot and polluted air [6,7]. Ventilation also helps to optimize the indoor thermal environment, prevents excessive moisture development, and repels pollutants, such as pollens, dust, and contaminants in the air[8]. Excessive moisture build-ups especially in tropical countries may lead to allergies, respiratory diseases, besides the hygiene problems in environments that encourage molds and mites to thrive.

Heat accumulation may also occur at roof and attic areas without the aid of ventilation. Thus, Heating, Ventilating and Air Conditioning (HVAC) systems are normally introduced to improve indoor air quality, comfort, and thermal environment. However, HVAC accounts up to 60% of domestic building energy consumption[7].

Natural ventilation utilizes natural phenomena such as wind force and the stack effect to introduce fresh air into an interior space and repel aged air to the outside. It is believed to be the most effective and environmentally friendly method of passive cooling for supply clean and fresh air to a space[8,9]. Natural ventilation with proper roof design is feasible for tropical countries such as Malaysia whereby local air conditions are classified as Class I, with annual wind velocities averaging between 1 m/s to 5 m/s[7]. Natural ventilation can be further categorized into cross ventilation and stack ventilation. Cross ventilation is driven by wind flow, thereby generating negative pressure indoors which in turn creates a pressure difference that directs the wind flow from outside into the building through apertures[7,10–12]. On the other hand, stack ventilation is driven by temperature discrepancies between the indoors and the outdoors of a building[8,13,14]. Due to the imperceptible indoor and outdoor temperature changes in tropical regions, cross ventilation is said to be more effective and therefore, the stack ventilation effect is not

* Corresponding author e-mail: moeylipkean@segi.edu.my.

included in the scope of this study[14]. Cross ventilation shall be the main focus of this investigation.

The roof plays an important role in preventing humidity development and heat accumulation in a building[15]. Roof configuration greatly impacts wind flow pattern and characteristics around and within a building and also controls the dispersion of pollutants[14–16]. Some common roof configurations in Malaysia are the hip, venturi, and gable types.

Computational Fluid Dynamics (CFD) is an authoritative tool that combines flow physics, computer application, mathematics, and the knowledge of mechanics to solve problems involving one or more phenomena such as fluid flow, heat change, mass transfer, and chemical reaction[17,18]. CFD was applied to study the airflow around a gable roof building with various roof tilt angles by measuring the turbulent kinetic energy, pressure coefficient, and time-averaged velocity around the gable roof building[19,20]. Reynolds-Averaged Navier-Stokes(RANS) models, such as the Standard $k-\epsilon$ (Sk- ϵ), Renormalization Group $k-\epsilon$ (RNG $k-\epsilon$), Realizable $k-\epsilon$ (RK- ϵ), and Shear-Stress Transformation $k-\omega$ (SST $k-\omega$) models were tested and validated against the wind tunnel experiment. These studies confirmed that roof pitches affect the streamline, distribution of turbulent kinetic energy, pressure coefficient, and mean velocity ratio of wind around the building.

Only a few literatures have comprehensively examined the impact of gable roof configuration on natural ventilation. Karava et al. analyzed the wind-induced natural ventilation on a 1:12 sloped gable roof building using the boundary layer wind tunnel experiment[6]. The tested building model has a 153mm \times 98mm rectangular plan view with 30mm in eave height. This experiment was conducted on a gable roof building with windward wall porosity ranging from 0 to 22%. Results indicate that the internal pressure coefficient and discharge coefficient of a cross-ventilated building varies significantly with wall porosity and inlet to outlet ratio. Non-uniformity of the internal pressure coefficient for windward wall porosity larger than 10% was only observed in a cross-ventilated building. The airflow rates changed considerably when different discharge coefficients are used, specifically for configurations with large inlet to outlet ratios.

Peren et al. investigated the impact of roof angle and opening locations on cross ventilation of a generic isolated building with asymmetric opening positions[21]. The analysis was conducted with 3D RANS CFD simulation using six turbulence models and five different roof angle inclinations. Accuracy of the SST $k-\omega$ model was validated against the Particle Image Velocimetry (PIV) experiment by Karava et al.[22]. Results indicate that the volume flow rate and indoor air flow pattern are highly dependent on the roof inclination angles. Critical roof inclination angle shall be larger than 18° to improve the volume flow rate of a low-rise building.

In reality, volume flow rate, pressure difference over a building, and indoor air speed rely strongly on roof shapes and configurations[22]. However, limited literatures focus on the effect of roof configuration on indoor natural ventilation. As such, the impact of a gable roof building on indoor airflow pattern has yet to be well studied specifically in buildings with window openings. Therefore, this study is

dedicated to investigate the effect of gable roof angles on natural cross ventilation in an isolated building with window openings. The CFD simulation results generated are then validated against experimental and numerical analysis performed by Karava et al.[22]and Tominaga et al.[23],respectively.

The remaining of the paper is organized as follows: Section 2 outlines the computational setting and parameters, perform model validation, and grid sensitivity studies. Section 3 presents the simulation results of gable roof building with various roof pitches and discusses the effect of varied gable roof angles on airflow characteristics. Finally, section 4 concludes the findings of this study.

2. Numerical Studies: Model Setup and CFD Simulation

2.1. Model Cases

In this study, an isolated basic building model is chosen as the reference model. The model has a 1:50 scaled down dimension of length \times width \times height (L \times W \times H) = 100mm \times 100mm \times 80mm, corresponding to 5m \times 5m \times 4m in real scale. This model also constitutes of a set of window and roof openings each at two opposing side walls, having heights of 18 mm and 9 mm respectively with center line of the window opening at $y = 0.04$ m, and that of the roof opening at $y=0.0655$ m from ground level. Wall thickness of the tested model is 2 mm as proposed by Ramponi et al.[14]. This basic model was used as a basis for grid sensitivity study in which its results were validated by the PIV experiment by Karava et al.[22].Three model cases were constructed based on this basic building model using different roof pitches. Another reference model with a gable roof but without window openings was also created with reference to Tominaga et al.[23]for validation purposes.

2.2. Computational Domain and Grids

Simulations were performed using a scaled down model which was modified based on the basic building model. The computational domain was created with reference to existing recommended operational guidelines proposed by Franke et al.[24]and Tominaga et al.[25]. However, distance between the inlet plane of the computational domain and windward wall of the tested model was reduced to 3H at upstream instead of 5H as recommended by Franke et al.[24]and Tominaga et al.[25] to restrict the extent of unplanned streamwise gradient[14]. The top and lateral wall of the flow domain were set 5H away from the model, while the downstream length was set to 15H. Figures 1(a) and 1(b) illustrate the dimensions of a gable roof building with roof angle of 15° and the computational domain, respectively, whereby H is the effective building height measured from ground level.

MosaicTM meshing technology was applied to this geometry due to its ability to produce high quality octree hexahedron in the bulk region. The MosaicTM meshing technology allows automatic connection of elements regardless of their types. It also produces high quality meshes and is efficient in solving fluid flow around highly complex geometries[26]. This geometry was first meshed with a tetrahedral element using the scope sizing function in

Ansys Fluent, followed by its conversion into a poly-hexcore. Figure 2 shows the meshing details of the tested models and the flow domain.

2.3. Boundary Conditions

The measured mean wind speed and turbulence intensity from the vertical plan determines the boundary conditions to be imposed at the inlet plane of the flow domain. Inlet wind velocity was determined using equation (1), whereby $z_0=0.00003m$, von Karman constant $\kappa = 0.42$, z is the height coordinate, and U_{abl} is friction velocity of the atmospheric boundary layer. Turbulent kinetic energy (TKE), k can then be calculated using equation (2), knowing the mean wind velocity and measured turbulence intensity, I_u . The chosen α value shall be 1 as recommended by Tominaga et al.[23].The turbulence dissipation rate, ε and specific dissipation rate, ω can be determined using equations (3) and (4) respectively whereby C_{μ} is an empirical constant equal to 0.09 [27].

$$U(z) = \frac{u_{ABL}^*}{\kappa} \ln\left(\frac{z + z_0}{z_0}\right) \tag{1}$$

$$k(z) = \alpha (I_u(z)U(z))^2 \tag{2}$$

$$\varepsilon(z) = \left(\frac{u_{ABL}^{*3}}{\kappa(z + z_0)}\right) \tag{3}$$

$$\omega(z) = \frac{\varepsilon(z)}{C_{\mu}k(z)} \tag{4}$$

Standard wall function with roughness height modification was applied at ground surface[28,29] as this building is expected to be built on a grass covered terrain

with a scaled down roughness length of 0.00003m. The sand grain roughness k_s was determined using equation (5) derived by Blocken et al.[30]which describes the consistency of relationship between k_s and the roughness constant C_s , whereby the chosen value for C_s is 0.42.

$$k_s = \frac{9.793z_0}{C_s} \tag{5}$$

Zero static pressure was imposed at the outlet plane, and symmetry type was applied to the symmetry plane. Boundary condition at the top and lateral side wall of the flow domain on the other hand were imposed with zero normal gradients and velocities representing the zero-shear condition. Standard wall function with zero roughness height was also applied to the tested model.

2.4. Solver Settings

In this study, simulations were performed using Ansys 2019 R3. The 3D steady RANS equation was solved by theSST $k-\omega$ turbulence model. The SST $k-\omega$ model was selected as it has better accuracy in comparison to the PIV experiment conducted by Karava et al.[22]. This study also uses the SIMPLE algorithm which was established from the Green Gauss node based spatial discretization in combination with second-order upwind discretization schemes and pressure interpolation applied to the convection and viscous terms of the governing equation. Convergence was expected to be achieved when the scaled residuals are receding down to 10^{-4} . Table 1 summarizes the details and comparison of parameters between previous literatures.

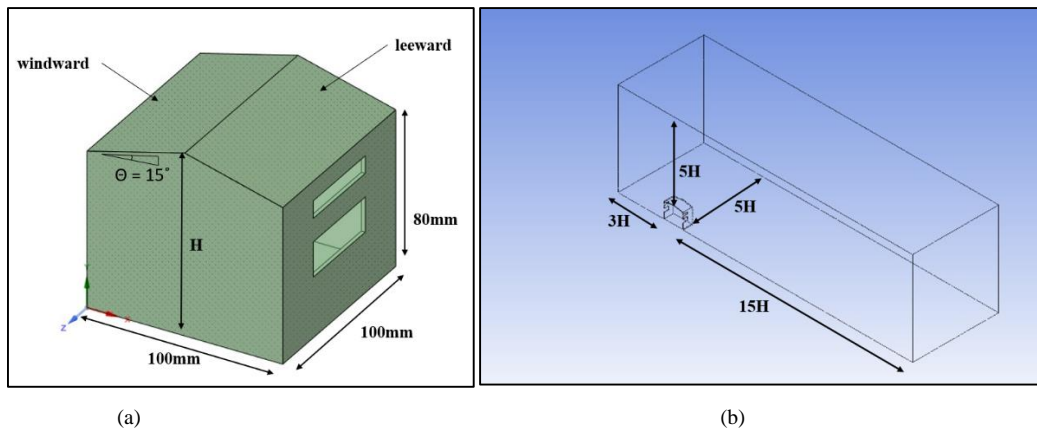


Figure 1. Dimension of (a)15° gableroof building and (b) computational domain

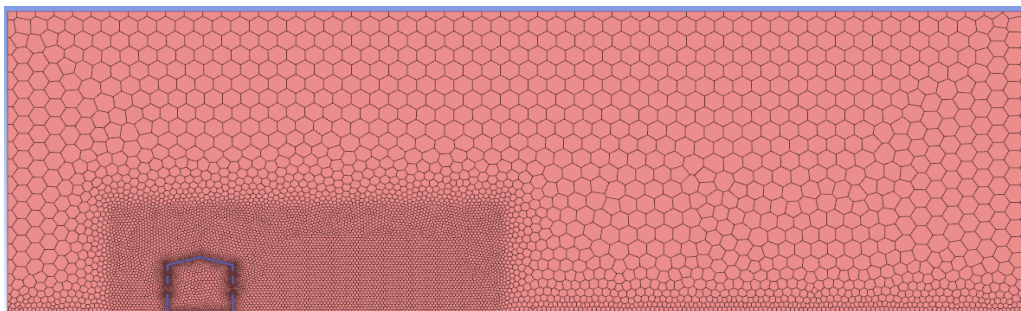


Figure 2. Meshing details of flow domain of 15° roof pitch

2.5. Grid Sensitivity Analysis

A grid sensitivity analysis was performed on the basic building model to ensure that the results are grid independent. Three different grids with various cell counts (319426, 473837 and 749997) were created for the purpose of this analysis. Grids with higher cell counts have smaller mesh sizes. Results of these meshes were compared with the PIV results by Karava et al. [22] in terms of dimensionless mean velocity ratio (U/U_{ref}) across the inlet and outlet aperture. Note that U is the 3D streamwise velocity vector and $U_{ref} = 6.97\text{m/s}$ is the reference wind speed measured at the building height ($H=80\text{mm}$).

Figure 3 illustrates the results obtained from three different grid sizing and the PIV results by Karava et al. [22]. Each coarse, basic and fine mesh (denoted by grid A, B and C) has respective cell counts of 319426, 473837, and 749997. Results were compared in terms of dimensionless mean velocity ratio U/U_{ref} . Observations clearly show that the fine mesh model conforms most closely to the experimental results with the nearest cell counts as compared to the literatures in Table 1. The fine mesh is, therefore, implemented in the subsequent simulations and studies. To effectively capture the boundary layer around the building walls, 10 prism layers with the 1st cell height of 0.01mm (corresponding to $y^+ \approx 200$) and an inflation rate of 1.2 were added to the mesh. Noticeable difference between the numerical and experimental results can be observed near the openings. This is attributed to the fact that numerical models tend to overestimate the mean wind speed near the openings [10]. Also, shading effects and reflections may contribute to inaccurate prediction of the PIV measurements [6].

2.6. Model Validation

Both the wind-tunnel experiment and CFD simulation conducted by Tominaga et al. [23] were used for model validation. The test model was created without any window and roof opening for this validation purpose. Mean velocity ratio around the simulated models were then compared to that of the wind tunnel measurements and computational results by Tominaga et al. [23].

The model was validated with respect to the reference model by Tominaga et al. [23] in terms of streamlines and pressure coefficient. Figures 4 and 5 compare the streamline and distribution of pressure coefficient between the validation model and that of the reference model. Results show a large recirculation region behind the building and a small recirculation region at the lower corner windward side of the building. Positive pressure is also observed in front of the validation model due to the blockage caused by the building structure. Negative peaks at the front corner of the validation model were also apparent in both results. Further detailed inspection of Figure 4 revealed a wake behind the validation model that is larger than that of the reference model. This is because the $k - \omega$ SST turbulence model was used for validation while the RNG $k - \epsilon$ model was used as reference. Both RANS models perform differently in turbulence prediction [23]. Although significant improvement on prediction accuracy can be achieved by systematically optimizing the closure coefficients of the RANS models [32], the work is beyond the scope of this study. This validation model is therefore practiced and modified accordingly in the following investigations.

Table 1. Summary of literature reviews on roof configurations

Literature	Roof Shape	Roof Pitches (°)	Turbulence Model	Mesh Type	Selected Cell Counts
Tominaga et al., 2015 [23]	Gable	16.7, 26.6, 36.9	Sk- ϵ , RNG k- ϵ , Rk- ϵ , SST k- ω	Structured	2355280
Ozmen et al., 2016 [31]	Gable	15, 30, 45	Rk- ϵ , Sk- ω	Structured	800000
Peren et al., 2015 [21]	Inclination	9, 18, 27, 36, 45	SST k- ω	Structured	770540
Karava et al., 2007 [6]	Gable	5	-	-	-

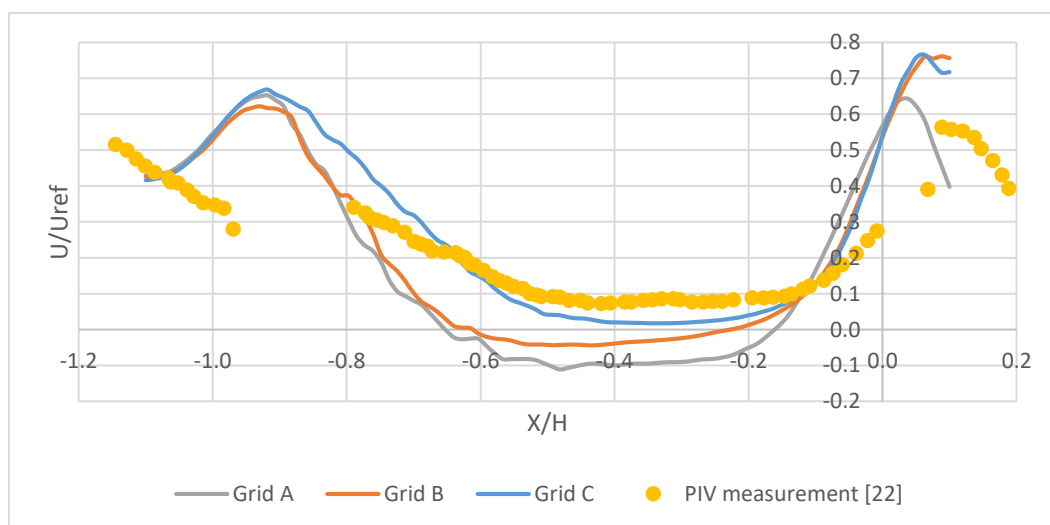


Figure 3. Comparison between simulation results of three different grid sizing and PIV experimental results by Karava et al. [22]

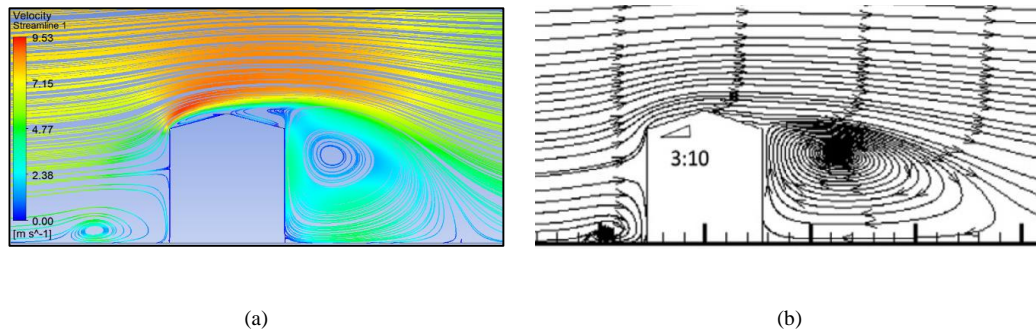


Figure 4. Comparison of streamline velocity between (a) validation model of 15° roof pitch and (b) reference model of 16.6° [23].

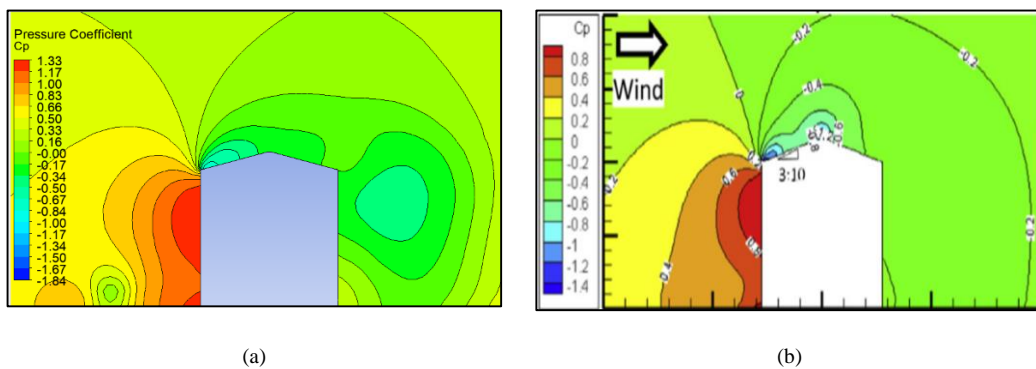


Figure 5. Comparison of pressure coefficient contour of (a) validation model of 15° roof pitch and (b) reference model [23].

3. Results and Discussion

3.1. Streamlines

Figure 6 compares the streamlines of normalized velocity for various roof pitches. According to Tominaga et al.[23], the recirculation region at the leeward side of the building becomes larger as roof angle increases. The center region of the recirculation eddy behind the building also tends to move upwards. However, addition of window and roof openings, and shelling of the model allowed wind to flow through the building thereby interrupting the recirculation flow behind the model. It can be clearly observed that there is a noticeable change in flow field between roof pitches of 15° and 25°. Although no reverse flow is observed behind the building for roof pitch of 15°, but reverse flow is present, and it becomes larger in roof pitches of 25° and 35°. Velocity through the openings are also observed to be increasing as the roof angle becomes steeper. The resulting critical roof pitch is nearly compatible with the critical roof pitch of 18° at which flow around the gable roof building changes, and the reversed flow at the leeward side of the roof becomes larger. Overall streamline results are in well agreement with the findings by Tominaga et al.[23].

3.2. Spatial Distribution of Pressure Coefficient

Figure 7 presents a comparison of the static pressure around a building with various gable roof angles. In all cases, peak positive value of pressure coefficient is observed at the front of the building due to the impact of

wind force on the building wall. Negative peak value on the other hand is observed at the windward corner and the ridge side in the case of a 15° gable roof. Pressure coefficient also increases with increment in roof angle at the windward side. Contrastingly, no negative peak value of pressure coefficient is observed at the windward corner of the 25° and 35° roof pitches. However, the negative value nearing the leeward side of the roof becomes larger as the steepness of the roof pitch increases, and the wake formation region becomes larger with increment in the roof angle. Pressure within the building also decreases with an increase in the roof pitch.

3.3. Mean Velocity Profile

Figure 8 shows the inlet and outlet profiles of dimensionless streamwise mean velocity, U/U_{ref} at the windward window and roof openings (RO) of the tested model. Results clearly indicate that velocity at both window and roof openings increased with increasing roof pitch. A notable difference is observed between roof pitches of 25° and 35°. Constant changes are also observed in the streamwise mean velocity profile at the roof opening inlet when roof pitch is increased. Similarly, significant difference in velocity profile is observed at the window outlet between all three roof pitches whereby a prominent increase is observed between the 15° and 25° roof pitch, followed by an abrupt decrease in the case of the 35° roof pitch. The velocity profile has also changed noticeably. Results, therefore, indicate that dimensionless streamwise mean velocity is strongly dependant on the roof pitch.

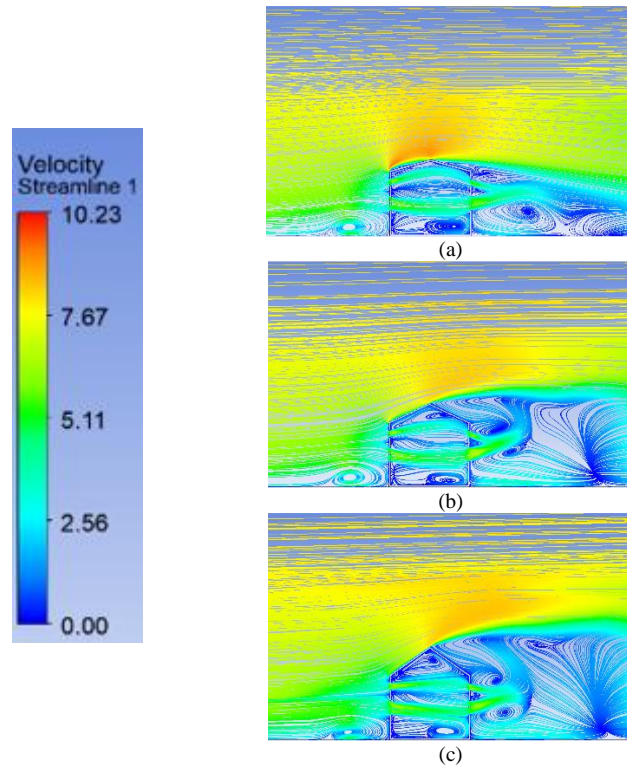


Figure 6. Streamlines of Normalized Velocity (U/U_{ref}) of (a)15° roof pitch, (b)25° roof pitch and (c)35° roof pitches

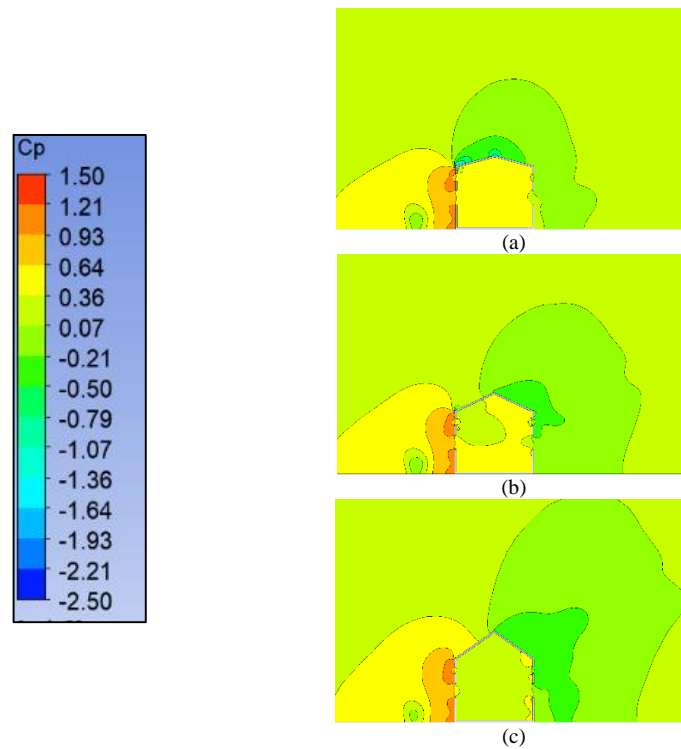
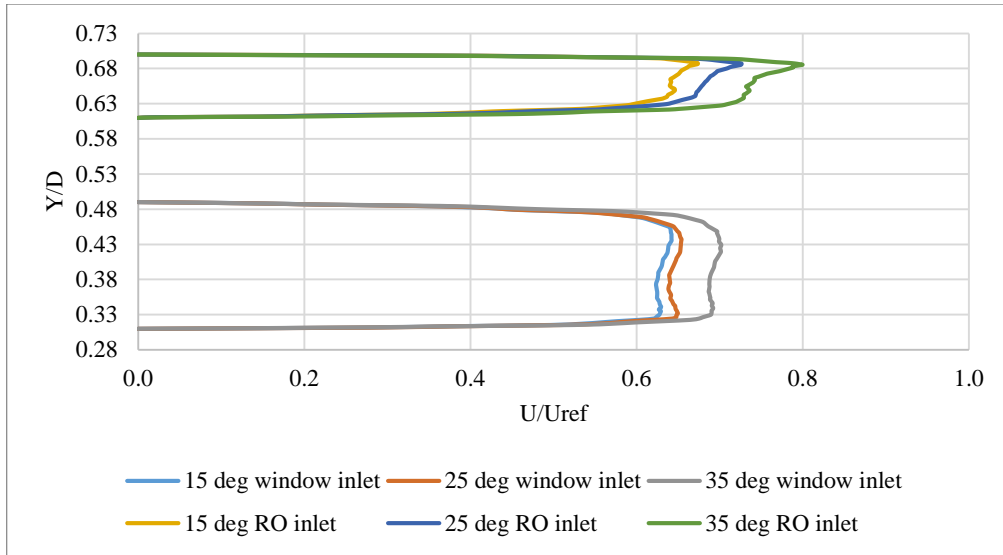
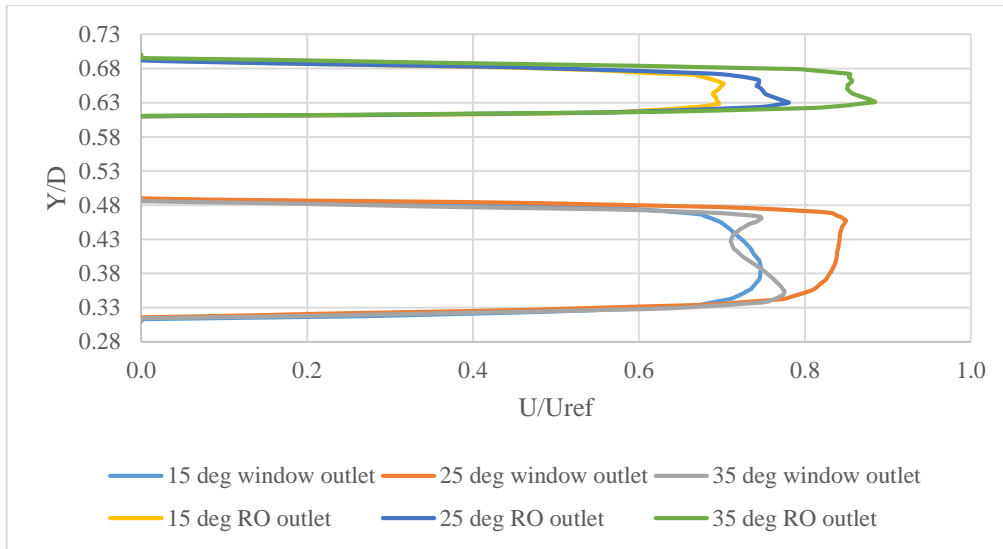


Figure 7. Spatial distribution of pressure coefficient of (a)15°, (b)25° and (c)35° roof pitches



(a)



(b)

Figure 8. Velocity profile at window and roof opening (a) inlet and (b) outlet

3.4. Distributions of Normalized Turbulent Kinetic Energy

Figure 9 illustrates the distribution contours of normalized turbulent kinetic energy (TKE), k for 15°, 25° and 35° roof pitches. In the case of a 15° roof pitch, region of distribution of TKE is observed to be small with no apparent peak value. However, the peak value of TKE is observed at the ridge in the case of 25° and 35° roof angles, with both peak value and region of TKE distribution becoming larger as the roof pitch becomes steeper. This is due to flow separation resulting from the increment in roof angle[23]. In contrast, changes in the distribution of TKE is minor within the building despite changes in the roof angle. The TKE distribution near the roof opening outlet on the other hand was observed to be larger as the roof pitch increased. This TKE distribution shows the airflow power near the building from ambient wind through the apertures, therefore accounting for the flow patterns near the building model which explains the sudden change of streamwise mean velocity profile at the window outlet for roof pitch of 35°[33].

3.5. Ventilation Rate

The air flow rate of a naturally ventilated building model can usually be determined by means of simple relationship. The rate of ventilation for a naturally cross ventilated low rise isolated building can be determined using the following equations[34]:

$$C_p = \frac{P - P_r}{\frac{1}{2} \rho V_{ref}^2} \tag{6}$$

$$CQ = C_d V_{ref} \sqrt{\Delta C_p} \tag{7}$$

$$C_a = \frac{CQ}{(1 + CQ)} \tag{8}$$

$$Q = C_a V_{ref} A_e \tag{9}$$

Equation (6) is used to determine the pressure coefficient, C_p , whereby P is the pressure at selected opening, P_r is the reference free stream static pressure, $\rho = 1.225 \text{ kg/m}^3$ is the density of air, and $V_{ref} = 6.97 \text{ m/s}$ is the measured velocity at reference height. The pressure coefficient calculated from inlet and outlet openings will then be used in equation (7) to calculate the estimated flow coefficient, C_Q , whereby $C_d = 0.62$ is the discharge coefficient and ΔC_p is the pressure coefficient change between inlet and outlet opening. Accordingly, ventilation rate can be calculated by equation (9) which is derived from the Bernoulli equation namely the product of actual flow coefficient: C_a , V_{ref} , and the effective area of opening: A_e . In this present study, the effective area (A_e) was determined to be $1.242 \times 10^{-3} \text{ m}^2$, whereby the corresponding discharge coefficient can be reasonably assumed to be 0.62 - a typical value for a sharp openings.

Figure 10 compares the ventilation rates between the three different roof pitches. Data clearly indicate that ventilation rate increases with the increase in roof pitch. A larger difference is observed in the ventilation rate between 15° and 25° roof angle and the increment of ventilation rate decedes when the roof angle increased to 35° from 1.97% to 0.69%. This is caused by the pressure difference

between the interior and exterior of the building model. The pressure variation between indoors and outdoors causes the wind flow to enter the building at an increasing velocity through the opening apertures. This increment of wind speed entering the building with increasing roof pitch induces a higher rate of ventilation and eventually promotes improved indoor air quality and comfort.

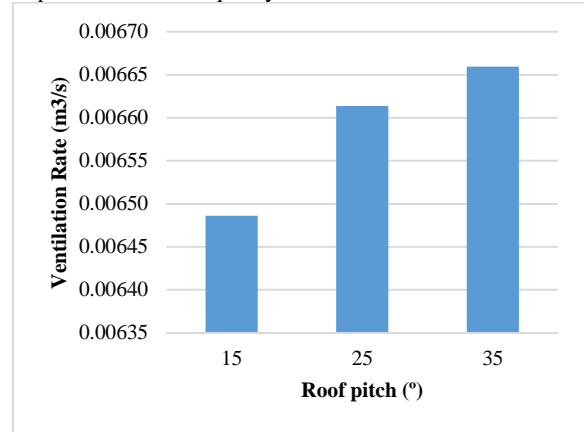


Figure 10. Comparison of ventilation rate (m^3/s) of gable roof with various angle.

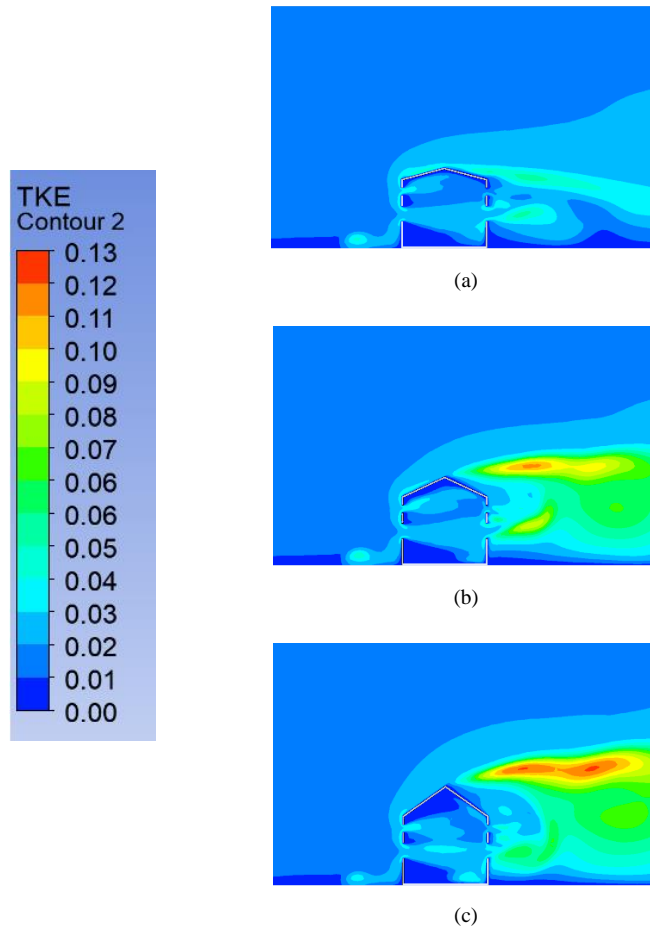


Figure 9. Distribution of normalized turbulent kinetic energy of (a) 15° , (b) 25° and (c) 35° roof pitch

4. Conclusion

In the present study, airflow characteristics around and within an isolated building with gable roof of varied roof angles namely 15°, 25°, and 35° were investigated and analyzed by the means of computational analysis and 3D RANS in steady state. Model validation was conducted and verified to be agreeable with the findings from literature. Computational simulation results also show that the streamline, pressure coefficient, TKE, mean velocity ratio, and ventilation rate are significantly dependent on the roof pitch. The recirculation region behind the building tends to move upwards and become larger with the increase in roof pitch angle. However, the presence of window and roof openings generates wind flow through the apertures thereby disturbing the recirculation region. Positive pressure was observed at the windward side of the building due to the wind blockage caused by the building wall. Negative peaks on the other hand occur at the windward corner and reduces until it eventually diminishes as the roof pitch is increased. Concurrently, the spatial distribution of TKE at the leeward side of the building roof becomes larger as the roof pitch is increased. Ventilation rate was also observed to increase with higher roof pitch. Based on all the above measured parameters, it can be concluded that gable roofs with a higher roof pitch is preferred for better natural ventilation in an isolated building. This study is, however, limited only to one reference wind speed: $U_{ref} = 6.97\text{m/s}$, and one wind direction namely that perpendicular to the windward side of the building. As ventilation performance could be affected by varying the reference wind speed and wind direction, these parameters may be further investigated in future research. Future work can also include the surrounding buildings to better understand the effect of real urban conditions on cross ventilation.

References

1. A.P. Aizebeokhai, "Global warming and climate change: Realities, uncertainties and measures". *International Journal of Physical Sciences*, Vol. 4, No.13, 2009, 868–879.
2. N.A. Hassan, Z. Hashim, J.H. Hashim, "Impact of climate change on air quality and public health in urban areas". *Asia-Pacific Journal of Public Health*, Vol. 28, No. 2, 2014, 38–48.
3. Suruhanjaya Tenaga. Malaysia energy statistics handbook 2019. Malaysia Suruhanjaya Tenaga (Energy Comm); 2019, p.1–86.
4. S. A. Ahmed, H. O. Mahammed, "A statistical analysis of wind power density based on the weibull and ralyeigh models of "Penjwen region" Sulaimani/Iraq". *Jordan Journal of Mechanical and Industrial Engineering*, Vol. 6, No. 2, 2012, 135-140.
5. H. Nidal, "Greenhouse gas emissions reduction potential of Jordan's utility scale wind and solar projects". *Jordan Journal of Mechanical and Industrial Engineering*, Vol. 10, No. 3, 2016, 199-203.
6. P. Karava, T. Stathopoulos, A.K. Athienitis, "Wind-induced natural ventilation analysis". *Solar Energy*, Vol. 81, No. 1, 2007, 20–30.
7. L.K. Moey, N.M. Adam, K.A. Ahmad, L.C. Abdullah, "Wind tunnel study of different roof geometry configurations for wind induced natural ventilation into stairwell in tropical climate". *International Journal of Engineering Research*, Vol. 13, No.5, 2018, 2635–47.
8. C.H. Lim, S. Omidreza, K. Sopian, M.Y. Sulaiman, S. Mat, E. Salleh, "Design configurations analysis of wind-induced natural ventilation tower in hot humid climate using computational fluid dynamics". *International Journal of Low-Carbon Technologies*, Vol. 10, No. 4, 2013, 332–346.
9. M. N. Khan, I. Janajreh, "Transevaporative cooling performance of a three-sided wind catcher". *Jordan Journal of Mechanical and Industrial Engineering*, Vol. 11, No. 4, 2017, 225-233.
10. R. Ramponi, B. Blocken, "CFD simulation of cross ventilation flow for different isolated building configurations: Validation with wind tunnel measurements and analysis of physical and numerical diffusion effects". *Journal of Wind Engineering and Industrial Aerodynamics*, Vol. 104-106, 2012, 408-418.
11. M. Shirzadi, P.A. Mirzaei, M. Naghashzadegan, "Development of an adaptive discharge coefficient to improve the accuracy of cross-ventilation airflow calculation in building energy simulation tools". *Building and Environment*, Vol.127, 2018, 277–290.
12. M. Shirzadi, M. Naghashzadegan, P.A. Mirzaei, "Improving the CFD modelling of cross-ventilation in highly-packed urban areas". *Sustainable Cities and Society*, Vol.37, No.Sieminski 2015, 2018, 451–65.
13. A. Aflaki, N. Mahyuddin, Z.A. Mahmoud, B. Mohamad Rizal, "A review on natural ventilation applications through building façade". *Energy and Buildings*, Vol.101, 2015, 153-162.
14. R. Ramponi, B. Blocken, "CFD simulation of cross-ventilation for a generic isolated building: Impact of computational parameters". *Building and Environment*, Vol. 53, 2012, 34–48.
15. J. Kindangen, G. Krauss, P. Depecker, "Effects of roof shapes on wind-induced air motion inside buildings". *Building and Environment*, Vol.32, No.1, 1997, 1–11.
16. L. K. Moey, N. M. Adam, K. A. Ahmad, "Effect of venturi-shaped roof angle on air change rate of a stairwell in tropical climate". *Journal of Mechanical Engineering*, Vol. 4, No. 4, 2017, 135-150.
17. Y. Huang, X. Hu, N. Zeng, "Impact of wedge-shaped roofs on airflow and pollutant dispersion inside urban street canyons". *Building and Environment*, Vol. 44, No.12, 2009, 2335–2347.
18. M.F. Yassin, "Impact of height and shape of building roof on air quality in urban street canyons". *Atmospheric Environment*, Vol. 45, No. 29, 2011, 5220–5229.
19. Y. Tominaga, B. Blocken, "Wind tunnel experiments on cross-ventilation flow of a generic building with contaminant dispersion in unsheltered and sheltered conditions". *Building and Environment*, Vol.92, 2015, 452–461.
20. R.K. Raman, Y. Dewang, J. Raghuvanshi, "A review on applications of computational fluid dynamics". *International Journal of Laskshmi Narain College of Technology*, Vol. 2, No. 6, 2018, 137–143.
21. J.I. Perén, T. vanHooff, B.C.C. Leite, B. Blocken, "CFD analysis of cross-ventilation of a generic isolated building with asymmetric opening positions: Impact of roof angle and opening location". *Building and Environment*, Vol. 85, 2015, 263–276.
22. P. Karava, T. Stathopoulos, A.K. Athienitis, "Airflow assessment in cross-ventilated buildings with operable façade elements". *Building and Environment*, Vol. 46, No.1, 2011, 266–279.
23. Y. Tominaga, S. Akabayashi, T. Kitahara, Y. Arinami, "Air flow around isolated gable-roof buildings with different roof pitches: Wind tunnel experiments and CFD simulations". *Building and Environment*, Vol. 84, 2015, 204–213.
24. Franke J, Hellsten A, Schlunzen H, Carissimo B. Best practice guideline for the CFD simulation of flows in the urban environment. 1st ed. Belgium: COST Action; 2007, p. 10–26

25. Y. Tominaga, A. Mochida, R. Yoshie, H. Kataoka, T. Nozu, M. Yoshikawa, "AIJ guidelines for practical applications of CFD to pedestrian wind environment around buildings". *Journal of Wind Engineering and Industrial Aerodynamics*, Vol. 96, 2008, 1749–1761.
26. Z. Krishna, P. Gandhar, S. Balasubramanyam, A. Varghese, "Ansys mosaic poly-hexcore mesh for high-lift aircraft configuration". 21 st Annual CFD Symposium, Bangalore, India, 2019,1–11.
27. M. Shirzadi, P.A. Mirzaei, M. Naghashzadegan, Y. Tominaga, "Modelling enhancement of cross-ventilation in sheltered buildings using stochastic optimization". *International Journal of Heat and Mass Transfer*, Vol. 118, 2018, 758–772.
28. Cebeci T, Bradshaw P. *Momentum transfer in boundary layers*. New York: Hemisphere Publishing Corporation; 1977, 377–386.
29. B.E. Launder, D.B. Spalding, "The numerical computation of turbulent flows". *Computer Methods in Applied Mechanics and Engineering*, Vol. 3, No. 2, 1974, 269–289.
30. B. Blocken, T. Stathopoulos, J. Carmeliet, "CFD simulation of the atmospheric boundary layer: Wall function problems". *Atmospheric Environment*, Vol. 41, No. 2, 2007, 238-252.
31. Y. Ozmen, E. Baydar, J.P.A.J. vanBeeck, "Wind flow over the low-rise building models with gabled roofs having different pitch angles". *Building and Environment*, Vol.95, 2016, 63–74.
32. M. Shirzadi, P.A. Mirzaei, M. Naghashzadegan, "Improvement of k-epsilon turbulence model for CFD simulation of atmospheric boundary layer around a high-rise building using stochastic optimization and Monte Carlo Sampling technique". *Journal of Wind Engineering and Industrial Aerodynamics*, Vol.171, No.October, 2017, 366–379. No.October:366–79.
33. S. Hawendi, S. Gao, "Impact of windward inlet-opening positions on fluctuation characteristics of wind-driven natural cross ventilation in an isolated house using LES". *International Journal of Ventilation*, Vol. 17, No. 2, 2018, 93–119.
34. M. Swami, & S. Chandra, "Procedures for calculating natural ventilation airflow rates in buildings". ASHRAE Final Report, Cape Canaveral, Florida, FSEC-CR-163-86, 1987.

Dynamic Behavior of Thin Graphite/Epoxy FRP Simply Supported Beam Under Thermal Load Using 3-D Finite Element Modeling

Fadi Alfaqs

Department of Mechanical Engineering, Faculty of Engineering Technology, Al-Balqa Applied University, Jordan

Received November 18 2020

Accepted June 23 2021

Abstract

Composite laminated structures have attracted much attention in recent years due to their wide range of mechanical properties and applications. However, this study presents an investigation of temperature impact as well as fiber orientation effect on mid-plane transverse deflection and interlaminar shear stress as the latter plays a crucial role in the layers' delamination in eight-layer laminated simply supported Graphite/Epoxy FRP composite beam. The beam considered is subjected to dynamic force of magnitude 1000 N concentrated in the middle as frequency varies 5-50 Hz using 3-D finite element modeling where different fiber orientations ($[0^\circ]_8$, $[0^\circ/15^\circ]_s$, $[0^\circ/30^\circ]_s$, $[0^\circ/45^\circ]_s$, $[0^\circ/60^\circ]_s$, $[0^\circ/75^\circ]_s$, and $[0^\circ/90^\circ]_s$) are considered for temperature 22, 40, and 60°C. Furthermore, modal analyses are carried out for all fiber orientations and temperatures considered. Results obtained via this study show that natural frequencies' values drop narrowly when the temperature applied on the structure rises. Moreover, dynamic mid-plane transverse and interfacial shear stress increases when increasing temperature. It should be said that comparing fiber orientations considered for every single temperature across the frequency range, fiber orientation scheme $[0^\circ]_8$ recorded minimum transverse deflection and maximum shear stress.

© 2021 Jordan Journal of Mechanical and Industrial Engineering. All rights reserved

Keywords: Laminated Beam; Dynamic; Modal, interlaminar Shear stress; Finite element;

1. Introduction

Failure of composite structures due to layers delamination is widely studied in literature where interlaminar shear stress between laminates is considered one of the main reasons of layers debonding. Normal stress effect on interlaminar shear stress of composite structures was studied where improved model of multiple notch experiments was used [1]. Moreover, method of characteristic curve was investigated in specimens containing double notches. Results obtained were compared to several failure criteria where excellent agreement was found with NU criterion. However, a review of different laminates' simulation of composite structures was presented [2]. This work studied the impact of different loading conditions on the delamination process and compared to failure models. Also, experimental results concerning toughness and impact resistance under different loading conditions were discussed.

Analytical investigation of fiber reinforced polymer (FRP) used in concrete beams subjected to impact loading was carried out to improve the beams considered [3]. However, several loading types and structures' geometry were studied using finite element (FE) package ABAQUS where models were developed using different configurations. Numerical results obtained via the FE software showed reliability concerning performance prediction of the beams considered. On the other hand, the

effect of SiC particles filled with different types of laminates was studied on interlaminar shear strength [4]. Different percentages of SiC were investigated experimentally where fractured areas were observed by electron scanner and optical microscopy as well. It is found that shear strength of laminates with SiC particles is significantly improved compared to the same structures containing no SiC particles.

Visco-plasticity was considered in failure analysis of FRP laminated composite structures when undergoing high strain rates using constitutive model [5]. Results obtained that the model considered shows the ability to predict strength of laminates in the composite structures when compared to experimental results. However, a review of dynamic behavior of FRP composite structures were investigated for several loading speeds [6]. Furthermore, effect of different strain rates of tension and compression were studied in order to observe laminates' failure for different composites.

Finite element analysis was performed to investigate the damage of FRP composites [7]. In addition, experiments were conducted to analyze the damage induced by drilling process where results were compared to finite element results obtained. On the other hand, FRP laminated composites subjected to two low velocity cylindrical impacts were investigated using finite element modeling to assess the delamination of mechanical structures' plies [8]. Also, delamination criterion was used to specify the location of the delamination. It is found that interfacial

* Corresponding author e-mail: faalfaq@bau.edu.jo.

delamination is significantly affected by the time between the two impacts applied.

Dynamic behavior FRP walls containing debonded regions was studied and analyzed where finite element models were developed to observe the nonlinear dynamic behavior [9]. In addition, von Karman criteria for different shear loads was used to model the geometry resulted from debonded regions. Results showed crucial effect of the regions considered on the dynamic behavior of the analyses. However, interlaminar normal and shear stresses were evaluated for different orientation schemes of FRP mechanical composite structures [10]. It is found laminates with fiber angles of 45° achieve maximum interfacial stresses.

Different parameters such as stacking schemes and boundary conditions were studied to evaluate the delamination process in carbon FRP laminated composite plate using FE package ANSYS [11]. Furthermore, Analytical formula was developed using Rayleigh-Ritz method and results were computed using MATLAB. It is found that fixed boundary conditions resulted in larger delamination size than simply supported conditions. Moreover, excellent agreement was observed between analytical and FE results.

Impact of thermal loading on free edge in mechanical structures were studied through developing new 2-D plane strain equations [12]. Moreover, Finite element analysis was used to implement the criteria considered to verify the results obtained. Results obtained in this work showed that interfacial stresses are well predicted when thermal load was applied locate the delaminated regions in the mechanical structure.

Effect of temperature on interfacial shear stress existing between laminates was investigated in carbon FRP composite structures [13]. Such an impact was observed using double notch shear experimental test where results were compared to a developed FE model. It is found that failure occurs due to epoxy resin softening. However, many static and dynamic experiments were carried out For bi-directional glass FRP materials to observe and analyze failure process [14]. Experimental Results obtained shows modulus of elasticity change in all three directions for different dynamic strain rates.

Dynamic and static analysis of FRP materials were studied for several environmental conditions using different types of loads including temperature [15]. In this work, failure was observed through the delaminated regions which lead eventually to material damage. It is found that environmental conditions such as temperature plays a significant role in failure process. Furthermore, thermoelastic study was conducted to investigate delamination properties of FRP composite structures where FE models were performed [16]. This analysis was concerned about the failure of laminates caused by thermal and structural conditions. It is found that stress induced thermally play a crucial role in facial delamination in mechanical composite structures.

Experimental shear tests were carried out in laminated composites where interfacial shear strength was measured through MSBS tests [17]. Moreover, FE model was developed to evaluate the results which showed clearly that a correction is needed for the equation of shear stress theory. However, structural and thermal interlaminar stresses are investigated for laminated composite shells using FE analysis [18]. The study used different fiber orientation schemes to monitor the stresses considered. Where critical interfaces were located throughout the structure.

Analysis of shear stress behavior was performed for epoxy resin- FRP composites as well as E-glass FRP laminated structures [19]. The study examined different resins and fibers. It is found that the model developed predicted the interfacial shear strength accurately. On the other hand, interlaminar shear stresses induced by harmonic and transient loads are examined for different viscoelastic laminated structures with different loading conditions [20,21]. FE model was performed to study these interfacial stresses where it is found that shear stress plays a crucial load in delamination process specially at natural frequencies. Furthermore, dynamic interlaminar shear stresses at midplane of composite simply supported thin plate were studied in different stacking fiber orientation order at several temperatures using FE package ANSYS [22]. Results revealed that increasing temperature leads to shear stress increase for all orientations considered.

FE vibration analysis of composite plates for different conditions was reviewed and simulated using ANSYS and ABAQUS softwares where it is found that natural frequencies drops when increasing the size of delamination [23,24]. However, Analytical work of composite beams was performed to study dynamic response of such beams for different conditions and materials [25,26].

In this study, FE modeling of thin simply Graphite/Epoxy laminated simply supported beam is carried out using FE package ANSYS19 in order to perform both modal and dynamic analyses of mid-plane deflections and interlaminar shear stresses under the effect of different temperature values 22, 40, and 60°C for different fiber orientation schemes ([0°]_s, [0°/15°]_s, [0°/30°]_s, [0°/45°]_s, [0°/60°]_s, [0°/75°]_s, and [0°/90°]_s).

2. Material Properties

Physical Properties of the materials used in modeling thin simply supported beam considered consisting of eight bonded perfectly layers are listed in table I. It should be mentioned that since the material is orthotropic, physical properties differ from direction to another.

Table1. Physical properties of Graphite/Epoxy FRP material used (Gu, et al.)[27]

	Direction 1	Direction 2	Direction 3
Density (Kg/m ³)	1610	-	-
Modulus of Elasticity (GPa)	144.23	9.65	9.65
Shear Modulus (GPa)	G ₁₂ = 3.45	G ₁₃ = 4.14	G ₂₃ = 4.14
Poisson's ratio	ν ₁₂ = 0.3	ν ₁₃ = 0.3	ν ₂₃ = 0.3
Thermal expansion (°C ⁻¹)	1.1 E-6	25.2 E-6	25.2 E-6
Thermal Conductivity (Wm ⁻¹ K ⁻¹)	48.44	0.8	0.8

3. Finite Element and Mathematical Modeling

3-D Finite element modeling of Graphite/Epoxy FRP simply supported laminated beam is performed using ANSYS19 where solid186 elements are being utilized to

mesh the beam considered as depicted in Fig 1. It should be said that these elements contain 20 nodes each and are capable of both structural and thermal FE analyses. Moreover, accuracy of results is improved compared to solid185 elements since the latter consists of 8 nodes. The length of the beam L is 1000mm as shown in Fig. 2 while the width is 50mm. However, each laminated layer thickness is modeled as 6.25mm. The force F which represents a dynamic force with amplitude 1000N is concentrated at the middle of the simply supported beam considered.

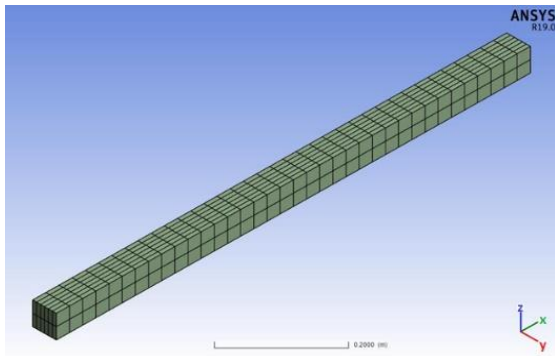


Figure1. Finite element model of simply supported beam

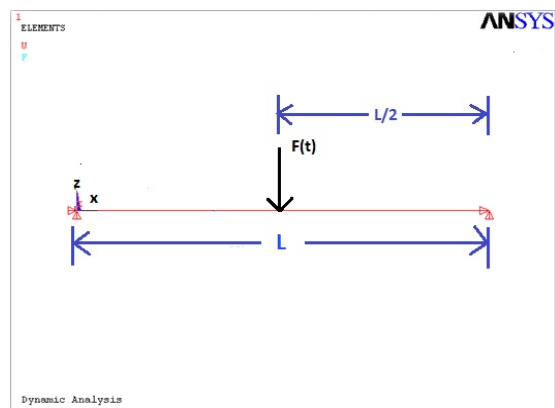


Figure2.Design Scheme for the simply supported composite beam

FE model is verified using the results obtained for free edge laminated plate [28] as shown in Fig. 3. Results obtained in current model present excellent agreement with the corresponding literature results where the free edge laminated FRP plate contains 8 layers of stacking sequence [0/90]_s. It should be said that the mechanical properties are stated in Table I .

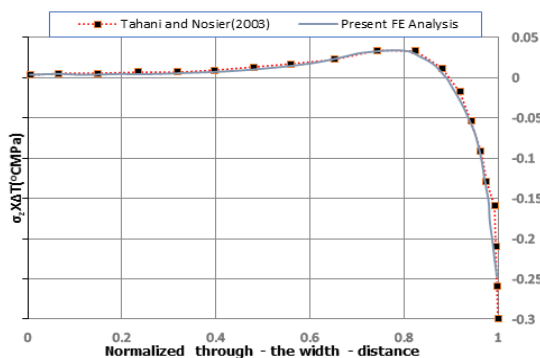


Figure3.Interfacial normal stress of free edge Graphite/Epoxy plate of an orientation scheme [0/90]_s for a temperature change 1°C (Tahani et al[22])

Fig. 4 represents the stacking sequence for a composite laminated structure. As in current case study, there are eight laminated layers in which 4 layers above midplane and same number of layers under the mid plane as well.

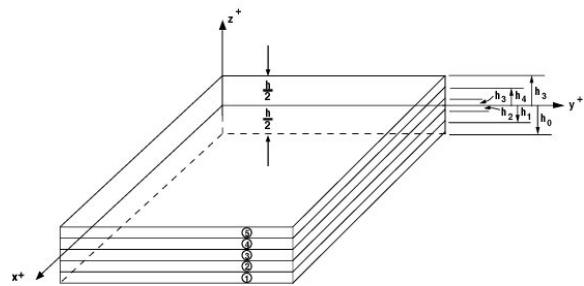


Figure4.Stacking Sequence of laminated structure

On the other hand, it should be mentioned that displacement relations according to the shear deformation theory in laminated beam are expressed as

$$\begin{aligned}
 U(x, y, z) &= u_0(x, y) - z \frac{\partial w}{\partial x}(x, y) + f(z)\Phi(x, y) \\
 V(x, y, z) &= v_0(x, y) - z \frac{\partial w}{\partial y}(x, y) + f(z)\psi(x, y) \\
 W(x, y) &= w(x, y)
 \end{aligned} \quad (1)$$

Where U, V, and W are mid-plane displacements in x,y, and z directions respectively. Φ and ψ are shear rotations. $f(z)$ is distribution function.

Assuming small displacements, strain-displacement relations become

$$\begin{aligned}
 \epsilon_x &= \frac{\partial U}{\partial x}, \epsilon_y = \frac{\partial V}{\partial y}, \epsilon_z = \frac{\partial W}{\partial z} \\
 \gamma_{xy} &= \frac{\partial U}{\partial y} + \frac{\partial V}{\partial x}, \gamma_{xz} = \frac{\partial U}{\partial z} + \frac{\partial W}{\partial x} \\
 \gamma_{yz} &= \frac{\partial V}{\partial z} + \frac{\partial W}{\partial y}
 \end{aligned} \quad (2)$$

Hence equation (1) becomes

$$\begin{aligned}
 \epsilon_x &= \frac{\partial u_0}{\partial x} - z \frac{\partial^2 w}{\partial x^2} + f(z) \frac{\partial \Phi}{\partial x} \\
 \epsilon_y &= \frac{\partial v_0}{\partial y} - z \frac{\partial^2 w}{\partial y^2} + f(z) \frac{\partial \Phi}{\partial y} \\
 \epsilon_z &= 0 \\
 \gamma_{xy} &= \frac{\partial u_0}{\partial y} + \frac{\partial v_0}{\partial x} - 2z \frac{\partial^2 w}{\partial x \partial y} + f(z) \left(\frac{\partial \Phi}{\partial y} + \frac{\partial \psi}{\partial x} \right)
 \end{aligned} \quad (3)$$

$$\gamma_{yz} = \frac{\partial f(z)}{\partial y} \Phi$$

$$\gamma_{xz} = \frac{\partial f(z)}{\partial z} \psi$$

However, considering thermal effect and shear deformations, stress-strain relations become in the kth layer

$$\begin{Bmatrix} \sigma_x \\ \sigma_y \\ \tau_{xy} \\ \tau_{yz} \\ \tau_{xz} \end{Bmatrix}^k = \begin{bmatrix} Q_{11} & Q_{12} & 0 & 0 & 0 \\ Q_{21} & Q_{22} & 0 & 0 & 0 \\ 0 & 0 & Q_{66} & 0 & 0 \\ 0 & 0 & 0 & Q_{44} & 0 \\ 0 & 0 & 0 & 0 & Q_{55} \end{bmatrix} \begin{Bmatrix} \epsilon_x - \alpha_x T \\ \epsilon_y - \alpha_y T \\ \gamma_{xy} \\ \gamma_{yz} \\ \gamma_{xz} \end{Bmatrix}^k \quad (4)$$

Where α_x and α_y are thermal expansion coefficients in x any directions respectively. T is thermal load Q_{ij} is transformed elastic coefficients

$$Q_{11} = \frac{E_1}{1 - \nu_{12}\nu_{21}}, Q_{12} = \frac{\nu_{21}E_2}{1 - \nu_{12}\nu_{21}},$$

$$Q_{22} = \frac{E_2}{1 - \nu_{12}\nu_{21}}$$

$$Q_{66} = G_{12}, Q_{55} = G_{13}, Q_{44} = G_{23}$$

Where E_1 and E_2 are material modulus of elasticity in principle directions 1 and 2 respectively. $\nu_{12}\nu_{21}$ are Poisson's ratios and $G_{12}, G_{13},$ and G_{23} are material modulus of rigidity.

4. Results and Discussion

Natural frequencies of Graphite/Epoxy composite simply supported laminated beam are obtained by performing modal analysis using 3-D finite element modeling in Ansys19 for different fiber orientation angles ($[0^\circ]_s, [0^\circ/15^\circ]_s, [0^\circ/30^\circ]_s, [0^\circ/45^\circ]_s, [0^\circ/60^\circ]_s, [0^\circ/75^\circ]_s,$ and $[0^\circ/90^\circ]_s$) at temperatures 22, 40, and 60°C as shown in tables 2, 3, and 4. Table. 2 presents the first six natural frequencies of the composite simply supported beam at 22°C for all fiber orientation schemes considered. It should be observed that should temperature increases natural frequencies decreases slightly. Furthermore, largest natural frequency 258.56Hz is obtained for fiber orientation scheme $[0^\circ]_s$.

It is clearly observed that largest fundamental natural frequency is recorded at a fiber orientation scheme $[0^\circ]_s$. However, it should be said that lowest fundamental natural frequencies are obtained for orientation schemes $[0^\circ/60^\circ]_s, [0^\circ/75^\circ]_s,$ and $[0^\circ/90^\circ]_s$ for all temperatures considered.

The first six natural frequencies are listed for all fiber orientation schemes considered for 22, 40, and 60°C as listed in table. 3 and table. 4, where it is clearly observed that highest natural frequencies are recorded at fiber

orientation scheme $[0^\circ]_s$ as 258.4 and 258.23 Hz at temperatures 40 and 60°C respectively.

Dynamic analysis for Graphite/Epoxy FRP simply supported beam is carried out using finite element modeling for fiber orientation schemes $[0^\circ]_s, [0^\circ/15^\circ]_s, [0^\circ/30^\circ]_s, [0^\circ/45^\circ]_s, [0^\circ/60^\circ]_s, [0^\circ/75^\circ]_s,$ and $[0^\circ/90^\circ]_s$ at temperatures 22, 40, and 60°C where the magnitude of force is 1000N concentrated at the middle of the beam considered. It should be mentioned that current analysis is performed for frequency range 5 – 50Hz to observe closely the effect of temperature on transverse deflection and interfacial shear stress of mid-plane at L/2. Fig. 5. shows the relation of transverse deflection of fiber angle $[0^\circ]_s$ for the three different temperatures considered. Generally, transverse deflection of mid-plane increases when temperature increases across driving frequency variation 5-50Hz. However, maximum transverse deflection is recorded 82.7mm at frequency 285Hz and temperature 22°C when modeling the simply supported beam for frequency variation 0-300 Hz. This result indicates that while higher temperature application induces higher midplane deflection, maximum deflection is obtained at room temperature (22°C) when the driving frequency matches the second natural frequency.

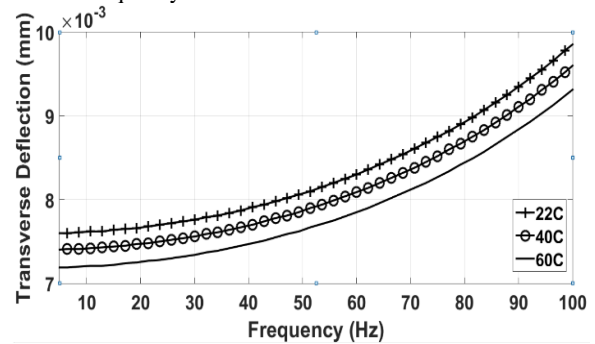


Figure5. Relation between mid-plane transverse deflection and driving frequency for Graphite/Epoxy laminated simply supported beam for $[0^\circ]_s$ at temperatures 22, 40, and 60°C

TABLE 2. Natural frequencies of composite laminated simply supported FRP beam for different orientation at temperature 22 °C

Mode	$[0^\circ]_s$	$[0^\circ/15^\circ]_s$	$[0^\circ/30^\circ]_s$	$[0^\circ/45^\circ]_s$	$[0^\circ/60^\circ]_s$	$[0^\circ/75^\circ]_s$	$[0^\circ/90^\circ]_s$
1	258.56	238.53	220.35	211.5	208.99	208.81	209.02
2	285.37	247.15	227.78	223.25	220.15	217.82	216.86
3	667.38	606.15	563.65	548.53	543.52	542.86	543.25
4	718.7	710.86	680.11	663.2	648.06	635.12	629.62
5	759.47	735.81	738.88	721.65	693.83	667.47	656.12
6	1332.3	1309.2	1223.6	1189.2	1176.5	1173.4	1173.5

TABLE 3. Natural frequencies of composite laminated simply supported FRP beam for different orientation at temperature 40 ° C

Mode	$[0^\circ]_s$	$[0^\circ/15^\circ]_s$	$[0^\circ/30^\circ]_s$	$[0^\circ/45^\circ]_s$	$[0^\circ/60^\circ]_s$	$[0^\circ/75^\circ]_s$	$[0^\circ/90^\circ]_s$
1	258.4	238.39	220.22	211.36	208.82	208.61	208.8
2	285.21	247	227.66	223.12	220	217.64	216.67
3	667.31	605.93	563.43	548.3	543.27	542.57	542.94
4	718.46	710.73	679.99	663.06	647.9	634.92	629.4
5	759.33	735.75	738.85	721.61	693.77	667.39	656.04
6	1332.1	1308.9	1223.4	1189	1176.3	1173.1	1173.2

TABLE 4. natural frequencies of composite laminated simply supported FRP beam for different orientation at temperature 60 ° C

Mode	$[0^\circ]_s$	$[0^\circ/15^\circ]_s$	$[0^\circ/30^\circ]_s$	$[0^\circ/45^\circ]_s$	$[0^\circ/60^\circ]_s$	$[0^\circ/75^\circ]_s$	$[0^\circ/90^\circ]_s$
1	258.23	238.24	220.06	211.2	208.63	208.39	208.57
2	285.04	246.84	227.53	222.98	219.83	217.44	216.45
3	667.23	605.69	563.19	548.05	542.99	542.25	542.59
4	718.19	710.57	679.86	662.91	647.71	634.69	629.16
5	759.17	735.68	738.81	721.56	693.7	667.31	655.96
6	1331.9	1308.7	1223.1	1188.8	1176	1172.8	1172.8

Dynamic mid plane deflection results of fiber orientation scheme $[0^{\circ}/15^{\circ}]_s$ at different temperatures are shown in Fig. 6 for frequency range 5 – 50Hz. It should be said that close values of deflection are obtained at temperatures 40 and 60°C and lower deflections are recorded when modeling at 22°C. However, comparing current scheme results with those of $[0^{\circ}]_s$ case, it can be concluded that mid-plane deflections of $[0^{\circ}/15^{\circ}]_s$ are much higher than the latter case which comes as a result of that the fibers angle in each laminate is longitudinal which adds strength to the mechanical structure. Furthermore, it should be noted that maximum mid-plane transverse deflection is 66.2mm at the second natural frequency when the temperature is set to 60°C.

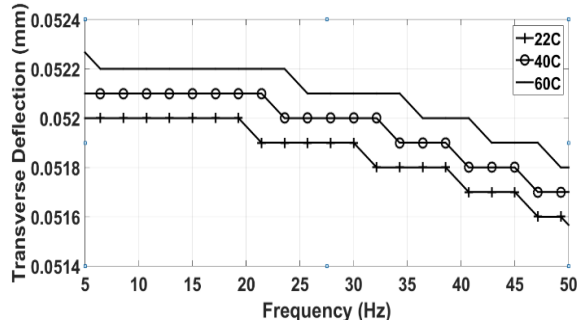


Figure 6. Relation between mid-plane transverse deflection and driving frequency for Graphite/Epoxy laminated simply supported beam for $[0^{\circ}/15^{\circ}]_s$ at temperatures 22, 40, and 60°C

Moreover, effect of temperature on laminated Graphite/Epoxy simply supported beam with fiber orientation scheme $[0^{\circ}/30^{\circ}]_s$ is investigated for frequency range 5 -50Hz and temperature variation 22, 40, and 60°C as shown in Fig. 7. It is clearly seen that should the temperature increases, harmonic deflection increases as well for driving frequency varies from 5-50Hz. It should be mentioned that maximum deflection is recorded 3.13mm at mid-plane at a frequency 220.7Hz for a temperature 22°C which represents a fundamental frequency.

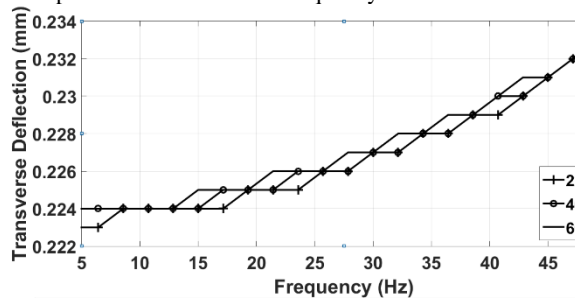


Figure7. Relation between mid-plane transverse deflection and driving frequency for Graphite/Epoxy laminated simply supported beam for $[0^{\circ}/30^{\circ}]_s$ at temperatures 22, 40, and 60°C

However, Fig. 8 to Fig. 11 present the relation between midplane transverse deflection of the laminated Graphite/Epoxy simply supported beam for driving frequency variation 5 - 50Hz at different temperatures for fiber orientation schemes $[0^{\circ}/45^{\circ}]_s$, $[0^{\circ}/60^{\circ}]_s$, $[0^{\circ}/75^{\circ}]_s$, and $[0^{\circ}/90^{\circ}]_s$ respectively. In general, same trend is observed as in previous schemes for most of the frequency range considered where it is found that increasing temperature will increase the transverse deflection induced by the

harmonic force. However, it is clearly observed in all figures considered that midplane deflection at temperatures 40 and 60°C where close results are obtained for some respectable frequency ranges. As for $[0^{\circ}/45^{\circ}]_s$ and $[0^{\circ}/60^{\circ}]_s$ cases, the frequency range 26 – 39Hz resulted in close mid-plane deflections. On the other hand, and for both orientation schemes mentioned, maximum transverse deflections are found to be 49.1 and 45.6mm respectively at the fundamental frequency and for temperature 22°C.

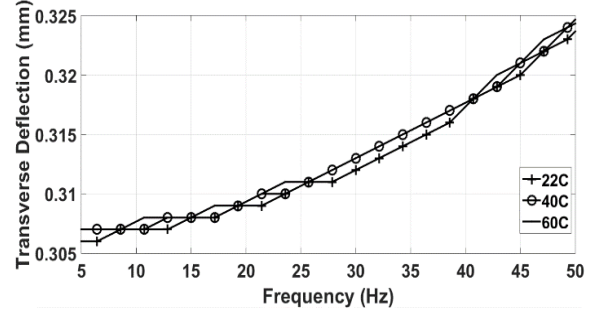


Figure8. Relation between mid-plane transverse deflection and driving frequency for Graphite/Epoxy laminated simply supported beam for $[0^{\circ}/45^{\circ}]_s$ at temperatures 22, 40, and 60°C

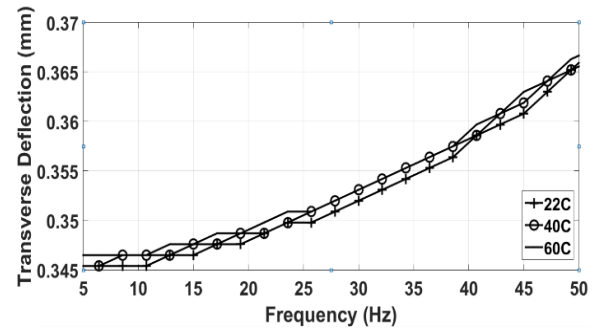


Figure9. Relation between mid-plane transverse deflection and driving frequency for Graphite/Epoxy laminated simply supported beam for $[0^{\circ}/60^{\circ}]_s$ at temperatures 22, 40, and 60°C

In the same context, fiber orientation schemes $[0^{\circ}/75^{\circ}]_s$ and $[0^{\circ}/90^{\circ}]_s$ follow the same trend concerning the mid-plane deflection behavior of simply supported beam considered in current study where higher values are obtained for higher temperatures values across driving frequency 5 – 50 Hz. It is noted that maximum values of deflections for the schemes considered are 60.3 and 45.2mm induced at the fundamental frequency when temperature is 60°C.

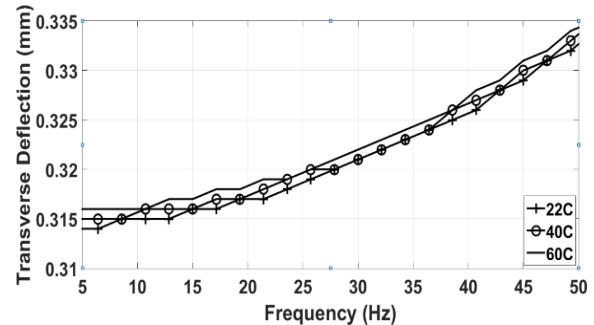


Figure10. Relation between mid-plane transverse deflection and driving frequency for Graphite/Epoxy laminated simply supported beam for $[0^{\circ}/75^{\circ}]_s$ at temperatures 22, 40, and 60°C

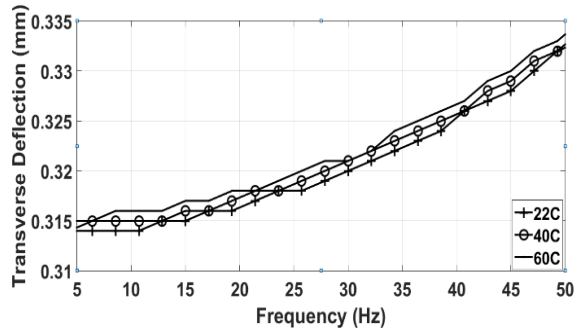


Figure11. Relation between mid-plane transverse deflection and driving frequency for Graphite/Epoxy laminated simply supported beam for $[0^{\circ}/90^{\circ}]_s$ at temperatures 22, 40, and 60°C

Similarly, Harmonic analyses for eight-layer laminated Graphite/Epoxy simply supported beam is carried out for fiber orientation schemes $[0^{\circ}]_s$, $[0^{\circ}/15^{\circ}]_s$, $[0^{\circ}/30^{\circ}]_s$, $[0^{\circ}/45^{\circ}]_s$, $[0^{\circ}/60^{\circ}]_s$, $[0^{\circ}/75^{\circ}]_s$, and $[0^{\circ}/90^{\circ}]_s$ and temperature variation (22, 40, and 60°C) at frequency range (5 - 50Hz) as depicted in Fig. 12 to Fig. 18 respectively. It should be said that shear stresses are induced due to dynamic force concentrated in the middle of the beam (at $L/2$). Fig. 12 investigates the effect of temperature on interfacial shear stress at mid plane for the orientation scheme $[0^{\circ}]_s$ and frequency range considered. It is clearly observed that for most of the frequency range, dynamic interfacial shear stress at the midplane obtains higher values when temperature increases where maximum shear stress value 81.2 MPa is recorded at the fundamental frequency for temperature 60°C. This trend is also observed in Fig. 13, that is should the temperature increases, mid-plane shear stress of the beam considered rises for the orientation scheme $[0^{\circ}/30^{\circ}]_s$. Maximum magnitude of the interfacial shear stress at mid-plane is found to be 43.2MPa for temperature 60°C.

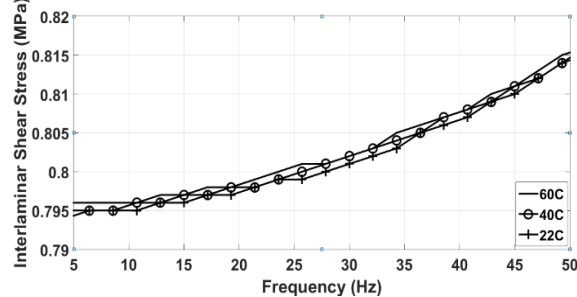


Figure12. Relation between mid-plane interfacial shear stress and driving frequency for Graphite/Epoxy laminated simply supported beam for $[0^{\circ}]_s$ at temperatures 22, 40, and 60°C

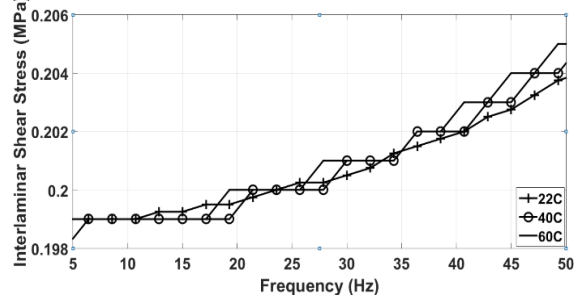


Figure13. Relation between mid-plane interfacial shear stress and driving frequency for Graphite/Epoxy laminated simply supported beam for $[0^{\circ}/15^{\circ}]_s$ at temperatures 22, 40, and 60°C

However, the results of interlaminar shear stress obtained for frequency range 21 – 46Hz are nearly similar for temperatures 50 and 60°C for stacking sequence $[0^{\circ}/30^{\circ}]_s$ as shown in Fig. 14. where Lowest values of stress are recorded for room temperature. It should be mentioned that maximum interfacial shear stress is recorded 0.017 MPa at the first natural frequency for temperature 22°C. Moreover, it can be clearly seen that there are constant values of shear stress at large portions of frequency for all temperatures considered.

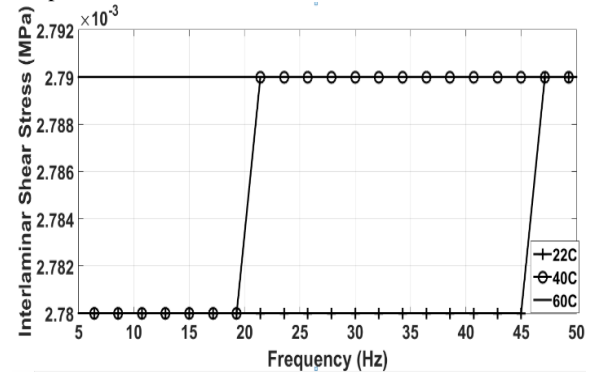


Figure14. Relation between mid-plane interfacial shear stress and driving frequency for Graphite/Epoxy laminated simply supported beam for $[0^{\circ}/30^{\circ}]_s$ at temperatures 22, 40, and 60°C

Fig. 15 to Fig. 18 illustrate the impact of temperature on interlaminar shear stress at the mid-plane for the composite simply supported beam considered concerning orientation schemes $[0^{\circ}/45^{\circ}]_s$, $[0^{\circ}/60^{\circ}]_s$, $[0^{\circ}/75^{\circ}]_s$, and $[0^{\circ}/90^{\circ}]_s$ respectively . It is clearly concluded that for all the cases considered increasing temperature leads to narrow interfacial shear stress increase at the mid plane. Also, it should be noted that a maximum shear stress of 17.8MPa for the fiber orientation scheme $[0^{\circ}/45^{\circ}]_s$ is recorded at frequency 212.1HZ which represents a fundamental frequency for the scheme and temperature considered. In the same context, Maximum shear stress for orientations schemes $[0^{\circ}/60^{\circ}]_s$, $[0^{\circ}/75^{\circ}]_s$, and $[0^{\circ}/90^{\circ}]_s$ are found to be 8.27, 4.69, and 3.86Mpa respectively at the fundamental frequency computed in modal analyses at 60°C. Moreover, the nonlinear behavior observed in the shear stress response of the $[0^{\circ}/90^{\circ}]_s$ case recorded very close results although same effect of temperature remains identical for rest of case considered.

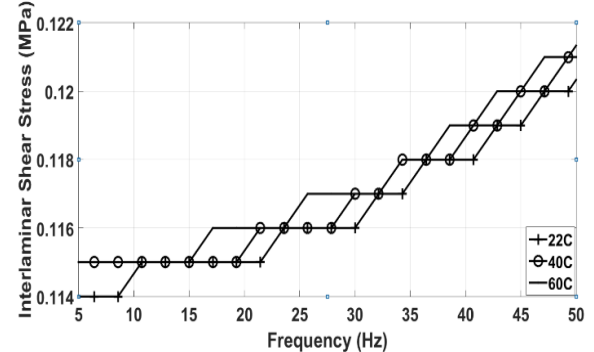


Figure15. Relation between mid-plane interfacial shear stress and driving frequency for Graphite/Epoxy laminated simply supported beam for $[0^{\circ}/45^{\circ}]_s$ at temperatures 22, 40, and 60°C

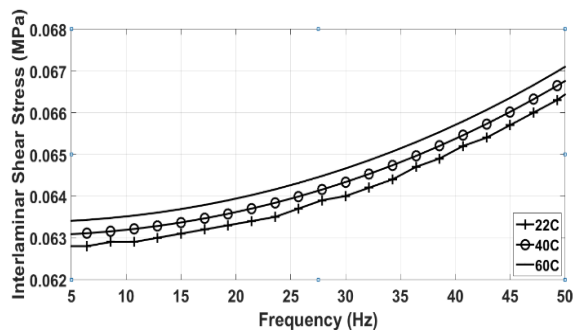


Figure 16. Relation between mid-plane interfacial shear stress and driving frequency for Graphite/Epoxy laminated simply supported beam for $[0^{\circ}/60^{\circ}]_s$ at temperatures 22, 40, and 60°C

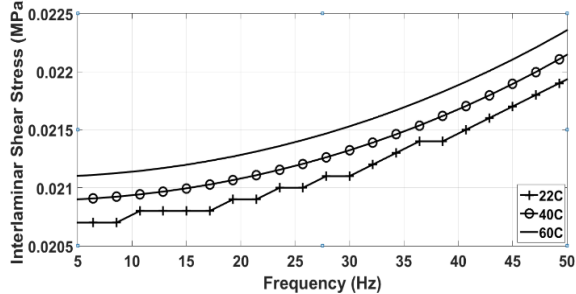


Figure 17. Relation between mid-plane interfacial shear stress and driving frequency for Graphite/Epoxy laminated simply supported beam for $[0^{\circ}/75^{\circ}]_s$ at temperatures 22, 40, and 60°C

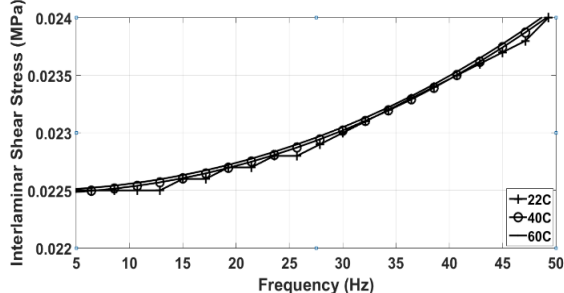


Figure 18. Relation between mid-plane interfacial shear stress and driving frequency for Graphite/Epoxy laminated simply supported beam for $[0^{\circ}/90^{\circ}]_s$ at temperatures 22, 40, and 60°C

Comparing mid-plane harmonic deflection and shear stress of simply supported composite beam considered for all fiber orientations ($[0^{\circ}]_s$, $[0^{\circ}/15^{\circ}]_s$, $[0^{\circ}/30^{\circ}]_s$, $[0^{\circ}/45^{\circ}]_s$, $[0^{\circ}/60^{\circ}]_s$, $[0^{\circ}/75^{\circ}]_s$, and $[0^{\circ}/90^{\circ}]_s$) across frequency range 5 - 50Hz at temperatures 22, 40, and 60°C shows that highest and lowest deflections are recorded for schemes $[0/60]_s$ and $[0^{\circ}]_s$ respectively. This is reasonable since the latter scheme leads to a structure with much higher strength than all other fiber orientation schemes. It is also noted that schemes $[0^{\circ}/60^{\circ}]_s$, $[0^{\circ}/90^{\circ}]_s$, and $[0^{\circ}/45^{\circ}]_s$ undergo much higher transverse deflections than other schemes. Furthermore, it should be observed that maximum shear stress existing between layers at midplane undergoes close range values for most of the schemes except at the orientation scheme $[0^{\circ}]_s$ where large values are recorded due to large strength of this orientation scheme.

5. Limitation and Future scope

Accuracy of finite element results remain an issue when solving for stresses when sudden change in geometry occurs. As a result, induced stresses may be larger at these locations than the yield stress since linear finite element analysis may not predict results accurately. However, studying dynamic facial shear stresses in laminated FRP

spherical and cylindrical shells is highly recommended to investigate the failure of such structures with different boundary conditions due to temperature and frequency effect using FE analysis.

6. Conclusion

This work investigates dynamic behavior of Graphite/Epoxy FRP eight-layer laminated simply supported beam at different temperatures (22, 40, and 60°C) and for fiber orientation schemes ($[0]_s$, $[0^{\circ}/15^{\circ}]_s$, $[0^{\circ}/30^{\circ}]_s$, $[0^{\circ}/45^{\circ}]_s$, $[0^{\circ}/60^{\circ}]_s$, $[0^{\circ}/75^{\circ}]_s$, and $[0^{\circ}/90^{\circ}]_s$) across frequency variation 5-50 Hz using finite element package ANSYS19.

Modal analysis is carried out to find out the first six natural frequencies for all fiber orientation schemes and temperatures considered where results showed that natural frequencies drop slightly for all the schemes considered at each temperature.

It is found that higher natural frequencies are obtained for fiber orientation scheme $[0]_s$ where highest natural frequencies are recorded at fiber orientation scheme $[0^{\circ}]_s$ as 258.56, 258.4, and 258.23 Hz at temperatures 22, 40 and 60°C respectively.

Concerning the harmonic analyses, it should be mentioned that both interfacial mid-plane transverse deflection and shear stress responses are found to increase narrowly when increasing temperature for all schemes considered. Moreover, it is concluded that $[0]_s$ case presents a significant scheme since it undergoes minimum transverse deflection and maximum shear stress at each single temperature compared with other schemes. Also, it should be noted that specific shear stress responses share almost the same results at temperatures 40 and 60°C as results show in $[0^{\circ}/30^{\circ}]_s$, $[0^{\circ}/45^{\circ}]_s$ cases.

Largest transverse deflection recorded is 82.7mm at frequency 285Hz and temperature 22°C when modeling the simply supported beam for with $[0]_s$ orientation scheme. However, maximum shear stress value 81.2 MPa is obtained at the same fiber orientation for temperature 60°C

Acknowledgements

This work was supported by Al-Balqa Applied University. In addition, Ali Al-Foqaha presented a helpful data throughout this study.

References

- [1] Li, F., Deng, A. Z., Zhao, Q. L., & Duan, J. (2020). Research on Influence mechanism of composite interlaminar shear strength under normal stress. *Science and Engineering of Composite Materials*, 27(1), 119–128. <https://doi.org/10.1515/secm-2020-0011>
- [2] Tabiei, A., & Zhang, W. (2018). Composite laminate delamination simulation and experiment: A review of recent development. In *Applied Mechanics Reviews* (Vol. 70, Issue 3). American Society of Mechanical Engineers (ASME). <https://doi.org/10.1115/1.4040448>
- [3] Roudsari, S., Hamoush, S., Soleimani, S., Abu-Lebdeh, T., & Haghhighifar, M. (2018). Analytical Study of Reinforced Concrete Beams Strengthened by FRP Bars Subjected to Impact Loading Conditions. *American Journal of Engineering and Applied Sciences Original Research Paper*. <https://doi.org/10.3844/ajeassp.2018>
- [4] Alsaadi, M., Uglu, A. A., & Erklig, A. (2017). A comparative study on the interlaminar shear strength of carbon, glass, and Kevlar fabric/epoxy laminates filled with SiC particles.

- Journal of Composite Materials*, 51(20), 2835–2844. <https://doi.org/10.1177/0021998317701559>
- [5] Eskandari, S., Andrade Pires, F. M., Camanho, P. P., Cui, H., Petrinic, N., & Marques, A. T. (2019). Analyzing the failure and damage of FRP composite laminates under high strain rates considering visco-plasticity. *Engineering Failure Analysis*, 101, 257–273. <https://doi.org/10.1016/j.engfailanal.2019.03.008>
- [6] Chandra Ray, B., & Rathore, D. (2015). A review on mechanical behavior of FRP composites at different loading speeds. In *Critical Reviews in Solid State and Materials Sciences* (Vol. 40, Issue 2, pp. 119–135). Taylor and Francis Inc. <https://doi.org/10.1080/10408436.2014.940443>
- [7] Rakesh, P. K., Sharma, V., Singh, I., & Kumar, D. (2011). *Delamination in Fiber Reinforced Plastics: A Finite Element Approach*, 3, 549–554. <https://doi.org/10.4236/eng.2011.34064>
- [8] Chakraborty, D. (2007). Delamination of laminated fiber reinforced plastic composites under multiple cylindrical impact. *Materials and Design*, 28(4), 1142–1153. <https://doi.org/10.1016/j.matdes.2006.01.029>
- [9] Elmalich, D., & Rabinovitch, O. (2015). Dynamic Geometrically Nonlinear Behavior of FRP-Strengthened Walls with Debonded Regions. *Journal of Engineering Mechanics*, 141(1), 04014105. [https://doi.org/10.1061/\(asce\)em.1943-7889.0000814](https://doi.org/10.1061/(asce)em.1943-7889.0000814)
- [10] Sankara Babu Ch. S., Rao, V. T., & Kumar, S. B. (2018). *Effect of Fiber Angle on Interlaminar Stresses of FRP Angle Ply Laminate* (Vol. 6, Issue 1). www.ijcrt.org
- [11] Imran, M., Khan, R., & Badshah, S. (2019). Investigating the effect of delamination size, stacking sequences and boundary conditions on the vibration properties of carbon fiber reinforced polymer composite. *Materials Research*, 22(2). <https://doi.org/10.1590/1980-5373-MR-2018-0478>
- [12] Islam, M. S., & Prabhakar, P. (2017). Modeling framework for free edge effects in laminates under thermo-mechanical loading. *Composites Part B: Engineering*, 116, 89–98. <https://doi.org/10.1016/j.compositesb.2017.01.072>
- [13] Li, J., Fan, W., Liu, T., Yuan, L., Xue, L., Dang, W., & Meng, J. (2020). The temperature effect on the inter-laminar shear properties and failure mechanism of 3D orthogonal woven composites. In *Textile Research Journal* (Vol. 90, Issues 23–24, pp. 2806–2817). SAGE Publications Ltd. <https://doi.org/10.1177/0040517520927009>
- [14] Liu, Z., Yang, Z., Chen, Y., Yu, Y., Wei, Y., Li, M., & Huang, C. (2020). Dynamic tensile and failure behavior of bi-directional reinforced GFRP materials. *Acta Mechanica Sinica/Lixue Xuebao*, 36(2), 460–471. <https://doi.org/10.1007/s10409-019-00920-8>
- [15] Mahato, K. K., Dutta, K., & Ray, B. C. (2018). Static and Dynamic Behavior of Fibrous Polymeric Composite Materials at Different Environmental Conditions. *Journal of Polymers and the Environment*, 26(3), 1024–1050. <https://doi.org/10.1007/s10924-017-1001-x>
- [16] Panda, S. K., & Pradhan, B. (2007). Thermoelastic analysis of the asymmetries of interfacial embedded delamination characteristics in laminated FRP composites. *Composites Part A: Applied Science and Manufacturing*, 38(2), 337–347. <https://doi.org/10.1016/j.compositesa.2006.03.012>
- [17] Shivakumar, K., Pora, A., & Abali, F. (n.d.). INTERLAMINAR SHEAR TEST FOR LAMINATED TEXTILE FABRIC COMPOSITES.
- [18] Das, R. R., Singla, A., & Srivastava, S. (2016). Thermo-mechanical Interlaminar Stress and Dynamic Stability Analysis of Composite Spherical Shells. *Procedia Engineering*, 144, 1060–1066. <https://doi.org/10.1016/j.proeng.2016.05.058>
- [19] Wang, X., Zhao, X., Wu, Z., Zhu, Z., & Wang, Z. (2016). Interlaminar shear behavior of basalt FRP and hybrid FRP laminates. *Journal of Composite Materials*, 50(8), 1073–1084. <https://doi.org/10.1177/0021998315587132>
- [20] Al-Huniti, N., Al-Faqs, F., & Abu Zaid, O. (2010). Finite Element Dynamic Analysis of Laminated Viscoelastic Structures. *Applied Composite Materials*, 17(4), 405–414. <https://doi.org/10.1007/s10443-010-9129-z>
- [21] Alfaqs, F. (2020). Dynamic analysis of thin laminated viscoelastic structures under elevated temperature using finite element modeling. *Naukovyi Visnyk Natsionalnoho Hirnychoho Universytetu*, 2020(6), pp. 28–33. <https://doi.org/10.33271/mvngu/2020-6/028>
- [22] Alfaqs, F., Haddad, J., Fayyad, S., Koroviaka, Y., Rastsvietaiev, V., Effect of Elevated Temperature on Harmonic Interlaminar Shear Stress in Graphite/Epoxy FRP Simply Supported Laminated Thin Plate Using Finite Element Modeling, (2020) International Review of Mechanical Engineering (IREME), 14 (8), pp. 523–533. <https://doi.org/10.15866/ireme.v14i8.1946>
- [23] Imran, M., Khan, R., Badshah, S. (2021). 'Experimental, analytical, and finite element vibration analyses of delaminated composite plates', *Scientia Iranica*, 28(1), pp. 231–240. doi: 10.24200/sci.2019.51508.2223
- [24] Imran, M., Badshah, S., & Khan, R. (2019). Vibration Analysis of Cracked Composite Laminated Plate: A Review. *Mehran University Research Journal Of Engineering And Technology*, 38(3), 705–716. doi:10.22581/muet1982.1903.14
- [25] Ghadiri, M., Malekzadeh, K., & Ghasemi, F. A. (2015). Free Vibration of an Axially Preloaded Laminated Composite Beam Carrying a Spring-Mass-Damper System with a NonIdeal Support. *Jordan Journal of Mechanical & Industrial Engineering*, 9(3), pp. 195–207
- [26] Gharaibeh, M., Ismail, Adel A., Al-Shammery, Ahmad F., Ali, Omar A. (2019). Three-Material Beam: Experimental Setup and Theoretical Calculations. *Jordan Journal of Mechanical & Industrial Engineering*, 13(4) pp. 253–264.
- [27] [21] Gu, H., Chattopadhyay, A., Li, J., & Zhou, X. (2000). A higher order temperature theory for coupled thermo-piezoelectric-mechanical modeling of smart composites. *International Journal of Solids and Structures*, 37(44), pp.6479–6497. [https://doi.org/10.1016/s0020-7683\(99\)00283-8](https://doi.org/10.1016/s0020-7683(99)00283-8)
- [28] [22] Tahani, M., & Nosier, A. (2003). Free edge stress analysis of general cross-ply composite laminates under extension and thermal loading. *Composite Structures*, 60(1), pp.91–103. [https://doi.org/10.1016/s0263-8223\(02\)00290-8](https://doi.org/10.1016/s0263-8223(02)00290-8).

Effect of Alkaline Nitrates and Operating Temperature on the Performance of Dye Sensitized Solar Cells

Mohamad I. Al-Widyan^{a,*}, Borhan A. Albiss^b, Mohammad S. Ali^c

^aMechanical Engineering Department- Jordan University of Science and Technology, PO Box 3030, Irbid 22110, Jordan

^bNanomaterials Lab., Department of Physics- Jordan University of Science and Technology, PO Box 3030, Irbid 22110, Jordan

^cGraduate Student, Mech. Eng. - Jordan University of Science and Technology, PO Box 3030, Irbid 22110, Jordan

Received July 20 2019

Accepted July 27 2021

Abstract

This work sought to investigate experimentally the applicability of an alkaline nitrate (NaNO₃ and KNO₃)-coated TiO₂ working electrode in a dye-sensitized solar cell (DSSC) in enhancing the cell's performance. A simple dipping method was used to modify the surfaces of TiO₂ films with nitrate aqueous solutions with concentrations of 0.01M, 0.05M and 0.1M. Using standard SEM, XRD and UV-Vis apparatus, the modified cell performance was compared with an equivalent bare-TiO₂ surface in terms of performance at two temperature levels. It was found that with higher alkaline concentrations, the electrode surface was covered with smaller, denser and nicely oriented nitrate nanoparticles, as well as superior optical performance and a quite successful incorporation of the alkaline nitrates with TiO₂ paste. The modified DSSC consistently showed higher power conversion efficiency. Specifically, findings indicate that the power conversion efficiency of the modified cell increased by up to 200% relative to its unmodified one. In addition, it was found that the conversion efficiency using NaNO₃-TiO₂/ITO layer was better compared to the KNO₃-TiO₂/ITO layer at all concentrations and temperature levels considered. The highest power conversion efficiency was recorded in the DSSC with NaNO₃ (0.1)-TiO₂/ITO layer at 1.029% and 0.84% at 13 °C and 40 °C, respectively. Moreover, the findings reaffirmed the positive effect of lower temperature on cell performance.

© 2021 Jordan Journal of Mechanical and Industrial Engineering. All rights reserved

Keywords: Dye-sensitized solar cells, Cell performance, Cell temperature, Electrode modification, Alkaline nitrates, TiO₂ nanoparticles;

1. Introduction

It is almost universally accepted that fossil fuels are not a sustainable energy source as they were formed by the decomposition of dead plants and animals under extreme heat and pressure over millions of years. In contrast, renewable energy sources provide a promising energy source since they are naturally replenished. As per the World Energy Council for 2013, renewable sources made up about 11% of the world's total primary energy supply in 2011, and are projected to reach about 16% in 2020 [1].

Among all renewable sources, solar energy offers the most potential and promise [2-4]. In the long term (up to 2050) and due to its distinct features, solar energy is expected to play a prominent role as an energy source and in climate change mitigation. In addition, conversion of solar energy to electricity is one of the most desired and convenient conversion technologies and may be achieved in two ways: PV solar cells and concentrating solar power [5]. PV cells enjoy the advantage of directly converting solar radiation to electricity.

PV solar cells are classified into three generations based on their performance and cost effectiveness. Crystalline silicon cells (1st Generation), also called traditional, conventional o

r wafer-based cells, are made of crystalline silicon [6]. Thin-film cells (2nd Generation) are made of thin layers of photosensitive materials (thickness < micrometer) on a low-cost substrate such as stainless steel, glass or a polymer foil [7]. Dye-sensitized cells (3rd Generation), widely known as DSSCs, are one of a third generation PV and are based on semiconductor structures.

Dye-sensitized solar cells represent one of the best alternatives and strongest substitutes for silicon or thin-film solar cells due to the low material cost and simplicity of fabrication [8]. Although they are still in the pre-commercial stage, commercial efficiencies have reached 4% to 5% and laboratory efficiencies of 12% [9]. Since their invention and development by Michael Grätzel and Brian O' Regan in 1991, DSSCs have attracted serious interest and gained widespread acceptance as a promising technology of renewable energy since they have an apparent edge over their counterparts [10, 11]. However, although the scientific community has succeeded for the past 20 years in improving DSSCs, the gains in efficiencies have not been staggering [12, 13, 14]. Recently, research efforts focus on enhancing power conversion efficiencies and reduce the gap between today's benchmark and Shockley-Queisser limit [15, 16]. DSSCs based on TiO₂ as photo anodes and doped photo anodes have been also studied [17]. Studies discussed how TiO₂ comparatively stands as the best with alternative

* Corresponding author e-mail: widyan@just.edu.jo.

oxides by virtue of its unique properties and the analysis of various factors affecting the performance of TiO₂-based DSSCs. Moreover, the necessity and impact of doping in TiO₂ toward the improvement in the performance of DSSC was explored. In a systematical study, Chu et al. [18] investigated the nano-scale structural changes of the TiO₂ DSSC electrode due to the alkaline and thermal treatments. Photovoltaic performance was measured and revealed the effect of microstructural changes. Such electrode coatings can be considered as potential candidates for the electrode material in a DSSC. Experimental results revealed that TiO₂ layer with a 3D network 'nano-flaky' was prepared with sizes of around 100 to 200 nm across and thickness of less than 10 nm that cover the outermost surface, as well as the inner pores and voids. This scheme provides a larger surface area for dye absorption and thus increases the efficiency of assembled DSSC.

The basic concept of DSSCs is simple, and it, basically, imitates plant photosynthesis process. Figure 1 shows the structure and general mechanism of energy conversion in a typical DSSC [19, 20].

In this work, the main objective was to experimentally investigate the impact of introducing modifications to the photoelectrodes on the performance of a locally fabricated and assembled DSSC by attempting to reduce charge recombination and alleviate the negative effect of cell operating temperature [21, 22]. The modifications involved mainly applying different concentrations of dilute nano-scale aqueous solutions of two alkaline nitrates that were separately applied to the bare- TiO₂ photoelectrodes via a soaking process [23]. The cell performance was evaluated mainly by its voltage-current (V-J) characteristics at two temperature levels. Standard tests using UV-Vis, SEM, and XRD were conducted to evaluate relevant properties of the photoelectrodes and the size and morphology of the nanocrystals.

2. Materials and Methods

This work involved three basic parts, namely, modifying the cell's photoelectrodes which entailed preparing and

using aqueous solutions with various concentrations, namely, 0.01 M, 0.05 M, and 0.10 M, of sodium nitrate (NaNO₃) and potassium nitrate (KNO₃) nanoparticles via a soaking process; fabricating and assembling a DSSC in the lab as per the modifications indicated above; and finally, evaluating the fabricated cell performance.

2.1. Preparation of solutions

2.1.1. NaNO₃ and KNO₃ aqueous solutions

Particles of NaNO₃ and KNO₃ were manually ground by mortar to get their respective nanoparticles which were later characterized by scanning electron microscope (SEM). Then, 50 mL of distilled water were added to the resulting NaNO₃ or KNO₃ nanoparticles to produce different concentrations of aqueous solutions. Table 1 shows the different amounts of materials used to produce desired concentrations of both aqueous solutions. The solutions of KNO₃ and NaNO₃ were stirred in a hot plate for 15 min at 60 °C, followed by placing them in an ultrasonic bath for 15 min.

2.1.2. TiCl₄ aqueous solution

To obtain 40 mM TiCl₄ solution, a volume of 0.45 ml of TiCl₄ was added to 99.55 ml of ice cold deionized water in a fume hood and then stirring the mixture for 30 min. A general procedure in the assembly of DSSCs is to deposit a thin film of TiO₂ by submerging the substrate in the 40 mM aqueous TiCl₄ solution at 70 °C for a period of time. The TiCl₄ is then used to produce the pigment titanium dioxide (TiO₂) according to the following equation:



2.1.3. The dye solution

The N749 black dye was employed as the sensitizer. The dye solution (0.3 mM) was prepared by adding 0.0205 g of the dye in 50 ml of ethanol which was used as the solvent. The solution was stirred for 30 min and stored in a sealed container for 24 hours before use. The dye solution was stored away from light.

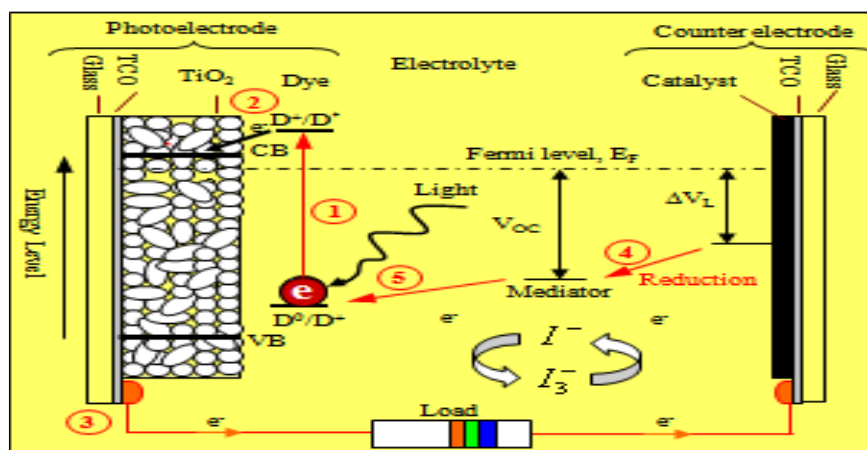


Figure 1: Structure and working principle of TiO₂- based DSSCs.

2.2. Fabrication and assembly of the DSSC

2.2.1. Materials used in preparing the solar cells

The following materials were used: Indium tin oxide (ITO, In_2O_3 : Sn) coated glass electrodes ($2.5\text{ cm} \times 1.8\text{ cm}$, 2 slides per cell); Anatase TiO_2 nanoparticle colloid; Black dye N749; Platinum precursor solution; A redox (I^-/I_3^-) electrolyte solution composed of 0.5M lithium iodide and 0.05M iodine in acetonitrile with γ -Butyrolactone as a solvent to improve volatility; Binder clips (small, 2 pieces for 1 cell); Ethanol; Deionized water, Distilled water; and Detergent solution.

2.2.2. Fabrication and assembly of the cell

Indium-doped tin oxide (ITO) conductive glass substrate was cut into pieces of dimensions $1.8\text{ cm} \times 2.5\text{ cm}$. ITO glasses were cleaned by a detergent solution for 10 min, water for 10 min and ethanol for 10 min using an ultrasonic bath, and then dried in a furnace at $70\text{ }^\circ\text{C}$ for 20 min. The ITO glasses were immersed in a 40 mM TiCl_2 solution at $70\text{ }^\circ\text{C}$ for 30 min.

A TiO_2 paste was prepared by adding 3.5g of TiO_2 nano-powder to 15 ml of ethanol, followed by adding a Polyvinylpyrrolidone binder (PVP) to the nano-powder in a weight ratio of 10:1. The TiO_2 mixture was stirred on a hot plate until the paste became uniform. The paste was finally subject to sonication for 15 min. An active film of TiO_2 paste was formed on the ITO glass via a doctor-blade method.

The TiO_2 paste films were gradually heated by air at $60\text{ }^\circ\text{C}$ for 5min, $80\text{ }^\circ\text{C}$ for 5 min and then $100\text{ }^\circ\text{C}$ for 5 min using a hair dryer to drive off water and carbon dioxide. Again, the TiO_2 films were treated with 40 mM TiCl_4 solution for 1 min., annealed at $500\text{ }^\circ\text{C}$ for 40 min and then slowly cooled in a furnace to develop equilibrium structure.

The NaNO_3 - TiO_2 /ITO and KNO_3 - TiO_2 /ITO electrodes were fabricated via a dipping process in which TiO_2 /ITO electrodes were separately soaked into the aqueous solutions of NaNO_3 and KNO_3 at concentrations of 0.01 M, 0.05 M and 0.1 M for 30 sec, followed by rinsing with deionized water. Then, seven electrodes were dried at $120\text{ }^\circ\text{C}$ for 30 min in a furnace. Upon cooling them down to $80\text{ }^\circ\text{C}$, the bare- TiO_2 /ITO electrode, the NaNO_3 - TiO_2 /ITO electrodes and the KNO_3 - TiO_2 /ITO electrodes were

separately immersed into a 0.3 mM of N749 black dye solution for 24 h.

The counter electrodes were prepared by placing a drop of 3 mM H_2PtCl_6 solution on ITO glass, then drying it at $150\text{ }^\circ\text{C}$ for 30 min. The working electrodes and platinum-counter electrodes were assembled into a sandwich type cell and sealed with binder clips. Then, a drop of electrolyte was placed between the working electrode and the platinum-counter electrode. To improve conductivity, copper paste was added to the edges of the cell.

2.3. Evaluation of cell performance

Various techniques were used to examine the cell performance after introducing the modifications indicated in this study. Such techniques included scanning electron microscopy (SEM), X-ray diffraction (XRD), ultraviolet-visible spectroscopy (UV-Vis). The cell's current-voltage data was gathered by a Keithley 2425 source meter along with the Lab-View software as shown in Figure 2.

PV tests of surface-modified (NaNO_3 - TiO_2 /ITO and KNO_3 - TiO_2 /ITO) and non-modified (bare- TiO_2 /ITO) photoelectrodes were performed by experimentally producing the electric current density vs. voltage, J vs. V, curves using a LED array of 10 mW/m^2 at two different temperatures, namely, $40\text{ }^\circ\text{C}$ and $13\text{ }^\circ\text{C}$. The area of the modified surface was $0.0001\text{ (}1 \times 10^{-4}\text{)}\text{ m}^2$. The cell performance was evaluated by measuring the short circuit current density (J_{sc}), open circuit voltage (V_{oc}), fill factor (FF) and energy conversion efficiency (η). The values of J_{sc} and V_{oc} can be obtained directly using the current-voltage, I-V, data. The FF and η were calculated, respectively, from the following two equations [11] (Okoli, 2010; Lellig, 2012):

$$FF = \frac{I_m \times V_m}{I_{sc} \times V_{oc}} = \frac{P_m}{I_{sc} \times V_{oc}} \quad (2)$$

$$\eta = \frac{P_o}{P_i} = \frac{FF \times V_{oc} \times I_{sc}}{P_i} \quad (3)$$

where, P_o = the electrical power output

P_i = the energy input from the sun

m = the subscript "m" stands for the maximum power point

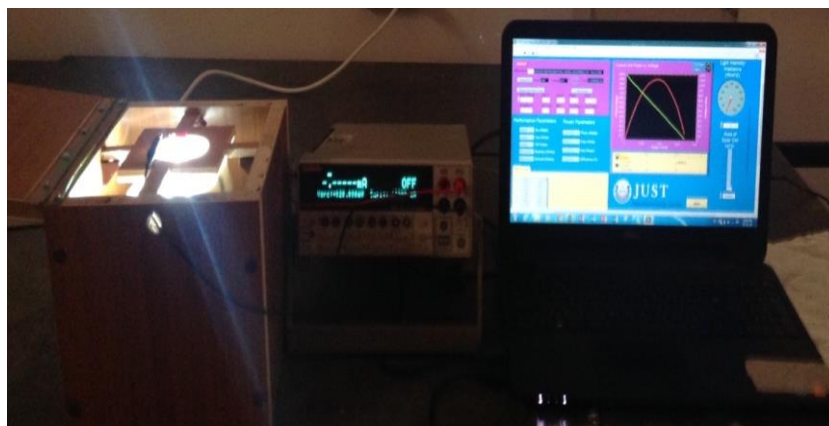


Figure 2. Keithley 2425 instrument, Lab-View program and light simulator used for the measurement of the photocurrent-photovoltage characteristics.

The structure and morphological characterization of the DSSC were studied by scanning electron microscope (SEM: Quanta FEI 450 SEM machine). The intention was to get a high-resolution surface image and thus have the shape and size of clusters from which the diameter of the TiO₂ nanoparticles can be determined. As for the crystalline structure of the photoelectrode, an X-ray diffraction technique (XRD-6000, Shimadzu) using Ni-filtered Cu K α line ($\lambda = 0.15418$ nm) at a scanning rate of 2° min^{-1} in 2θ ranging from 0° to 80° was utilized. Bare-TiO₂/ITO films were dipped into KNO₃ or NaNO₃ aqueous solution and during the soaking process, the nitrate ions were adsorbed onto the surface of TiO₂. NaNO₃ or KNO₃ phase was verified by the XRD.

2.4. Effect of temperature on cell performance

Experiments were conducted at two temperature levels, namely, 40°C and 13°C . The intention was to examine and validate the effect of temperature on cell performance.

3. Results and Discussion

3.1. The fabricated/assembled cell

Figure 3 depicts the cell that was fabricated and assembled in this study. The same cell was also used in all measurements made in this work. DSSC consists of a transparent conducting glass electrode with a porous TiO₂ layer coated with an organic dye (in our case) that serves as light sensitizer, an electrolyte layer, and a counter electrode, typically coated with graphite. The electrodes were fixed using two clips and sealed firmly in order to prevent leakage of the dye and electrolyte. In DSSCs, dyes play an important role in solar energy harvesting. Therefore, cell performance is mainly dependent on the type of dyes used as a sensitizer.

The following notes should be considered during DSSC fabrication:

- Temperature stability given that at low temperatures the electrolyte can freeze, preventing power production and potentially leading to fluctuation in cell conversion efficiency due to mechanical defects in the microstructure.

- Porous microstructures of the TiO₂ layers with high surface area are essential for achieving high efficiency in the DSSC system because a large amount of dye can be adsorbed on the surface of the nc-TiO₂ particles resulting in an increased solar light absorption and an increased reacting interface per unit area.

3.2. Photoelectrode morphology (SEM results)

The SEM image of the bare-TiO₂/ITO in Figure 4 shows that the particles are of irregular shape and of non-uniform size. Figure 4 also shows that the particles have highly mesoporous foam-like structure and agglomerated to nearly spherical morphology which may be due to annealing of TiO₂ powder. Also, the same figure shows that there are some pores and voids between the grains, and the grain boundaries are randomly oriented. Similarly, SEM images were obtained for the 0.01 and 0.05 M concentrations for both nitrates and demonstrated particles with better features.

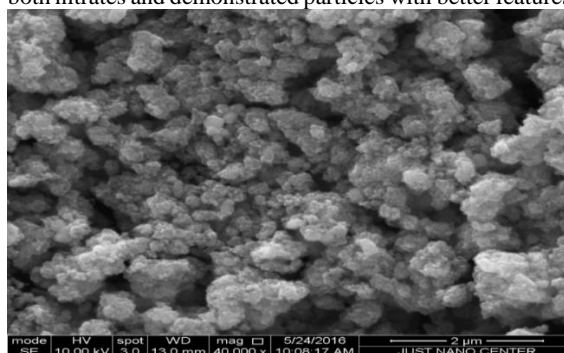


Figure 4. Scanning electron microscopy image of bare-TiO₂/ITO surface.

In contrast, Figure 5 presents the SEM image for samples with the highest concentration considered in this study, i.e., 0.10 M. As seen from the microstructure, the surface of the electrode is covered with NaNO₃ or KNO₃ nanoparticles with an average size of approximately 1.0 nm, which is smaller than that for the samples modified with lower concentrations. Figure 5 further exhibits a significantly denser microstructure with nicely oriented grain boundaries.

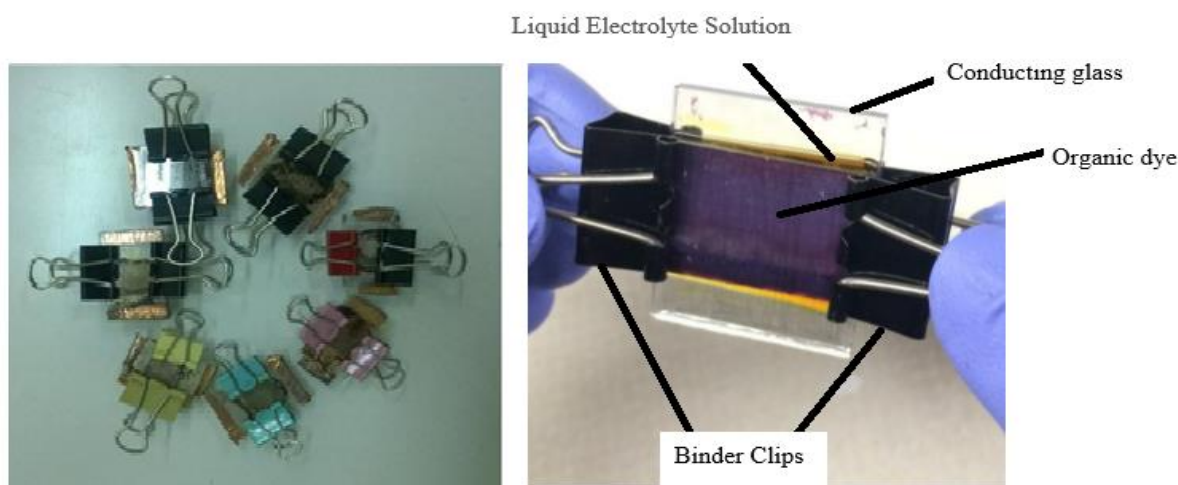


Figure 3: The fabricated/assembled cells used in this study.

In contrast, Figure 5 presents the SEM image for samples with the highest concentration considered in this study, i.e., 0.10 M. As seen from the microstructure, the surface of the electrode is covered with NaNO_3 or KNO_3 nanoparticles with an average size of approximately 1.0 nm, which is smaller than that for the samples modified with lower concentrations. Figure 5 further exhibits a significantly denser microstructure with nicely oriented grain boundaries.

3.3. Optical performance of the photoelectrodes

Figure 6 shows the UV-Vis transmission spectrum of absorption spectra of both non-modified (bare) and modified samples using both nitrates at the three concentrations. Figure 6 indicates that in the short

wavelength region (<300 nm), both the bare- TiO_2/ITO substrate and the alkaline nitrates- TiO_2/ITO substrates show essentially the same behavior. Beyond that, the figure shows a substantial decrease in light absorption. Moreover, Figure 6 shows that the optical absorption is slightly reduced with increasing solution concentration and further that NaNO_3 samples are less absorbent than their KNO_3 counterparts at the same concentration. This observation indicates the excellent optical absorption of alkaline nitrates- TiO_2/ITO film.

In a similar fashion, Figure 7 portrays the UV-Vis transmittance spectra of the tested samples and indicates that samples with higher concentration of an aqueous solution show lower transmittance in the long wavelength region ($\lambda > 400$ nm) while for $\lambda < 400$, samples show the same behavior, the penetrated light decreases seriously.

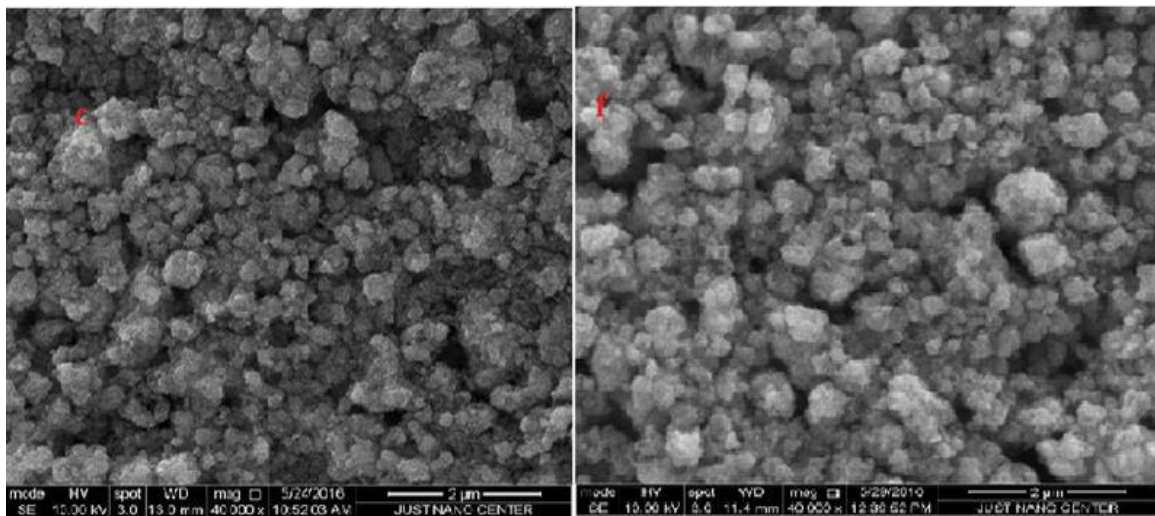


Figure 5: SEM images of NaNO_3 - TiO_2/ITO surface (left), and KNO_3 - TiO_2/ITO surface (right) at 0.10M concentration.

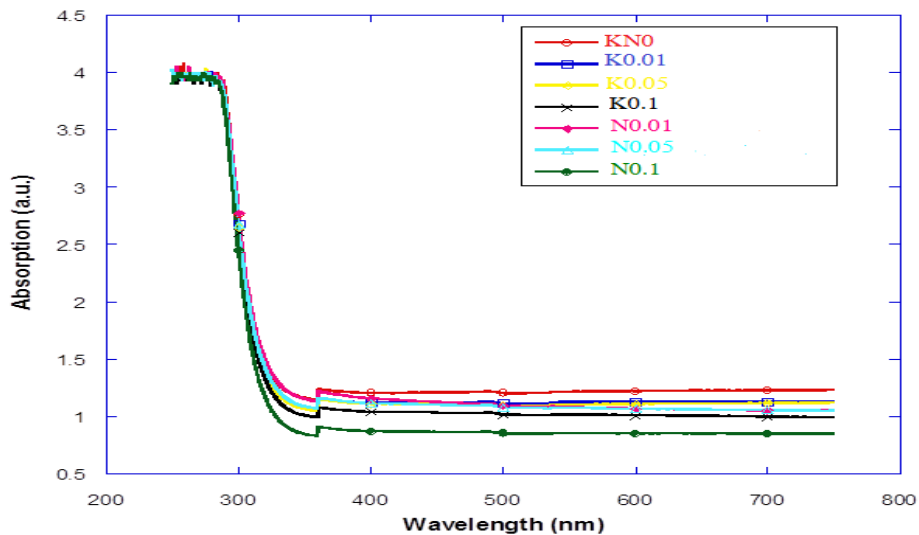


Figure 6. Absorption spectra of the photoelectrode samples.

3.4. XRD results

Figure 8 shows the XRD patterns of the photoelectrode samples. Crystallographic planes of TiO₂ anatase ((101), (004), (200), (105), (211), (204), (116), (220), (215)) could be observed at 2θ of 25.2°, 37.7°, 48.1°, 53.9°, 55°, 62.5°, 68.5°, 70.4°, and 74.7°, respectively. In contrast, NaNO₃ phase and KNO₃ phase start to appear at 2θ of 31.82° (006) peak and 27.33° (012) peak, respectively, indicating that the alkaline nitrates were successfully incorporated with TiO₂ paste.

3.5. The cell's J-V characteristics

Table 1 summarizes the cell's PV parameters at 40 °C and 13 °C including short-circuit current density (J_{sc}), open-circuit voltage (V_{oc}), fill factor (FF) and photoelectric conversion efficiency (η). In addition, Figures 9 and 10 display the J-V characteristics of the cell tested in this study for both the surface-modified and non-modified (bare- bare-TiO₂/ITO) photoelectrodes at 40 °C and 13 °C, respectively.

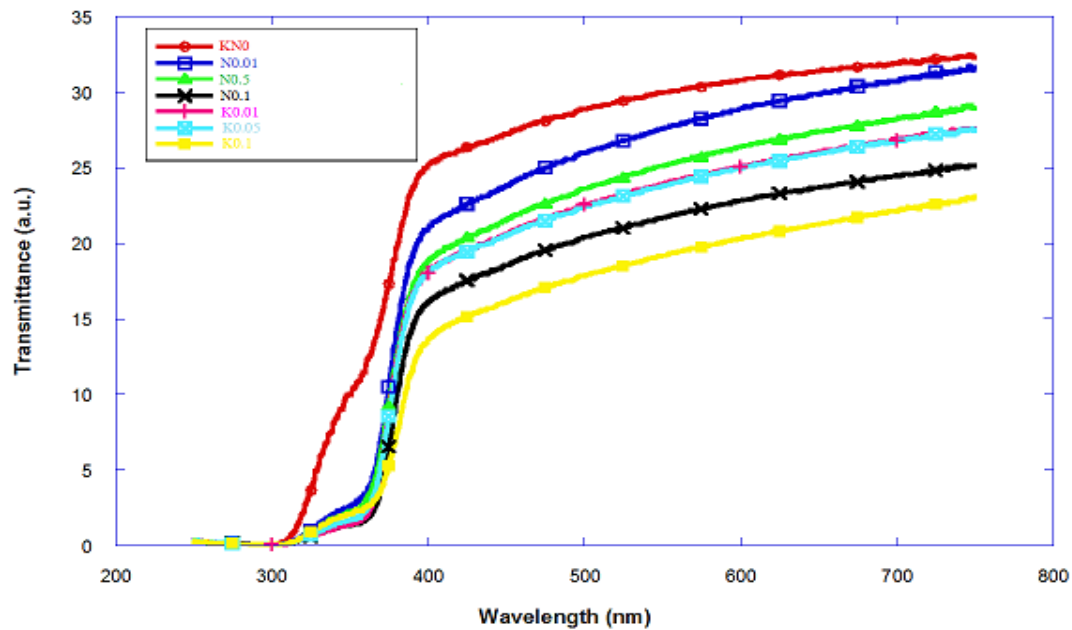


Figure 7. Transmittance spectra of the photoelectrode samples

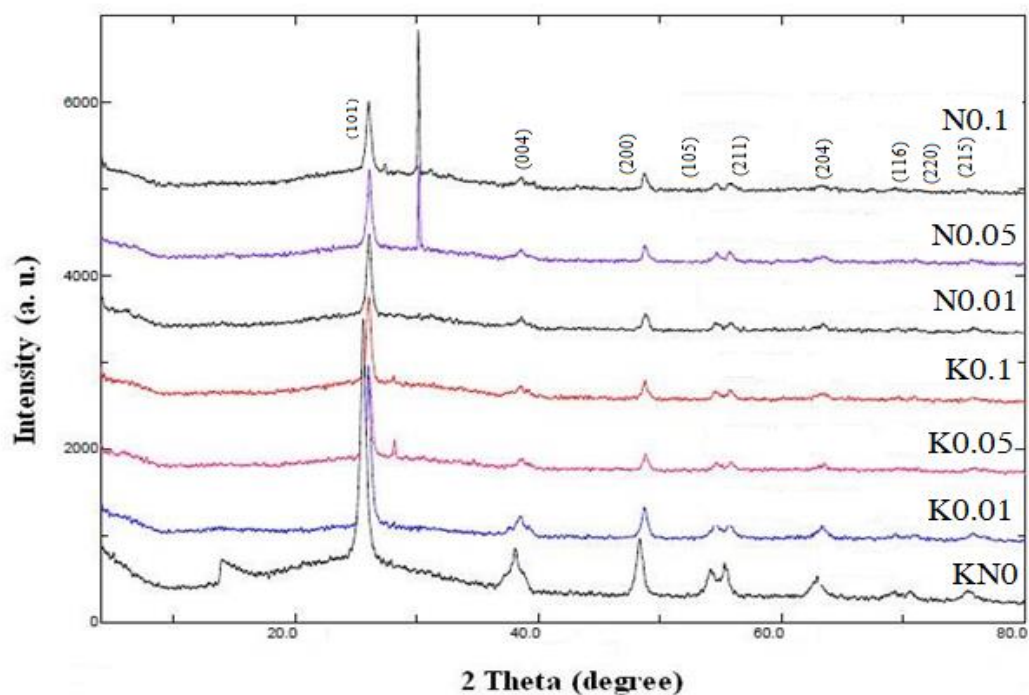


Figure 8. XRD patterns of TiO₂ - NaNO₃ and KNO₃ nanocomposites.

Table 1: Cell's photoelectric parameters for the surface-modified and non-modified (bare- TiO₂/ITO) photoelectrodes at 40 °C and 13 °C.

Surface photoelectrode		J _{sc} (mA/cm ²)	V _{oc} (V)	J _m (mA/cm ²)	V _m (V)	Fill Factor(%)	η (%)
bare-TiO ₂ /ITO at 40 °C (13 °C)		0.709 (0.793)	0.422 (0.429)	0.388 (0.438)	0.211 (0.211)	27.4 (0.271)	0.082 (0.092)
Modified KNO ₃ at 40 °C (13 °C)	TiO ₂ /ITO Concentration (M)						
	0.01	0.957 (0.996)	0.473 (0.560)	0.479 (0.505)	0.263 (0.316)	27.8 (0.286)	0.126 (0.159)
	0.05	1.297 (1.016)	0.515 (0.760)	0.725 (0.518)	0.263 (0.369)	28.6 (0.247)	0.191 (0.191)
	0.10	2.643 (2.942)	0.695 (0.784)	1.520 (1.674)	0.368 (0.421)	30.5 (0.306)	0.560 (0.705)
NaNO ₃ at 40 °C (13 °C)	0.01	1.154 (1.171)	0.505 (0.490)	0.635 (0.632)	0.263 (0.263)	28.7 (0.290)	0.167 (0.167)
	0.05	2.332 (2.420)	0.565 (0.718)	1.207 (1.256)	0.316 (0.421)	28.9 (0.304)	0.381 (0.529)
	0.10	3.507 (4.013)	0.777 (0.830)	1.994 (2.173)	0.421 (0.474)	30.8 (0.309)	0.840 (1.029)

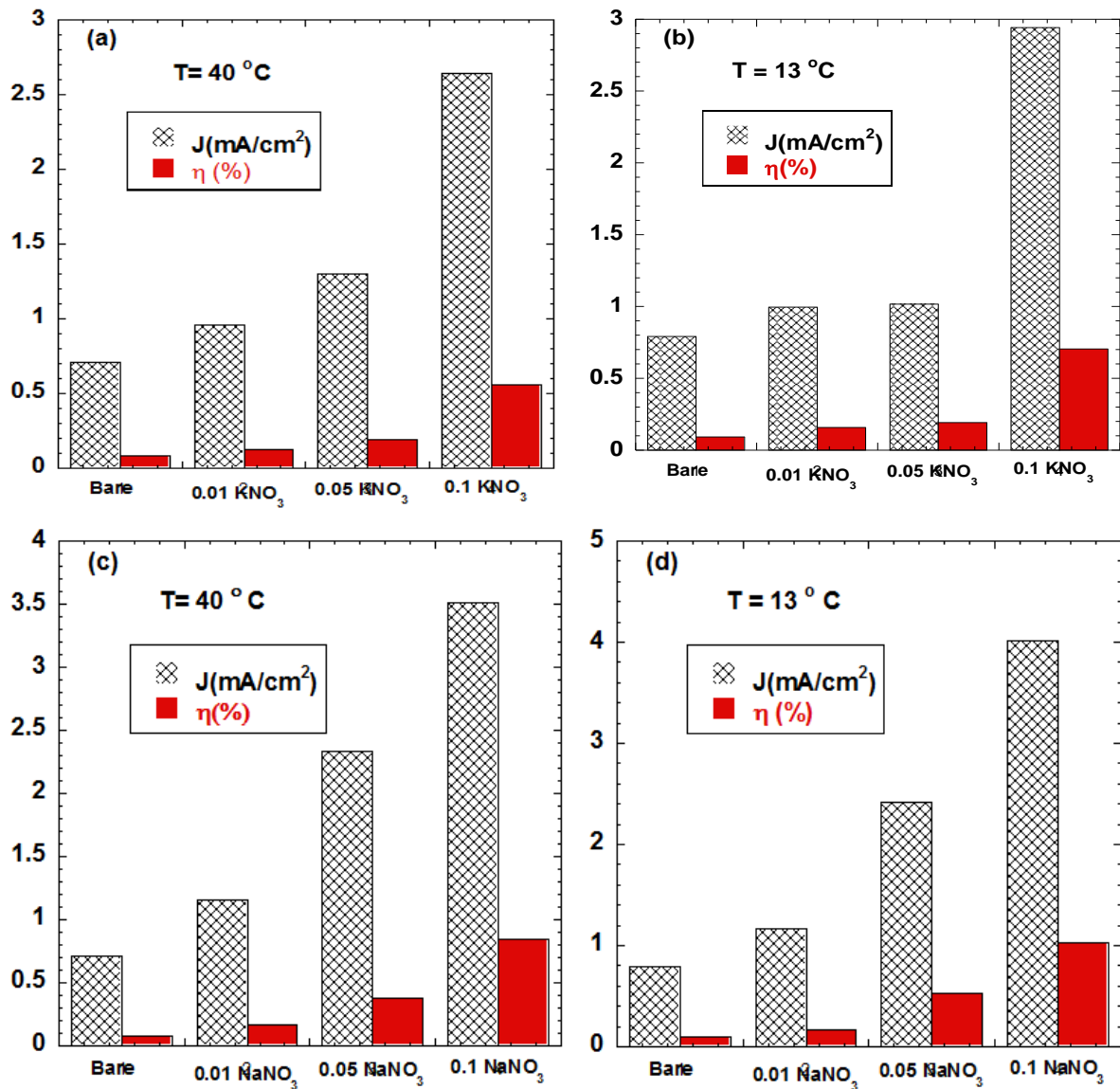


Figure 9. Histograms of distribution of current density J(mA/cm²) and photo-conversion efficiency η (%) (a) KNO₃ at 40 °C (b) KNO₃ at 13 °C (c) NaNO₃ at 40 °C and (d) NaNO₃ at 13 °C.

Figure 9 presents variations of current density, J , and efficiency, η , of DSSCs with various KNO_3 and NaNO_3 contents at different operating temperatures (40°C and 13°C). Results revealed that for all tested DSSCs samples, the current densities and the photo-conversion efficiency increases gradually with increasing the alkaline content. However, for DSSCs with 0.1KNO_3 at 13°C (Figure 9 – b), a drastic increase (about three times) in both current density and efficiency was observed. This may suggest that further increase in the alkaline content may give rise to the main DSSCs parameters and thus enhances the cell performance. Almost similar behavior was also observed at $T = 40^\circ\text{C}$ for the same DSSC.

Figure 10 (a, b) shows that the modified DSSC exhibited higher power conversion efficiency (PCE) than that with bare- TiO_2/ITO . For example, the same figure indicates that the PCE of the DSSC with NaNO_3 (0.01)– TiO_2/ITO and with KNO_3 (0.01)– TiO_2/ITO increased by, respectively, 200% and 150% relative to a cell with a bare- TiO_2/ITO .

Moreover, Figure 10 (a, b) demonstrates consistent increase in PCE with concentration of aqueous solutions. It may be readily noted from the same figure that the highest PCE was for the DSSC with NaNO_3 (0.1M)– TiO_2/ITO and reached 0.840. As evident from Figure 11 (a, b), similar trends were obtained for the tests at 13°C . This enhancement may be ascribed to the addition of NaNO_3 or KNO_3 , which greatly reduced charge recombination between the dye and TiO_2 film, as well as between the electrolyte and TiO_2 film. Further, Figure 11 (c) reveals that the PCE of the surface modified with NaNO_3 – TiO_2/ITO was higher than that for the surface modified with KNO_3 – TiO_2/ITO at any given concentration or operating temperature within the ranges considered here.

As far as the influence of operating temperature on cell performance, Figures 10 and 11, clearly and consistently demonstrate the positive influence of lower operating temperature on the cell performance.

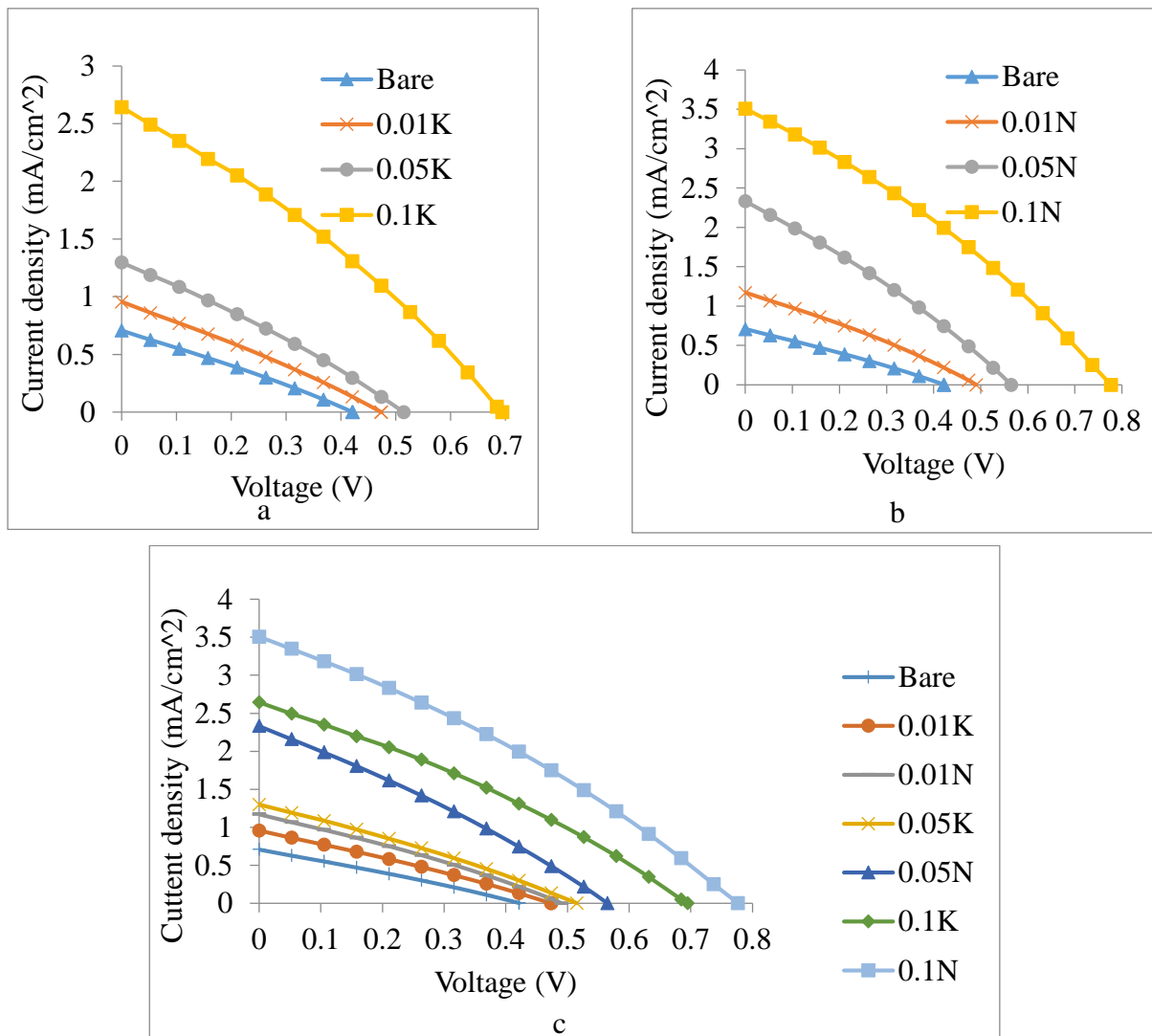


Figure 10: The cell's J-V curves at 40°C with different photoelectrodes (a) KNO_3 -modified (b) NaNO_3 -modified, and (c) Comparison between NaNO_3 - and KNO_3 -modified electrodes.

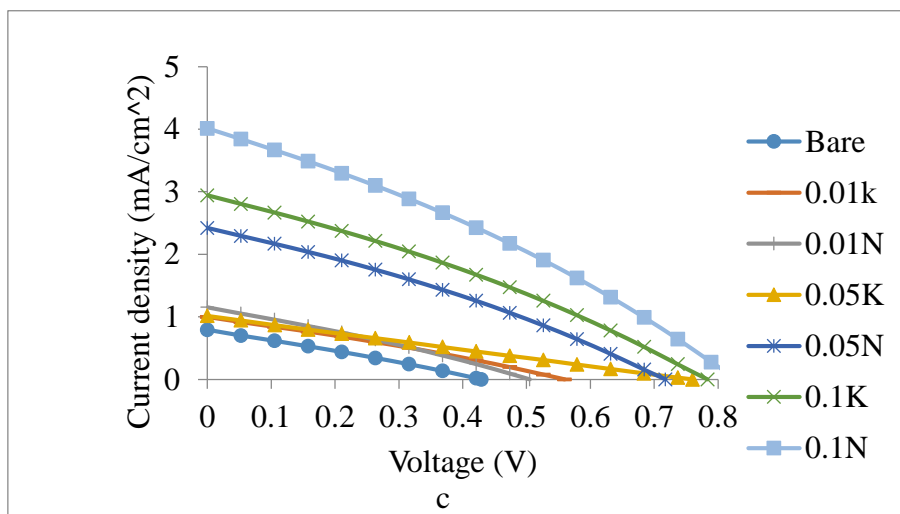
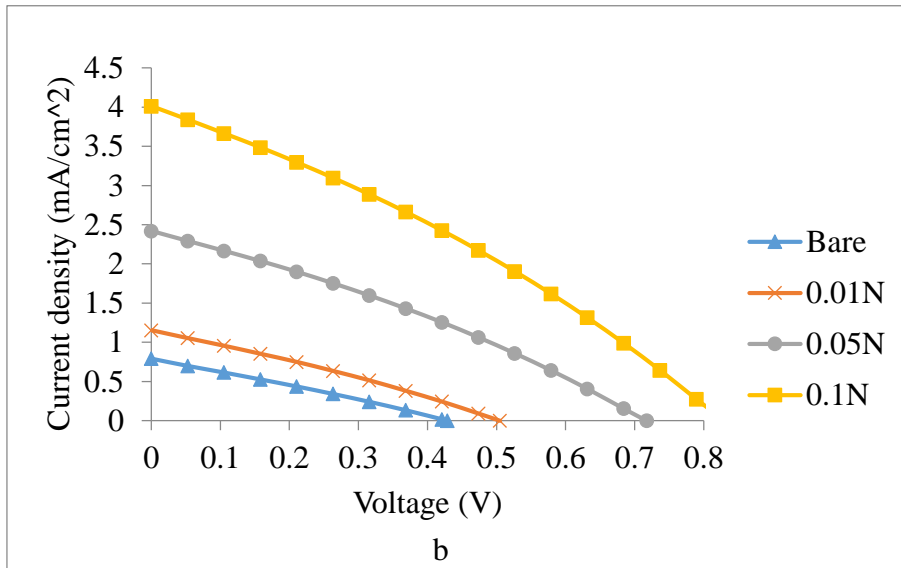
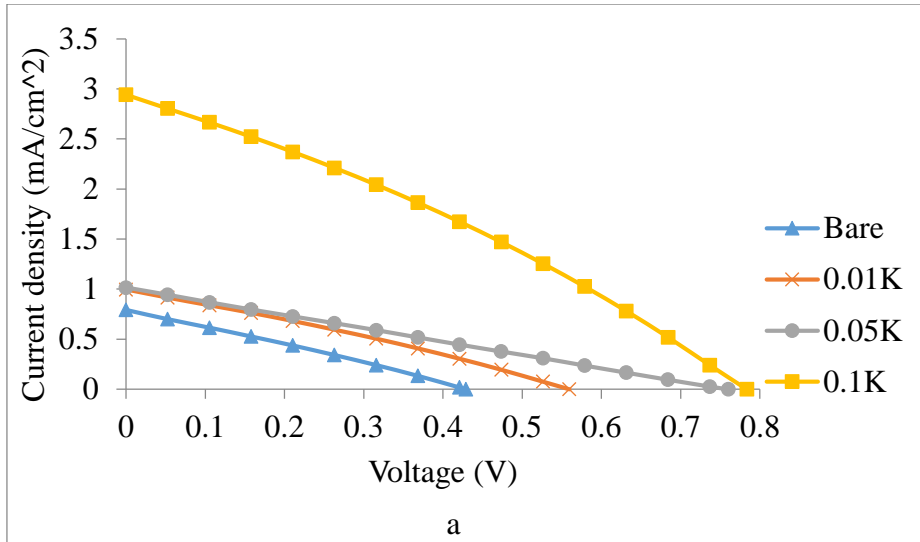


Figure 11: The cell's J-V curves at 13 °C with different photoelectrodes (a) KNO_3 -modified (b) NaNO_3 -modified, and (c) comparison between NaNO_3 - and KNO_3 -modified electrodes.

4. Conclusion

Based on the findings obtained in this work, it may be concluded that DSSCs, unlike existing solar cells, enjoy the attractive feature of easy, low-cost manufacturing under simple low-tech setups and limited resources. In addition, the results of this study indicate that coating the working electrodes of a typical DSSC with alkaline nitrates nanoparticle solutions have the potential to substantially improve the cell performance in terms of its power conversion efficiency and other characteristics. Moreover, DSSCs perform better at lower temperatures as is the case for their traditional PV counterparts.

5. Acknowledgements

Authors wish to express their gratitude to all individuals working at the Nanomaterials Lab., Department of Physics at Jordan University of Science and Technology (JUST) for all the technical assistance they provided. Thanks are extended to JUST Deanship of Research for funding this work.

References

- [1] Y. Demirel, "Energy: production, conversion, storage, conservation, and coupling". Springer Science & Business Media, 2012.
- [2] Askari, Mohammad Bagher, et al. "Synthesis and evaluation of MoWCoS/G and MoWCuS/G as new transition metal dichalcogenide nanocatalysts for electrochemical hydrogen evolution reaction." *Chemical Physics Letters* 691 (2018): 243-249.
- [3] Bahrapour, Hamid, et al. "Evaluation of renewable energies production potential in the Middle East: confronting the world's energy crisis." *Frontiers in Energy* (2017): 1-15.
- [4] WEC. World energy resources: 2013 Survey. England and Wales; 2013.
- [5] Sánchez CV. Thin film nanocrystalline silicon solar cells obtained by hot-wire CVD. Dissertation for the Doctoral Degree. University of Barcelona; 2001.
- [6] Edenhofer O, Madrugá R, Sokona Y, Seyboth K, Kadner S, Zwickel T, Eickemeier P, Hansen G, Schlömer S, Von Stechow C, Matschoss P. Renewable energy sources and climate change mitigation: special report of the Intergovernmental Panel on Climate Change. New York, Cambridge University Press; 2012.
- [7] A.M. Bagher, M.A. Vahid, M. Mohsen, "Types of Solar Cells and Application". *American Journal of Optics and Photonics*, 3, 94-113, 2015.
- [8] Stierstorfer J, Donald K, Teske S, Cameron M, Grafik B. Solar Generation-Solar Electricity for Over One Billion People and Two Million Jobs By 2020; 2006.
- [9] H. Gerischer, M. Michel-Beyerle, F. Reberstrost, H. Tributsch, "Sensitization of charge injection into semiconductors with large band gap". *Electrochimica Acta*, 13, 1509-1515, 1968.
- [10] IRENA. Renewable Energy Technologies: Costs Analysis Series [Online]. Available: www.irena.org/Publications, Volume 1: Power Sector, 2012.
- [11] Okoli LU. Fabrication and Characterization of Dye Sensitized Solar Cell Using Natural Dye from Roselle Plant. MSc. Thesis. Nnamdi Azikiwe University; 2010.
- [12] S.R. Raga, F. Fabregat-Santiago, "Temperature effects in dye-sensitized solar cells". *Physical chemistry chemical physics: PCCP*, 15, 2328-36, 2013.
- [13] Arsenault E. Three-Dimensional Transparent Conducting Oxide Based Dye Sensitized Solar Cells. 2011.
- [14] C.S. Chou, F.C. Chou, J.Y. Kang, "Preparation of ZnO-coated TiO₂ electrodes using dip coating and their applications in dye-sensitized solar cells". *Powder Technology*, 215, 38-45, 2012.
- [15] E.S. Kim, Y.S. Han, "Influences of Sodium Nitrate-Modified Photoelectrode on the Performance of Dye-Sensitized Solar Cells". *Journal of Nanoelectronics and Optoelectronics*, 10, 565-568, 2015.
- [16] Abdelkader MR, Al-Salaymeh A, Al-Hamamre Z, Sharaf F. A comparative analysis of the performance of monocrystalline and polycrystalline PV Cells in semi-arid climate conditions: the case of Jordan. *Jordan J Mech Ind Eng* 2010; 4:543-52.
- [17] Po-Jen Chu, Shu-Yuan Wu, Keh-Chang Chen, Ju-Liang He, Aleksey Yerokhin, Allan Matthews, Nano-structured TiO₂ films by plasma electrolytic oxidation combined with chemical and thermal post-treatments of titanium, for dye-sensitized solar cell applications, *Thin Solid Films*, Volume 519, Issue 5, 2010, Pages 1723-1728,
- [18] F. Sauvage, J.D. Decoppet, M. Zhang, S.M. Zakeeruddin, P. Comte, M. Nazeeruddin, P. Wang, M. Grätzel, "Effect of sensitizer adsorption temperature on the performance of dye-sensitized solar cells". *Journal of the American Chemical Society*, 133, 9304-10, 2011.
- [19] B. A. Albiss, M. I. Al-Widyan, I. Obaidat, "Influence of loadings of single-walled carbon nanotubes on the performance of ZnO nanorod-based dye-sensitized solar cells". *Ceramics International*, Vol. 42(2B): 3563-3568, 2015.
- [20] F. Sauvage, "A review on current status of stability and knowledge on liquid electrolyte-based dye-sensitized solar cells". *Advances in Chemistry*, 2014.
- [21] S. Suhaimi, M.M. Shahimin, Z. Alahmed, J. Chyský, A. Reshak, "Materials for enhanced dye-sensitized solar cell performance: Electrochemical application". *International Journal of Electrochemical Science*, 10, 28-59, 2015.
- [22] Tun MA. Design, construction and testing of an IV tester for thin-film solar cells and mini-modules. 2011.
- [23] T.Y. Cho, K.W. Ko, S.G. Yoon, S.S. Sekhon, M.G. Kang, Y.S. Hong, C.H. Han, "Efficiency enhancement of flexible dye-sensitized solar cell with sol-gel formed Nb₂O₅ blocking layer". *Current Applied Physics*, 13, 1391-1396, 2013.
- [24] P. Lellig. Application of a hybrid blocking layer in dye-sensitized solar cells [Online]. Available: <http://ubm.opus.hbz-nrw.de/volltexte/2012/3051/pdf/doc.pdf>, 2012.



الجامعة الهاشمية



المملكة الأردنية الهاشمية

المجلة الأردنية
للمهندسة الميكانيكية والصناعية

JJIMIE

مجلة علمية عالمية محكمة
تصدر بدعم من صندوق البحث العلمي

<http://jjmie.hu.edu.jo/>

ISSN 1995-6665

المجلة الأردنية للهندسة الميكانيكية والصناعية

المجلة الأردنية للهندسة الميكانيكية والصناعية: مجلة علمية عالمية محكمة تصدر عن الجامعة الهاشمية بالتعاون مع صندوق دعم البحث العلمي والابتكار - وزارة التعليم العالي والبحث العلمي في الأردن.

هيئة التحرير

رئيس التحرير

الأستاذ الدكتور محمد سامي الأشهب

مساعد رئيس التحرير

الدكتور احمد المقدادي

الدكتور مهند جريسات

الأعضاء

الأستاذ الدكتور طارق العزب

جامعة البلقاء التطبيقية

الأستاذ الدكتور محمد الوديان

جامعة العلوم والتكنولوجيا الاردنية

الأستاذ الدكتور جمال جابر

جامعة البلقاء التطبيقية

الأستاذ الدكتور محمد تيسير هياجنه

جامعة العلوم والتكنولوجيا الاردنية

الأستاذ الدكتور محمد الطاهات

الجامعة الاردنية

الأستاذ الدكتور علي جوارنه

الجامعة الهاشمية

فريق الدعم

المحرر اللغوي

الدكتور بكر محمد بني خير

تنفيذ وإخراج

م . علي أبو سليمة

ترسل البحوث إلى العنوان التالي

رئيس تحرير المجلة الأردنية للهندسة الميكانيكية والصناعية

الجامعة الهاشمية

كلية الهندسة

قسم الهندسة الميكانيكية

الزرقاء - الأردن

هاتف : 00962 5 3903333 فرعي 4147

Email: jjmie@hu.edu.jo

Website: www.jjmie.hu.edu.jo